MANGANESE OXIDE – GRAPHENE OXIDE HYBRID CATALYST SUPPORTS FOR USE IN DIRECT METHANOL FUEL CELLS

by

AIMEE FAE JACKSON

A thesis submitted to the University of Birmingham for the degree of

DOCTOR OF PHILOSOPHY

Centre for Hydrogen and Fuel Cell Research

School of Chemical Engineering

University of Birmingham

September 2019

Abstract

Direct methanol fuel cells are a promising, clean energy technology with many applications including in the portable power sector. Catalyst materials which are an important part of these devices have short lifetimes due to degradation from reaction intermediates. This is particularly the case for the catalyst at the anode side of the direct methanol fuel cell – which is typically made from platinum metal, or a platinum based alloy.

In this study, the use of hybrid catalyst supports was investigated with an aim to improving the durability of the anode catalyst. A simple microwave synthesis method was utilised to produce manganese oxide – graphene oxide and later manganese oxide – carbon black catalyst supports. It was found that manganese oxide - graphene oxide hybrid supports have good durability but suffer from re-stacking of the graphene sheets – inhibiting their performance. Manganese oxide – carbon black supported platinum nanoparticle catalysts had improved performance and durability over the commercial platinum and platinum alloy catalysts. In addition, a preliminary study into the effect of the hybrid support on other novel catalysts suggested that it is the interaction of the platinum and the manganese oxide in direct contact which provides the improved durability.

Contents

List of Abbreviations

ADF	Annular Dark Field
BF	Bright Field
CB	Carbon Black
CV	Cyclic Voltammetry
CO_{ads}	Adsorbed Carbon Monoxide
DMFC	Direct Methanol Fuel Cell
ECSA	Electrochemical Surface Area
EDX	Energy Dispersive X-ray Spectroscopy
FWHM	Full Width Half Maximum
GL	Gaussian - Lorentzian
GO	Graphene Oxide
HAADF	High Angle Annular Dark Field
Helium KED	Helium Kinetic Energy Discrimination
HRTEM	High Resolution Transmission Electron Microscope
HUPD	Hydrogen Under Potential Deposition
I_b	Backwards Current
$I_{b\ Peak}$	Backwards Peak Current
ICP-MS	Inductively Coupled Plasma Mass Spectrometry
I_f	Forwards Current
$I_{f\ Peak}$	Forwards Peak Current
IL-TEM	Identical Location Transmission Electron Microscope
JCPDS	Joint Committee on Powder Diffraction Standards
LF	Lorentzian Finite
MnO_x	Manganese Oxide

MOR	Methanol Oxidation Reaction
OH_{ads}	Adsorbed hydroxyl group
ORR	Oxygen Reduction Reaction
PEMFC	Polymer Electrolyte Fuel Cell
Pt/CB	Platinum nanoparticles supported on carbon black
Pt/C_{com}	Commercial Platinum nanoparticles supported on carbon
Pt/GO	Platinum nanoparticles supported on graphene oxide
Pt/MnOx-CB	Platinum nanoparticles supported on Manganese Oxide - Carbon Black hybrid support
Pt/MnOx-GO	Platinum nanoparticles supported on Manganese Oxide - Graphene Oxide hybrid support
$PtRu/C_{com}$	Commercial Platinum-Ruthenium alloy nanoparticles supported on carbon
rGO	Reduced Graphene Oxide
RuSePt/CB	Ruthenium-Selenium-Platinum alloy nanoparticles supported on carbon black
RuSePt/MnOx-CB	Ruthenium-Selenium-Platinum alloy nanoparticles supported on manganese oxide - carbon black support
SHE	Standard Hydrogen Electrode
STEM	Scanning Transmission Electron Microscope
TEM	Transmission Electron Microscope
TGA	Thermo Gravimetric Analysis
XPS	Xray Photoelectron Spectroscopy
XRD	X-ray Diffraction

List of figures

List of tables

ACKNOWLEDGEMENTS

I have been incredibly lucky to have the help and support of many people during the course of my PhD. There are too many to name individually, but a few are listed below.

Firstly - to all my family. Particularly my parents Arlene and Peter, and to Sam. Thank you for being there always. For supporting me through everything. I'm not sure you realise just how much your help and support has meant. I really couldn't have done it without you all. To both my nans and grandads Win and Ron, and Arlene and Syd – thank you for your support and I know how proud you all are, were, and would be of how far I have come. And to everyone else – especially Brenda, Malcolm, and Pam thank you for your encouragement and support.

To my friends – Jade, Abi, Rhi, James, Bea, Laura, the leaders in Girlguiding Berkswich District - especially Jane & Hilary, and everyone else. Thank you for your support, encouragement and kindness through both the good and difficult times.

To my colleagues at the University of Birmingham. Thank you for your help, support, advice and friendship during this absolute rollercoaster of a journey that we have all been on together.

To the Public Engagement Team at the University of Birmingham and people I've met through them – especially Jon, Caroline, Leah, Coralie and James. Thank you for your encouragement and support and reminding me of the joy of science.

Finally, to my supervisor Neil – thank you for all the support, knowledge and guidance along the way.

CHAPTER 1 Introduction

With an increase in the global average temperature now unavoidable, major efforts are underway to mitigate the effects and to minimise the degree of warming that our planet inevitably faces[1]. A key factor in these efforts is decarbonising the entire energy system of nations who have largely relied on the same fossil fuel energy sources that powered the industrial revolution in the 18th Century. In order to achieve a <2°C temperature rise, it is vital that countries move away from a system based on fossil fuels (coal, oil, gas) to a system which is 100% renewable. This includes the entire energy sector: the electricity and gas network, transport, and portable power systems.

To achieve such a massive change in the system, a blend of approaches is necessary. Renewable energy generation accounts for an increasing proportion of the UK's energy generation[2], however the mismatch between energy generation by renewables and typical energy usage[3] means that large scale energy storage must be implemented to replace the dependence on coal and gas. The options available which allow energy to be stored for a long period of time are limited to pumped hydro storage, compressed air, and hydrogen storage[4]. Battery storage is limited to shorter time periods due to self-discharge. In the case of hydrogen storage, when the renewable energy generator (solar panels, wind turbine, tidal power etc.) is producing a surplus of energy, the excess energy can be diverted to produce hydrogen (e.g. via electrolyser to split water into hydrogen and oxygen). The hydrogen produced can be stored (e.g. as a compressed gas in cylinders) and kept until a time and place that it is needed. The hydrogen can then be recombined with oxygen to form water, either through combustion, or through an electrochemical process in a fuel cell, at the same time

generating electricity with a maximum efficiency between 50% and 80% (if electricity and heat generated can be used e.g. in a combined heat and power system).

In addition to providing a clean energy storage solution, hydrogen and fuel cell power is one option for decarbonising the transport and portable power sectors, as it has the highest gravimetric energy density of any known substance[4]. Hydrogen and fuel cells have already started to prove themselves as an important part of the future transport sector. Fuel cell power has already been implemented in a range of transport applications including: trains - such as the first fuel cell train - the Coradia iLint from Alstom[5]; buses - in cities globally[6–8]; and cars - with Hyundai, Toyota and Honda leading the way and other manufacturers to follow[6]. In terms of portable power, fuel cells (in this instance typically powered by methanol rather than hydrogen due to its superior volume energy density) have been used for a range of applications, including: for leisure (in motorhomes, caravans, on boats etc); for military purposes[9]; and for specialist off-grid applications (including remote documentary filming[10], and powering remote research expeditions[11]).

With fuel cells already proving their worth in a range of areas with total shipments increasing year on year[6], it is important to note the various types of fuel cell that are available:

Table 1.1 Types of fuel cell on the market

Type	**Full Name**	**Fuel Used**[12,13]	**Electrolyte**[12,14]	**Catalyst Material**[12]	**Operating Temperature**[14]	**Moving Ion**[12,13]	**Areas Of Use**[6]	**2018 Shipments (Units)**[6]
PEMFC	Polymer Electrolyte Fuel Cell	Hydrogen	Nafion Membrane	Platinum	<120°C	H^+	Portable, Transport, Stationary	42600
DMFC	Direct Methanol Fuel Cell	Methanol	Nafion Membrane	Platinum/ Platinum - Ruthenium	60 - 80°C	H^+	Portable, Transport	3700
SOFC	Solid Oxide Fuel Cell	Hydrogen, Biogas, Natural gas	Yttria Stabilised Zirconia	Nickel	500 - 1000°C	OH^-	Portable, Stationary	27800
MCFC	Molten Carbonate Fuel Cell	Natural gas, Biogas	Liquid Sodium / Potassium Carbonate	Nickel / Nickel Alloy	600 - 700°C	CO_3^{-2}	Stationary	<50
AFC	Alkaline Fuel Cell	Hydrogen	Liquid Potassium Hydroxide	Iron, Cobalt, Nickel	<100°C	OH^-	Stationary	<50
PAFC	Phosphoric Acid Fuel Cell	Hydrogen	Liquid Phosphoric Acid	Platinum	150 - 200°C	H^+	Stationary	200

All fuel cells work based largely on the same principles. Fuel is oxidised at the anode, and oxygen is reduced at the cathode. During this process, ions move across the membrane (or electrolyte), and electrons are made to flow through the external circuit where they provide power. The oxidised fuel, reduced oxygen, and electrons are combined to form water at the cathode.

In a polymer electrolyte fuel cell (PEMFC), the H_2 fuel is oxidised at the anode to form H^+ hydrogen ions and electrons following the equation (1.1):

$$H_2 \rightarrow 2H^+ + 2e^- \qquad (1.1)$$

The hydrogen ion passes through the Nafion membrane, while the electrons flow through the external circuit, providing the power to the electrical load. Then, at the cathode, oxygen is reduced to form water with the equation (1.2):

$$\frac{1}{2}O_2 + 2H^+ + 2e^- \rightarrow H_2O \qquad (1.2)$$

This gives rise to the overall equation for a PEMFC reaction (1.3):

$$\frac{1}{2}O_2 + H_2 \rightarrow H_2O \qquad (1.3)$$

Clearly, the only by product of generating energy through this process is water (provided pure hydrogen is used as the fuel source), making this an attractive option for the future low carbon energy system.

This thesis focuses in particular on the DMFC, or Direct Methanol Fuel Cell. This fuel cell is based on the PEMFC, but it uses methanol as its fuel source instead of pure hydrogen. DMFCs are much more suited to small, portable applications than PEMFCs due to fuel storage and

transport issues, and even have some commercial success in this area. There are some drawbacks to using DMFCs which are mostly linked to the use of methanol fuel. Such issues include methanol crossover where methanol can cross the electrolyte barrier. This not only causes material issues across the fuel cell, but also decreases the overall energy output of the fuel cell. The methanol environment at the anode also causes fast degradation of the catalyst, which limits the lifetime of the DMFC. While this short device lifetime may be acceptable for certain applications, for DMFCs to become more widely adopted, the short lifetime issues have to be addressed. A key part to tackling these issues is materials development to produce more stable material components which will enable the DMFC to work for longer. This thesis focuses on the anode catalyst layer in DMFCs.

1.1 Objectives

The aim of this work is to investigate the potential of a hybrid material: manganese oxide on high surface area carbon (graphene), as a novel anode catalyst support material for use in a direct methanol fuel cell (DMFC). In particular, the aim is to evaluate the extent to which the addition of manganese oxide to a carbon support can improve the durability and stability of the anode catalyst in a DMFC. To determine this, the following will be investigated:

1. Develop a reliable method for fabricating manganese oxide - graphene oxide hybrid catalyst supports.
2. The use of manganese oxide in a hybrid carbon - based support and its influence on the catalyst when tested for DMFC applications.
3. The effect of varied amounts of manganese oxide in the catalyst support on the performance of the catalyst.
4. The influence of manganese oxide on different carbon supports and the overall performance for DMFC applications.

CHAPTER 2 Literature review

2.1 Hydrogen vs Methanol

When it comes to the use of hydrogen and fuel cells in the future energy system, there are a number of challenges to overcome and drawbacks that need further improvement to increase uptake of the technology and to make it as good as it can be. One such drawback for hydrogen is that while its gravimetric energy density is the highest of all substances, its volumetric density is very low when it is in the gas phase[4]. Storing hydrogen as a liquid is not practical for portable applications due to the low temperatures required and the issue of boil-off where the liquid hydrogen will evaporate over time due to a boiling point of -253°C[15]. Research to minimise boil-off and enable more widespread use of liquid hydrogen is underway[16], but liquid hydrogen storage tends to be reserved for high cost applications such as space rocket fuel tanks and for transporting hydrogen between pressurised gas containers[17]. The most common form of hydrogen storage is in the compressed gas phase. For many cases, the hydrogen gas is compressed at 350 bar or 700 bar – giving a volume saving of >99.6% compared to standard atmospheric pressure[18]. Storage of hydrogen at 700 bar is the standard for automotive applications – with such a high storage pressure requiring strong 4-layer composite tanks to ensure the passengers of the vehicle are kept safe. The problems arising from the storage and transportation of hydrogen gas can be overcome if a hydrogen-rich liquid fuel is used instead.

One such example of a hydrogen-rich, liquid fuel is methanol. The problems of storage and distribution are removed, as the fuel can be stored in a standard liquid fuel container. Methanol as fuel is currently more readily available, can be transported easily, and has a

higher volumetric energy density when compared to hydrogen[19]. In addition to this, methanol can also be produced renewably[20], from biomass, wastes and CO_2.

Methanol has been used as a fuel not only in a fuel cell, but also in a traditional combustion engine - as demonstrated in drag car racing in USA[21] making it a viable energy source for a variety of purposes.

2.2 Direct methanol fuel cells (DMFCs)

Methanol can be utilised directly in a fuel cell, with no pre-reforming[19], when it is used in a direct methanol fuel cell (DMFC). A direct methanol fuel cell (DMFC), which can be seen in Figure 2.1, is a low temperature fuel cell[22] that is largely the same as a polymer electrolyte fuel cell (PEMFC), consisting of a Nafion membrane in the centre. Platinum catalysts lie on either face of the membrane, to facilitate the fuel (methanol or hydrogen) oxidation at the anode and oxygen reduction reaction at the cathode. These platinum catalysts are typically supported by porous carbon nanomaterials (such as carbon black). The supported catalysts are deposited on porous carbon-based gas diffusion layers (carbon felt, carbon paper etc). Bipolar plates made from graphite or metal are used to direct fuel and oxidant in, and reaction products out of the fuel cell through their serpentine surface pattern.

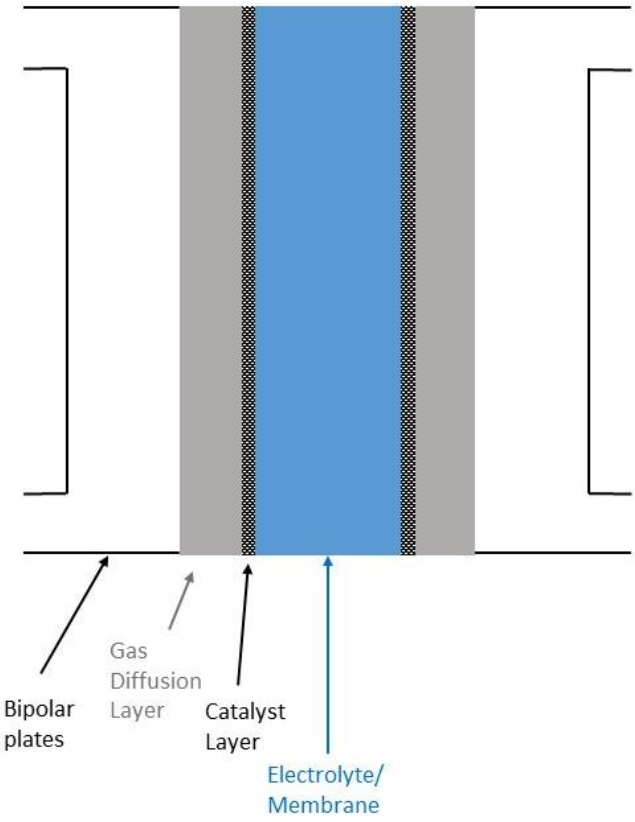

Figure 2.1 Polymer electrolyte and direct methanol fuel cell layout

DMFCs offer significant advantages over PEM fuel cells, as they do not experience fuel storage issues associated with hydrogen, as they utilise liquid methanol fuel, as opposed to gaseous hydrogen fuel in the case of a polymer electrolyte fuel cell (PEMFC). Along with the fuel benefits outlined above, DMFCs have already had commercial success across a range of transport and portable applications[5,7–11]. However, DMFCs are not without their problems, as they suffer from a low efficiency when compared to other fuel cell types[23]. This low efficiency is due to methanol crossover and catalyst poisoning.

Methanol crossover is the mechanism whereby methanol makes its way across the hydrated Nafion membrane to the cathode. This causes the oxygen reduction reaction to have competition as the methanol which has crossed over undergoes methanol oxidation,

competing with the oxygen reduction and reducing the overall efficiency of the fuel cell[24]. To overcome this, a thicker Nafion membrane tends to be used in commercial DMFCs to try to prevent methanol crossover. Research is underway to use composite membranes, or alternative and more selective membranes which do not permit methanol crossover[25]. An alternative way to prevent methanol crossover would be to use a cathode catalyst which is selective towards the oxygen reduction reaction and so methanol crossover would not affect the cathode in this case[26–28].

Catalyst poisoning occurs when the surface active sites of the catalyst get blocked[29]. Chemicals and reaction intermediates (in the case of a DMFC anode, carbon monoxide) bind to the active catalyst sites, which renders them inactive towards the desired reaction. This causes a reduction in the overall efficiency of the catalyst as there are fewer active sites on which the desired reaction can occur. In extreme cases, if enough of the catalyst surface becomes blocked, the reaction can no longer proceed and the fuel cell will stop working[22].

These mechanisms (catalyst poisoning and methanol crossover) affect the overall lifetime of DMFCs, as the materials in the fuel cell are negatively affected by the methanol and its by-products. In order to improve these problems, new or modified materials with better performances need to be investigated and developed for use in DMFCs.

In a PEMFC, hydrogen is supplied to the anode to form hydrogen ions and electrons.

$$H_2 \rightarrow 2H^+ + 2e^- \qquad (2.1)$$

The H^+ moves across the membrane to the cathode, while the e^- is diverted through an external circuit to provide power. At the cathode O_2 is reduced and combines with H^+ and e^- to form water (H_2O).

$$O_2 + 4H^+ + 4e^- \rightarrow 2H_2O \quad (2.2)$$

This gives the overall PEMFC equation:

$$H_2 + O_2 \rightarrow 2H_2O \quad (2.3)$$

From the above equations (2.1 – 2.3) it is evident that this process produces clean electricity as no carbon dioxide or other pollutants are formed. The only by-product is water when pure hydrogen is used as the fuel.

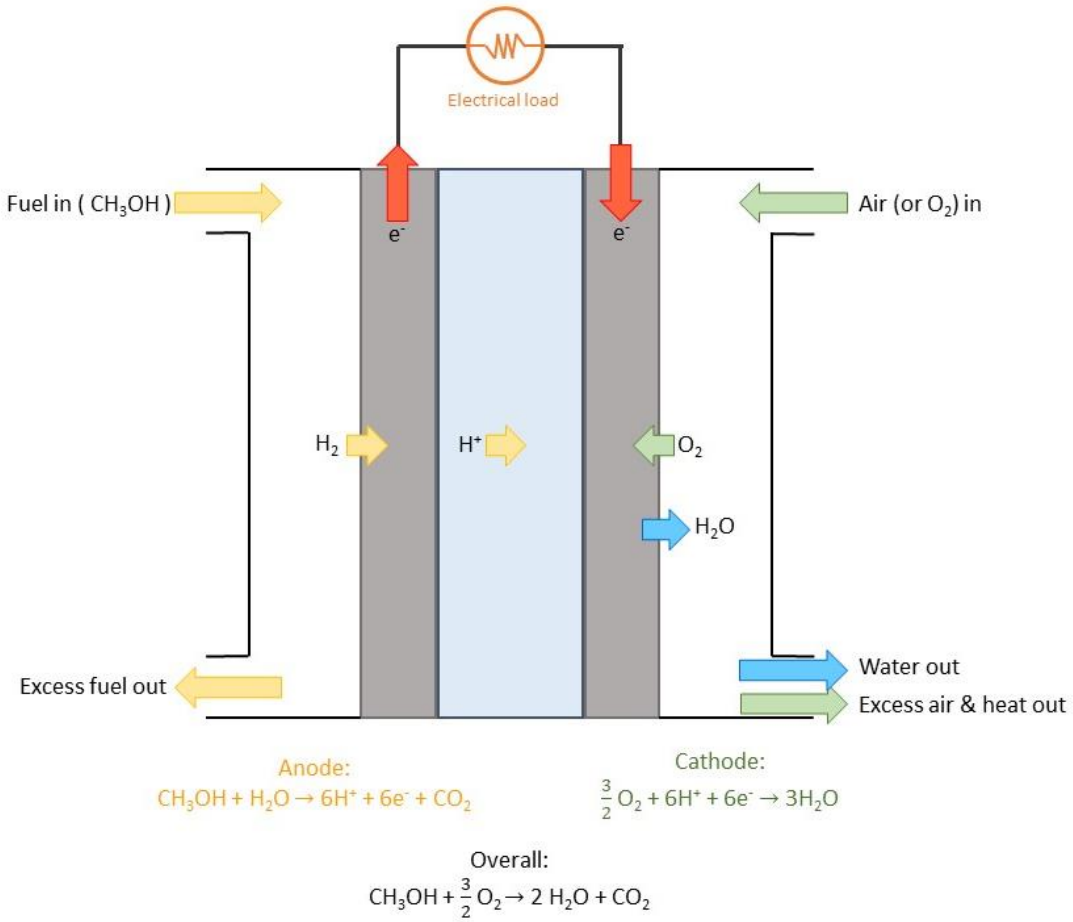

Figure 2.2 Schematic diagram of a direct methanol fuel cell.

In a DMFC, shown in Figure 2.2 the methanol fuel is oxidised in the presence of water to form the hydrogen ions (H^+) which travel through the membrane, and the electrons (e^-) which

travel through the external circuit to give power to the electrical load. This means that the reaction at the anode becomes more complex than for pure hydrogen, with the methanol oxidation reaction (MOR) involving 6 electrons:

$$CH_3OH + H_2O \rightarrow 6H^+ + 6e^- + CO_2 \quad (2.4)$$

And at the cathode oxygen is reduced in the oxygen reduction reaction (ORR) to give water:

$$O_2 + 4H^+ + 4e^- \rightarrow 2H_2O \quad (2.5)$$

This means that for a DMFC, the overall reaction is:

$$2CH_3OH + 3O_2 \rightarrow 4H_2O + 2CO_2 \quad (2.6)$$

The oxidation of the methanol, involving 6 electrons, occurs via a complex pathway with many intermediate steps. It is because of these intermediate steps that the platinum anode catalyst from a DMFC is prone to poisoning from –CO intermediates. This limits the lifetime of these fuel cells.

A range of direct electrochemical mass spectrometry investigations have proven that the methanol oxidation reaction has two parallel pathways, which can be seen in Figure 2.3, with one or the other being preferred under certain conditions[30–33]. On platinum metal surfaces, the competing pathways for the methanol oxidation reaction are shown in Figure 2.3 The methanol oxidation pathway on platinum crystal surfaces (proposed by Hausmans et al 2006) The first of the two is an indirect pathway, whereby methanol is oxidised through C/O/H species adsorbed onto the platinum catalyst surface to –CO and finally CO_2. The –CO adsorbed on the platinum surface that occurs during this pathway acts as a poison, as it binds strongly and blocks the platinum active sites, hindering the reaction. The second pathway is the direct

pathway, where the methanol is oxidised via formate to CO_2. On closer inspection to an electrochemical cyclic voltammogram of the methanol oxidation reaction, the two pathways can be seen with each pathway beginning at slightly different potentials[34].

The pathway selected is highly sensitive to the structure of the surface on which the reaction takes place[35]. The direct pathway is favoured on smooth surfaces[34], and on the Pt(111) surface in H_2SO_4[35]. When steps are present on Pt(111) surfaces in H_2SO_4, the proportion of methanol oxidised through the indirect pathway is increased[35], showing that surface structure has an effect on the oxidation mechanism. The optimal Pt surface for selectivity towards the methanol oxidation reaction is a combination of steps and terrace sites, such as those found on the Pt(554) and Pt(553) surfaces[36].

In the indirect pathway described, the -CO intermediates are strongly bound to the platinum catalyst surface. The bond strength of the adsorbed intermediates may be reduced by the employing a different catalyst support, or by using an alloy catalyst so that the reaction intermediates do not poison the catalyst as readily[37]. This is achieved by shifting the preference towards linearly-bound -CO (which is bound onto a single Pt atom) vs bridge-bound -CO (which is bound to two adjacent Pt atoms)[37,38]. In addition, a catalyst support that is rich in -OH groups (either inherent or from dissociation of water) such as manganese oxide, can assist in the removal of adsorbed intermediate species by donating the -OH groups[38,39]. This facilitates the removal of the adsorbed -CO groups on the platinum nanoparticle surface through oxidation of the -CO to CO_2.

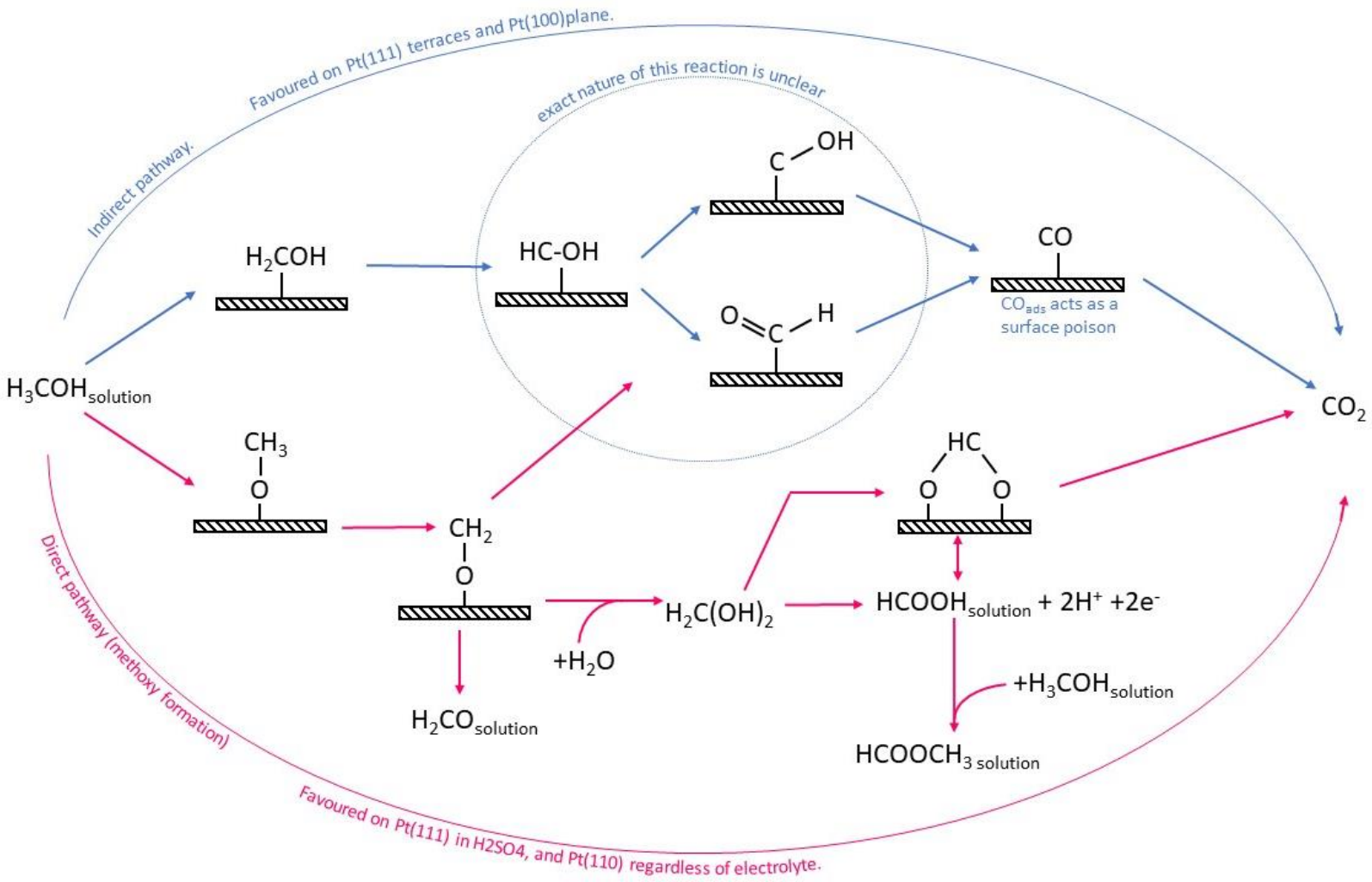

Figure 2.3 The methanol oxidation pathway on platinum crystal surfaces (proposed by Hausmans et al 2006)[35,36]

2.3 The catalyst layer and its degradation in DMFCs

In the catalyst layer of the methanol fuel cell, there are two major components: the catalyst particles and the catalyst support. In a commercial DMFC, the anode catalyst particles are typically either platinum or a platinum-ruthenium alloy and the catalyst support tends to be carbon black[40].

Catalyst degradation can occur through a series of different mechanisms: dissolution, Ostwald ripening, agglomeration, detachment, and support corrosion[41–44].

Pt dissolution is where individual platinum atoms dissolve out of the nanoparticles, leading to a reduction in the nanoparticle size. Pt dissolution is a particular problem at the cathode of a PEM fuel cell, as it is subject to trace amounts of chloride and potentials greater than 0.85 V (vs SHE) and pH values <2 (at 25°C) which is the region where Pt dissolution occurs according to the Pourbaix diagram[45]. Pt dissolution is sensitive to pH, temperature, and potential, and surface area of the Pt particle. As a result of Pt dissolution, Pt atoms can be found exiting the fuel cell in the waste water stream, or migrating into the membrane, where they degrade the membrane and block hydrogen transport.

Ostwald ripening occurs when Pt atoms are dissolved from smaller nanoparticles, but rather than exiting the fuel cell or migrating into the membrane, the dissolved Pt atoms are re-deposited onto other, larger nanoparticles. This mechanism is a secondary mechanism, which relies on Pt dissolution. Ostwald ripening leads to a decrease in overall surface energy of the catalyst. The dissolved Pt atoms can migrate along the surface of the support (2D Ostwald ripening) or through the membrane/electrolyte (3D Ostwald ripening)

Agglomeration occurs when whole nanoparticles migrate across the support to join up with other nanoparticles. These combine together to form one larger particle with the result being a decrease in surface energy.

Detachment happens when whole nanoparticles become disconnected from the support. Both detachment and agglomeration occur when the interaction between the particle and the support is low or decreases, for example due to support corrosion.

Support corrosion (or carbon corrosion) occurs when the carbon is oxidised at fuel cell operating conditions to CO_2[46]. The standard potential for this is 0.2V vs Standard Hydrogen Electrode (SHE), which is well within the operating range for a fuel cell. Although this form of degradation is thermodynamically facile, the kinetics of carbon support corrosion are slow, which leads to the widespread use of carbon supports for fuel cell catalysts. Carbon corrosion is most prevalent during fuel cell start up and shut down, due to the low potentials experienced during the start up/shut down cycles. For typical carbon black, primary carbon particles are joined up in a microporous network, with each primary carbon particle made up of a more amorphous type core, with more ordered graphene – like sheets towards the outer of the carbon black particle. IL-TEM studies have shown that the inner of the carbon black particles corrodes first, followed by the more crystalline shell. Support corrosion has drastic consequences for the fuel cell. Carbon corrosion can accelerate catalyst degradation through agglomeration and detachment, and finally after more severe carbon corrosion, the mass transport in the fuel cell (fuel supply, reaction products leaving) is affected due to a reduction in porosity of the catalyst layer.

Since the mechanisms of degradation in the catalyst layer are sensitive to the environment and conditions (pH, temperature, potential etc), the different mechanisms are more or less likely to occur during certain periods of operation through the fuel cell cycle. For example, carbon corrosion is more likely during start up and shut down, and dissolution is more likely to occur at the cathode. A combined approach, taking into account both the catalyst and support, and their interaction is needed in order to achieve a stable catalyst and support and is necessary to minimise the effects of degradation[47].

2.4 Catalyst materials in DMFCs

To improve the performance of catalyst particles, there are numerous investigations with a range of approaches including modifying the commercial catalyst or even developing and using an alternative catalyst material[48,49]. Approaches include different Pt-based alloys and non-precious metal catalysts[40,48,50,51], and carbon based materials such as N-doped carbons[52,53] and carbon nanotubes[52,54].

The standard approach to improve durability that is used in commercial DMFC anode catalysts is to use a PtRu alloy catalyst. The Ru component of the catalyst particle promotes the dissociation of water to form –OH which then adsorbs onto the catalyst surface. This –OH can then oxidise the -CO_{ads} (seen in the indirect pathway described in Figure 2.3) to CO_2, removing the –CO which would otherwise block the active sites on the catalyst[55]. The promotion of –OH_{ads} formation is therefore a key to improving the DMFC anode durability.

Although the use of Ruthenium and other platinum group metals and rare earth metals in Pt based alloys, such as Pt-Ru[50,56] and Pt-Pd[40,57] have shown improvements in terms of catalytic activity and resistance to poisoning, the alloyed metals are still expensive, and so do not offer

a significant price advantage when looking at overall fuel cell cost and lifetime. On the other hand, if Pt can be alloyed with cheaper transition metals, this would lead to an obvious price advantage. Metals such as Ni, Co and Fe[58] have been tested, and these also show improved catalytic activity and higher tolerance to CO poisoning as opposed to pure Pt particles.

The improved durability and increased performance, coupled with the significant price advantage exhibited by PtNi, PtCo, and PtFe over the rare earth and platinum group metals makes these alloyed particles very interesting[59]. However, alloyed nanoparticles are prone to further degradation mechanisms on top of those already outlined.

Alloy particles can suffer from de-alloying and surface segregation, where the different reactivity of the metals in the alloy lead to one metal being preferentially dissolved or leached out[60]. This leaching and dissolution may be due to incomplete alloying, excess of alloyed metal, or thermodynamic instability[61]. This results in a compromised structure of the nanoparticle and ultimately only a Pt nanoparticle remains[62], which can undergo further degradation at a more accelerated rate as it is no longer alloyed.

Ternary and quaternary alloys such as CoPtRu[63], PtRuRh[56], PtRuMo[64], PtCoW[40], PtRuMoW[40], and more[64] have been developed to further improve the stability of alloy catalyst particles. Such alloyed catalyst particles exhibit increased performance and improved durability over PtRu commercial catalysts, though a more complex synthesis route and issues of alloy degradation may prevent such complex alloys from reaching commercialisation.

The aim for an alloyed catalyst is to produce an alloy which promotes –CO oxidation, and so reduces the poisoning and degradation of the catalyst. The promotion of –CO oxidation may proceed by a number of different mechanisms on an alloy particle. First, the bi-functional

effect (seen in PtRu alloys) where –OH is formed, which can then oxidise the –CO to CO_2 can still occur on non-Ru Pt-alloys[29]. Secondly, a ligand effect can reduce the binding energy of the –CO on the Pt surface, allowing CO_2 formation to occur more readily[65]. Finally, a hydrogen spillover effect may also occur[40] which also promotes removal of -CO intermediates from the catalyst surface.

The mechanisms outlined above to promote –CO oxidation may also be achieved to some extent by modifying or altering the catalyst support[40].

2.5 Catalyst supports

An important part of the catalyst layer in low temperature fuel cells is the catalyst support. The catalyst support has numerous purposes in the fuel cell. It anchors the catalyst particles to ensure that they remain spatially in the location where they are needed - in the catalyst layer - and ensures there are well dispersed nanoparticles across the support surface to maintain a high catalyst surface area. The catalyst support also provides a conductive pathway to facilitate the flow of electrical current through to the external circuit. A microporous structure is also exhibited by the catalyst support to enable fuel and reactant gases to enter and leave the catalyst active sites. In addition, the catalyst support can interact with the catalyst to enhance the activity or durability of the catalyst particle[13,66–69].

A material that is used widely as a catalyst support in low temperature fuel cells is carbon black[70]. However, carbon black supports can suffer from corrosion[71,72], meaning the catalyst nanoparticle detaches from the support. Carbon corrosion also means that the structure of pores in the support (which allow transport of gasses) are altered. Another problem relating to carbon black supports is the possibility of movement and migration of the catalyst

nanoparticles, leading to the agglomeration of the nanoparticles. Catalyst nanoparticles can agglomerate through a range of mechanisms. These include dissolution, Ostwald ripening – both 2D and 3D, and nanocrystal migration on the support[47,73]. These problems of catalyst agglomeration and support corrosion lead to reduced electrochemical surface area (ECSA), and activity, so an improved support is desirable, as a stronger nanoparticle-support interaction may help to increase stability[74]. Examples of supports that have been investigated include: non-carbon supports such as polymers (including PANI and PPY); metal oxides (including Ti-oxides, W-oxides, and ITO); and other carbon based supports such as carbon nanotubes and more recently graphene[75].

The optimum support for the anode and the optimum support for the cathode of the fuel cell may well be made from different materials. For example the 4-electron oxygen reduction reaction (ORR) pathway is favoured on graphene based materials[76,77]. Manganese based supports and catalysts can be used to favour a 4-electron ORR pathway and provides selectivity against MOR when in alkaline conditions[78]. The promotion of the 4-electron pathway makes these materials preferable for cathode catalyst supports.

For the anode in a DMFC, there are many possibilities of catalyst support. Carbon based supports (such as graphene oxide[79], carbon nanotubes[80] etc) may provide some enhancement of the catalyst durability, but they suffer from carbon corrosion to some degree[81]. Metal oxides[82] and metal carbides[83] are promising, but they suffer from lower electrical conductivity compared to carbon based supports. Hybrid supports which utilise the best from both families of support (carbon based and metal oxide based) show promise in the future development of catalyst support materials, giving both durability and electrical conductivity[29,40,81,84,85]. In this thesis, a hybrid carbon - metal oxide support will be investigated.

From the range of carbon materials that are available, graphene-based material looks like promising catalyst support materials. Its 2D nature and high surface area should lead to good dispersion of the catalyst particles on the support[86]. In addition, defects arising from the graphene's production should provide good anchor sites for the catalyst particles to bind strongly to[87].

Manganese oxide has been selected as the metal oxide to be investigated as it is readily available and has a large range of oxidation states[88]. It is possible to form a variety of structures from various manganese oxides, giving a range of possible catalyst support candidates. In addition, other first row transition metal oxides such as iron, cobalt or nickel have shown promise in DMFC catalyst layers[29,58,89,90].

2.6 Background to Graphene and Manganese Oxide and their role in catalyst supports

2.6.1 Graphene

Since the experimental discovery of graphene in 2004 - by exfoliating graphite mechanically with scotch tape[91] - it has been investigated extensively by the scientific community. As a completely two dimensional material, its unique and remarkable properties[86,92–94] lend this semi-metal to a wide variety of applications in a range of research areas, including; sensors[95], antireflective coatings[96], transparent and flexible conducting films[97,98], supercapacitors[99,100], batteries[101,102], and fuel cells[66,103]. There are various properties of graphene that make it particularly interesting for fuel cells. Its proton selectivity makes it of particular interest for use in membranes[103] to minimise gas crossover and improve efficiency. The electronic conductivity properties of graphene sheets make it interesting for use in the catalyst layers[66],

as a high performance support for the catalyst. Using graphene as a catalyst support has shown previously to give higher ECSA, higher catalytic activity and enhanced durability[104] when compared to traditional carbon black supports.

A popular production technique to produce large amounts of graphene is to use the Hummers' method[105] (or a modified Hummers' method). In the Hummers' method, sheets of graphite powder are intercalated by ions, and the expanded sheets are then oxidised and further separated to produce graphene oxide. This produces graphene oxide sheets in large quantities and at low cost compared with other graphene production techniques. These sheets can then be reduced to give reduced graphene oxide (rGO). The resulting graphene is not pristine, and has some defects and residual oxygen groups[106]. This means that whilst the electrical conductivity and carrier mobility of reduced GO is higher than graphite, it is not as high as pristine graphene due to the defects present on the rGO[107]. These defects and oxygen groups that reduce the electronic properties however may be desirable in a fuel cell catalyst support, as they have been shown to help to anchor the catalyst nanoparticles[48]. The oxygen groups and lattice defects present on rGO are believed to serve as nucleation sites for catalyst nanoparticles to grow directly on the support[108]. Such a direct growth mechanism enhances the contact and interaction between the catalyst and support, leading to a more stable catalyst[68]. These oxygen groups and defects on the reduced graphene oxide support also help to reduce the effect of poisoning on the catalyst[85].

Transition metal oxides on graphene[49,59,109] have shown promise for low cost, durable fuel cell catalysts and can also be used with platinum to achieve high activity[40,89,110]. Metals investigated include Fe, Co, Ni and Mn[111,112]. These metals when used in their oxide form on

graphene show promise to fulfil the aim of low cost, highly durable and high activity catalysts for low temperature fuel cells.

2.6.2 Manganese Oxide

Manganese is a transition metal and has been used for centuries, with one of its first uses being as a colorant in glass[113]. Currently, 80 to 90% of world manganese produced is used in the steel industry – where between 0.6 and 10 weight % is used to improve mechanical properties of the steel[114]. Other uses of manganese and its oxides include in batteries[115,116], capacitors[116,117], livestock feed and plant fertiliser[114], and catalysis[88]. Their high activity and low cost make manganese oxides promising for use in fuel cells to help to lower the overall cost of the device.

There have been many methods used previously to produce manganese oxide, and more widely, transition metal oxide nanoparticles[68,109,112,115]. When producing a transition metal oxide, it is important to select the appropriate synthesis method and conditions if a specific single form of oxide is desired, because the manufacturing route selected and the conditions used will affect the resulting metal oxide produced. Manganese oxide has a large range of possible oxidation states, so it is clearly critical to control the synthesis route to achieve the desired manganese oxide. Because of the abundance of oxidation states possible in manganese oxide in particular, there are many synthesis routes, including solvothermal[118], hydrothermal[78,119], calcination[120], and more recently an increase in green synthesis methods. These use less energy and fewer harsh chemicals in the synthesis process. Such green methods typically include the use of ultrasonics[121–123] or a microwave method[117,124,125].

A method that has been widely cited for the synthesis of monodisperse nanocrystals of transition metal oxides uses thermolysis of metal-oleate complexes to produce transition metal oxide nanoparticles[109]. This method was first used successfully with Fe, Co and Mn. However there have since been many types of transition metal oxides produced via this method, or a modification of this method[115,126].

At the Swiss Nanoscience Institute (SNI) under the project Mangacat, there has been work to produce MnO_2 nanoparticles on an industrial scale using a flame spray pyrolysis technique[127,128]. This method can be used to produce vast quantities of nanoparticles, although great care must be taken to ensure the correct conditions are used to produce the desired product. Colloidal synthesis of manganese oxides is also possible[129], for example using PVA to obtain supported colloids, after which the PVA can be removed with heat to leave the activated catalyst. The atmosphere under which the PVA is removed determines the type and activity of the catalyst nanoparticles produced. A photo-assisted synthesis of manganese oxide has been achieved, using manganese nitrate as a precursor, and NaOH or LiOH as the hydroxide[130]. Depending on the time and concentrations used, different morphologies of MnO_2, MnOOH and Mn_3O_4 can be produced. Another option is to use a hydrothermal method to synthesise manganese oxide[131]. This type of method is promising as it uses mild conditions, is simple, holds good possibilities for scale up, and can even be used at room temperature.

The main drawback with the above synthesis routes for a hybrid support system is that they then require the synthesised manganese oxide nanoparticles to be subsequently attached to the supporting carbon, and in some cases require the removal of capping agents that are covering the nanoparticle surface prior to (or alongside) attachment. Options to deposit the synthesised manganese oxide nanoparticles onto the support include using ultrasonics[132] or

electrodeposition methods[133], which adds extra processing steps into the synthesis. More steps in the manufacturing procedure gives more chance for problems to occur, with some reported issues being; insufficient interaction between nanoparticles and graphene, uneven dispersion of nanoparticles on graphene, and re-stacking of graphene sheets. These issues mean that a one pot synthesis whereby manganese oxide is grown directly on the graphene is highly desirable, as it can improve the properties of the hybrid material, and also makes the synthesis route as simple as possible, minimising the chance for issues to occur.

One pot MnO_x on graphene (or rGO) synthesis routes are desirable, as they lead to a reduced contact resistance between the manganese oxide (nanoparticle) and the graphene (support). The enhanced contact and interaction between the nanoparticle and support leads to enhanced performance of the hybrid material as a catalyst support. This enhanced performance can include: improved conductivity as contact resistance is reduced; reduced particle detachment and carbon corrosion due to the strong binding between particle and support; improved lifetime of the overall system[48,68,69].

2.6.3 Low temperature one-pot routes to producing MnO_x-rGO materials

One option to produce a hybrid support in a one-pot route is to use a low temperature reaction. These low temperature methods will not reduce the graphene oxide at the same time as depositing the manganese oxide on the graphene oxide, so the graphene must first be reduced before the manganese oxide growth step. One such example involves a redox reaction being performed using reduced graphene oxide with sodium hydroxide and potassium sulfate, resulting in flower-like MnO_2 directly grown on already reduced graphene oxide[134]. The direct growth on rGO in this instance was shown to reduce the contact

resistance, leading to faster electron transport rate. A synergistic effect between the rGO and MnO_2 also leads to enhanced catalytic activity for ORR. This result however is in alkaline media, and when tested in acid, there was low catalytic activity due to the instability of MnO_2 in acid. The second example of a low temperature synthesis uses a dipping and stirring method[135]. Carbon nanotube films were dipped into a precursor solution and stirred vigorously – leading to MnO_2 deposition. For this method, it was found that stirring must be very fast in order to grow any MnO_2 on the carbon nanotube film.

Moving on from these low temperature methods, and in order to minimise experimental steps and complexity, it is particularly favourable to reduce the graphene oxide simultaneously with MnO_x growth. Such methods require application of heat, or high energy (such as provided in a microwave or ultrasonics method) to enable reduction of GO to rGO in addition to growth of MnO_x.

2.6.4 Hydrothermal one-pot routes to produce MnO_x-rGO materials

One such higher temperature method demonstrated for a one-pot MnO_x-rGO synthesis is a hydrothermal route. This hydrothermal route has been used extensively, and often uses a potassium permanganate precursor in solution with GO. This solution is typically heated in an autoclave for around 12 hours at 180 – 200°C, to produce a MnO_x-rGO composite material. A range of resulting materials have been reported[136,137].

Another hydrothermal route, which produced Mn_3O_4-rGO[138] used a two-step method. Initially, $Mn(Ac)_2$ precursor and GO sheets were dispersed in DMF and water at 80°C to obtain a dense uniform coating on GO. Then, this was hydrothermally treated for 10 hours at 180°C to grow crystalline Mn_3O_4 nanoparticles. The nanoparticles produced by this method were

uniformly distributed with around 10 wt% GO in the product. There was a good interaction between the Mn_3O_4 nanoparticles and GO sheets, providing a good charge transport and also good dispersion of nanoparticles to avoid agglomeration. This method used a lower concentration of $KMnO_4$ during the Hummers method production of GO, in order to obtain a lower oxygen content on the GO.

It has been demonstrated that MnO_2-rGO[78] can also be produced via a hydrothermal method. In this case, the precursor solution of $KMnO_4$ was mixed with $MnSO_3$ and chemically reduced GO, and then heated at 180°C for between 0 to 72 hours. This resulted in a range of nanostructures of MnO_2 on the rGO. Up to 10 minutes resulted in MnO_x nanoparticles, 30 minutes to 15 hours resulted in MnO_2 nanowires, and between 24 and 72 hours resulted in MnO_2 micro prisms. Testing in alkaline media for ORR showed that these composites exhibited a 4-electron reduction process. The nanowires showed best stability compared to the other morphologies grown (nanoparticles or micro prisms), but again this was in alkaline media.

A mixture of Mn_2O_3 and MnO_2 on graphene[122] was produced by using $Mn(NO_3)_2$ and GO (from Hummer's method) in water. This was then heated at 180°C for 12 hours, and then finally after washing was either dried in an oven or freeze dried. Manganese oxide nanoparticles of 10 - 20 nm were distributed uniformly on the surface of the graphene, and the composite had high conductivity.

Mn_3O_4-N-doped-rGO[121] was produced by first producing an N-doped graphene hydrogel from Hummer's method GO. This N-doped graphene was then ground into a fine powder and

stirred with $KMnO_4$ before being heated to at 180°C for 12 hours. From this method, tube like manganese oxide dispersed on slightly wrinkled N-doped graphene sheets was produced.

It is worth noting that each hydrothermal synthesis has slight variations in the precursor solution, dispersion, and heating parameters. This suggests that the forms of manganese oxide produced are sensitive to synthesis conditions.

2.6.5 Green synthesis routes to producing MnO_x-rGO materials

As an alternative to a hydrothermal method, and as a potential 'green' synthesis route, ultrasonics can be used to produce a composite MnO_x-rGO material. An ultrasonic probe is used in place of, or just before, the autoclave step and similar precursor solutions can be used to the hydrothermal methods. The ultrasonic probes work by acoustic cavitation, where the chemical reaction takes place at high temperatures and pressures[132] generated by collapsing bubbles.

MnO_2 needles on graphene[139] have been grown by mixing GO (from Hummer's method) and $MnCl_2.4H_2O$ in isopropyl alcohol, using ultrasonication for 30 minutes, followed by heating to 83°C and the addition of $KMnO_4$, and then refluxing. The resulting manganese oxide nanoneedles were comprised of a few nanorods aggregated together and covered both surfaces of the rGO sheets.

A purely ultrasonic synthesis method has also been reported to prepare Mn_3O_4 on graphene[123]. This method used potassium permanganate and GO (produced from a Hummer's method) in water, which were then subject to an ultrasonic probe for 30 minutes. The authors suggested that an increase in precursor concentration in this method lead to an

increase in Mn_3O_4 crystallinity. The manganese oxide forms flat patches across the rGO, whose coverage increases with precursor concentration.

Another 'green chemistry' route to an effective and rapid synthesis of MnO_x-rGO composite material is through the use of a microwave[124,125]. Graphene oxide and a manganese oxide precursor are simply mixed, and then microwaved. The solvent used must have a dipole to enable it to absorb microwave energy, for example water. A hydrothermal method can be adapted for use in the microwave – meaning that the synthesis time goes from 12 hours to 10 minutes - which is a clear advantage[140].

Using a microwave synthesis method, MnO_2 has been grown on CNTs[117]. This method used CNTs and $KMnO_4$ in water, which were stirred for 1 hour to enable the potassium permanganate to adsorb onto the CNT wall. The mixture was then placed in a microwave at 700W for 10 minutes and cooled. This method resulted in a thin layer of MnO_2 on the CNT wall. This method is by far the quickest synthesis method of all those discussed, as the microwave step takes just 10 minutes, compared with up to 1 hour of sonication, or 12 hours of heat treatment.

Other methods for producing a MnO_x-rGO composite material include; calcination[120], electrodeposition[141], and even novel green methods using recycled powder materials[142] have been investigated. Clearly there are many methods in which to produce manganese oxide-graphene composite materials, which can often be adapted slightly to produce slightly different materials.

2.6.6 Microwave synthesis

Microwave synthesis methods are attractive as they can produce rapid localised heating of the materials and create interesting structures and products. Microwave synthesis techniques use microwaves which are electromagnetic waves with wavelengths in the cm range (0.1 – 100cm)[143]. There are a range of different microwave devices which are used for microwave synthesis methods. Some can use a standard microwave device like a household microwave, which use standing wave formations inside the cavity of the machine and a rotating plate to generate the heat. There are also more sophisticated scientific microwave heating devices which include reflectors to generate a uniform microwave field inside the cavity to obtain better, more reproducible results[144]. These may also have temperature, pressure, and irradiated power measuring capabilities. However, the underlying principles of the microwave synthesis are the same for all microwave devices that can be used.

In a typical microwave synthesis, a polar solvent is needed so that the electric component of the electromagnetic wave can interact with the dipole moment of the solvent molecule – dielectric loss heating. The dipole of the molecule rotates to align with the applied electric field, causing the molecules to oscillate with the applied field. The solvent molecules cannot oscillate as fast as the rapidly changing field, which causes the solvent to heat up. This dielectric heating of the solvent and can achieve temperatures above the boiling point of the solvent. It is a much quicker and more uniform way to heat up a solvent than conventional heating on a hot plate, and provides much more flexibility to produce interesting and novel materials[145]. In addition to dielectric loss heating, there are other mechanisms by which the microwave can interact with the chemicals used in the synthesis.

The microwave may interact with any electrically conductive material present in the beaker, causing localised heating of the conducting surface – called conduction loss. The microwave interacts in the same way as any other electromagnetic wave when it reaches with the surface of a conductor, whereby the wave is attenuated as described by Maxwell's equations[146]. The incoming wave causes free electrons in the conductor to move, meaning the wave is absorbed and so causing local heating of the conductor. Conduction loss is particularly strong in carbon black and similar materials, so this form of localised heating will be present in the synthesis methods described in this thesis, which will use carbon based supports[143].

In addition to the electric field component of the microwave, the magnetic field component may interact with any materials which have magnetic properties – in magnetic loss heating. In magnetic materials and metal powders, the effect of magnetic loss is even greater than the dielectric loss[145]. The magnetic component of the microwave is absorbed strongly by magnetic powder, leading to rapid heating of the material. Magnetic heating should be present in the synthesis presented in this thesis, because transition metals and their oxides in particular exhibit magnetic loss heating when exposed to microwaves[143].

The combination of manganese oxide and graphene oxide in the catalyst support means that all three microwave heating modes will be present in the system described in this thesis. Dielectric loss heating, magnetic loss heating and conduction loss heating will be present in the carbon and metal oxide locations of the material, as well as in the polar solvent itself.

From a survey of the methods outlined in this section, a simple one-pot microwave synthesis method has been selected. This method has been chosen, as it is a facile method, allowing for variations of the MnO_x-GO produced by tweaking the synthesis parameters such as

microwave time, precursor concentration, graphene : manganese ratio etc. In addition, the process of growing the manganese oxide nanostructures directly on the graphene has the potential to generate a better material, as this type of method typically produces a material which has a reduced contact resistance between the graphene and manganese oxide[134] and enhanced stability. Two solvents were selected for synthesis: water and ethylene glycol. These are both low toxicity solvents with high dielectric loss tangents, meaning they will heat quickly via dielectric loss heating in the microwave.

CHAPTER 3 Materials synthesis

For all materials produced in this work, 3 main methods were used. In the case of graphene oxide, a Hummers method was selected due to the tuneable nature of the graphene oxide product when made in this manner. For MnO_x-GO synthesis, a microwave synthesis method was used, which varied slightly throughout the work in order to achieve varying loadings of manganese oxide and investigate the effects this had on the overall performance. Finally, to deposit platinum on the array of supports produced, a second microwave method was used. This platinum deposition method was kept constant across every support, so that only the effect of the support varied throughout the range of materials produced.

3.1 Support synthesis

The first step towards producing the manganese oxide - graphene oxide hybrid support materials used in this work was to produce the graphene oxide, onto which the manganese oxide could be grown. Then, this hybrid support was further decorated with platinum nanoparticles to produce a catalyst for testing.

3.1.1 Graphene Oxide synthesis

An effective catalyst support is required to have high electrical conductivity[66,147]. In order to achieve this from a graphene oxide (GO) support, the GO should be produced with a low oxygen content, so that when it is reduced, the majority of the oxygen functional groups can be removed, leaving a highly conductive rGO. A modified Hummers' method[85,105] was chosen for producing GO because of its simplicity and tunability; and the results showed a lower oxygen content than other authors[148].

First, 3 g of graphite powder (Sigma, 99.9%) and 2.28 g sodium nitrate (Sigma, >99.0%) were added to the reaction vessel, in an ice bath to maintain a low temperature. Next, 100 mL of sulfuric acid (Sigma, 95-98%) was added under continuous stirring. Meanwhile, 13.5 g potassium permanganate (Sigma, >99.0%) was added to 200 mL water and thoroughly mixed. The potassium permanganate solution was added dropwise to the reaction vessel, with continual stirring over ice for several hours. Once all of the potassium permanganate had been added to the mixture, it was left to stir for 5 days, with the ice bath removed after 1 day of stirring. After the stirring period of 5 days had passed, the mixture was left to stand for 48 hours for solids to precipitate. The excess permanganate solution was then decanted, and the slurry washed by filtration in 5% H_2SO_4 (made up from Sigma, 95-98%) / 30% H_2O_2 (Sigma, 30%) solution for the first wash, followed by 9 washes in 3% H_2SO_4 (made up from Sigma, 95-98%) / 0.5% H_2O_2 (made up from Sigma, 30%). The resulting slurry was washed by centrifugation in water a further 10 times. The final product of graphene oxide was oven-dried at 60°C.

3.1.2 Manganese Oxide – Graphene Oxide and Manganese oxide – Carbon Black synthesis

To produce the manganese oxide - graphene oxide (MnO_x-GO) composite material, 150 to 400 mg of manganese salt (either $KMnO_4$ (Sigma, >99.0%) or $Mn(NO_3)_2$ (Sigma, ≥97%)) was thoroughly mixed in a beaker with 50 mL ultrapure water. Meanwhile, 100 mg of graphene oxide (produced via the modified Hummer's method, as detailed above) was mixed with 50 mL ultrapure water in a second beaker. Once both solutions were thoroughly mixed via stirring and sonication for 15 minutes each, the GO solution was added to the manganese precursor solution. The GO – manganese precursor solution was then thoroughly mixed via stirring and sonication. Then, the mixture was microwaved in a microwave oven (230-240 V;

~50 Hz; input power 1200W; microwave output power 700W, 2450 MHz, model MT1710) at 700 W for 4 minutes. The mixture was allowed to cool to room temperature, and then washed by centrifugation (20,000 rpm, 21°C, 30 minutes) in water at least 3 times, or until the supernatant was clear. Following washing, the GO-MnO_x material was oven-dried at 60°C overnight.

The manganese oxide – carbon black (MnO_x-CB) materials were made following exactly the same method as for MnO_x-GO but substituting Vulcan Carbon XC-72 instead of graphene oxide as the carbon support component.

The following parameters were used to synthesise the MnO_x-GO and MnO_x-CB hybrid support materials:

Table 3.1 Parameters used for deposition of manganese oxide onto graphene oxide or carbon black supports

		$KMnO_4$ (g)	**GO (or CB) (g)**	**Microwave Time (minutes)**
Chapter 5	MnO_x-GO(52)	0.30	0.10	4
Chapter 6	MnO_x-GO(50)	0.20	0.10	4
	MnO_x-GO(61)	0.30	0.15	4
	MnO_x-GO(68)	0.45	0.1	4
Chapter 7 & 8	MnO_x-CB	0.30	0.10	4

The MnO_x-GO samples are identified and differentiated from each other with the annotation MnO_x-GO(xx) where xx is the MnO_x mass % obtained from TGA.

3.2 Platinum Nanoparticle Growth

Platinum nanoparticles were grown directly on the supports through a microwave process. The Pt nanoparticle deposition was the same (aiming at 30% Pt loading), regardless of the support used with the aim to produce a 30% Pt loading to match the commercial catalysts that are used for comparison. First, 40mg of the support (GO or MnO_x-GO or carbon black) was added to 20 mL of ethylene glycol (Sigma, ≥99%) and mixed thoroughly by sonication. Then, 1 mL of 0.1 M solution of potassium hexachloroplatinate (Sigma, 98%) was added whilst still sonicating. The mixture was further sonicated to mix the precursor thoroughly throughout the solution. The solution was transferred to the microwave oven and irradiated (230-240 V; ~50 Hz; input power 1200W; microwave output power 700W, 2450 MHz, model MT1710) for 60 seconds. After being allowed to cool to room temperature, the product was washed by centrifugation in acetone at least 3 times (10,000 rpm, 21°C, 15 minutes). The resultant product was dried at 60°C for 3 hours, or until dry.

CHAPTER 4 Methods

4.1 Characterisation.

4.1.1 Transition Electron Microscopy (TEM):

Transmission electron microscopy (TEM) is a microscopy technique which utilises the wave-particle duality principle. It uses a beam of electrons behaving as a wave to generate an image of a sample, in much the same way as an optical microscope. The wavelength of the electron beam can be calculated using the de Broglie wavelength for a particle[149]:

$$\lambda = \frac{h}{m.v} \qquad (4.1)$$

Where *h* is Planck's constant, *m* is the mass of the particle and *v* is the velocity. This gives a wavelength for an electron of the order of 0.1 nm - much smaller than light - and means that much smaller features of the sample can be resolved – down to the nanometre range. This makes TEM particularly suited to imaging nanoparticles.

As the illuminating beam is composed of electrons rather than light, the TEM machine must operate under vacuum to prevent scattering of the electron beam. The electron beam is focused with a series of electric and magnetic lenses onto the sample. Once the focused beam reaches the sample, the electron beam is diffracted through the sample to the detector. A range of bright field and dark field detectors can be used, as shown in Figure 4.1, and while the structure in the image looks the same, the bright field (BF) and dark field (ADF or HAADF) images allow different information to be gathered from the sample[150].

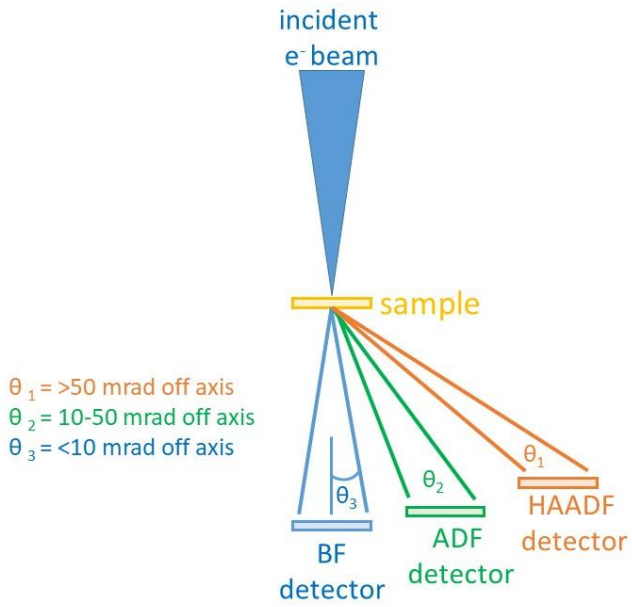

Figure 4.1 Diagram of a TEM with the different bright-field and dark-field detectors

The bright field images show the transmitted electron beam, so high mass or crystalline parts of the sample appear darker. The ADF and HAADF detectors pick up scattered electrons, so the parts of the sample which have higher mass or more sample appear bright, as these areas will scatter electrons. The advantage of dark field mode is that the original (transmitted) electron beam is not detected, so smaller crystalline features can be resolved using only the scattered electron image.

Scanning transmission electron microscope (STEM) images are based on the same principle, but the focused spot size of the electron beam is smaller, and is scanned across the sample, enabling even higher resolution to be achieved.

Energy dispersive X-ray spectroscopy (EDX) uses the electron beam to cause X-rays to be emitted from the atoms in the sample. The X-rays emitted are characteristic of the atoms present, and so an elemental composition can be obtained. An image can be obtained using

for example a silicon drift detector so that the elemental composition across the sample can be mapped.

HR-TEM (High Resolution - TEM) images were taken by Mike Fay and Julie Watts at the NMRC, Nottingham University, using a JEOL 2100F operating at 200kV, with a Gatan Orius CCD camera. STEM images were taken on the same microscope, using a high angle annular dark field (HAADF) detector, and energy dispersive X-ray (EDX) elemental mapping was obtained using an Oxford Instruments 80mm X-Max detector.

TEM images were analysed using ImageJ software. Particle size measurements were taken by measuring at least 200 particles across the x-direction of the image, using the straight line tool. This method was chosen, as the automatic intensity thresholding method in imageJ software, which is typically used to measure particle sizes computationally could not be used due to the varying contrast of the Pt particles against the supporting carbon/manganese oxide. This varying contrast is caused by an uneven background, which is due to the MnOx-GO support being a layered structure, giving rise to darker and lighter areas of the support in the background. In addition, the platinum nanoparticles have varying crystal orientations with respect to the electron beam, so some appear darker, while some appear lighter due to the varying degrees of scatter and diffraction. More than 200 particles were measured to achieve a good statistical representation of the particle size.

4.1.2 X-ray Photoelectron Spectroscopy (XPS):

X-ray photoelectron spectroscopy (XPS) is a technique used to determine the chemical composition and bonds present in a sample. The technique is based on the photoelectric effect[151], where a photon is incident on a sample surface and provided it has sufficient energy,

the photon interacts with an atom on the surface by ejecting an electron from the atom. If this electron has enough energy, it escapes the atom and is ejected out. An XPS measurement is performed using monochromatic X-rays in an ultra-high vacuum, and the ejected electrons are directed at a hemispherical analyser which measures the energy of the electrons that have been ejected[152]. These electrons will have a characteristic energy depending on the orbital that they have been ejected from. According to equation 4.2, the kinetic energy of the ejected electron depends on the binding energy of the ejected electron, work function and incident X-ray energy.

$$K.E. = h\nu - B.E. - \phi \qquad (4.2)$$

Where *K.E.* is the kinetic energy of the ejected electron; *B.E.* is the binding energy of the orbital where the ejected electron originated; ϕ is the work function of the spectrometer; and *hν* is the energy of the X-ray.

The binding energy of the electrons will change depending on the local chemical environment of the atom that the electron was ejected from. The photoelectron spectrum is measured by counting the ejected electrons over the measured energy range. By measuring the energy of ejected electrons accurately, the chemical structure of the sample can be obtained, as the XPS peaks will shift and change shape depending on the chemical structure.

As the peaks shift and change shape depending on the chemical environment of the atoms, the peaks measured from an XPS measurement must be deconvoluted to obtain the component peaks, allowing the chemical composition to be quantified.

XPS spectra for this work were obtained at the National EPSRC XPS Users' Service (NEXUS) at Newcastle University, an EPSRC Mid-Range Facility.

From 2017 onwards, XPS spectra were obtained through Harwell XPS, an EPSRC Mid-Range Facility, at both UCL and Harwell research campus.

XPS spectra were analysed using CasaXPS software, using an LF lineshape[153] for all carbon components, and a standard GL(30) lineshape for all metal/metal oxide components.

The GL(30) lineshape is used to describe a line with a mixed Gaussian and Lorentzian lineshape which is symmetric in nature[154,155]. The mixing in this case takes the form of the product between a Gaussian and Lorentzian curve, with 30% Lorentzian. GL(0) would describe a pure Gaussian curve, while GL(100) would describe a pure Lorentzian form.

The LF lineshape (Lorentzian Finite lineshape) is commonly used to describe carbon peaks[153–155]. The LF lineshape is an approximation of a Doniach-Sunjic shape, but with a finite area while still allowing for asymmetry to be introduced if required. It is a convolution of a Lorentzian with a Gaussian shape similar to the GL(30), but with the ability to define extra parameters so is more accurate in certain circumstances. The carbon peaks in this work were fitted with an LF(1,1,55,180,5) shape – which is typical for carbon XPS peaks[156]. The first and second numbers in the bracket describe α_1 and α_2, or the spread of the tail to the left and right respectively. If α_1 and α_2 are the same, there is no asymmetry. The third number extends the influence of these α terms and creates a limit of the asymmetry. The fourth number describes the size of the Gaussian to convolute the Lorentzian component with - a larger value here 'sucks in' the asymmetric tails. The final number describes how much the Gaussian and Lorentzian should be convoluted with each other.

Once complete, the XPS fits from CasaXPS were exported to OriginLab graphing software for plotting.

4.1.3 X-ray Diffraction (XRD):

X-ray Diffraction (XRD) is a technique which utilises the diffraction of X-rays off crystal planes to determine crystal structure of the sample material[157]. A monochromatic X-ray source is used. These X-rays are directed through a slit at a powder sample and diffract off at different angles depending on the crystal structure. A detector is moved in an arc around the sample to measure the intensity of X-ray signal across all angles.

The diffraction of the X-rays obeys brags law:

$$2d.sin\theta = n\lambda \tag{4.3}$$

Where λ is the wavelength of the incident X-ray, θ is the angle of incidence, n is an integer and d is the lattice parameter.

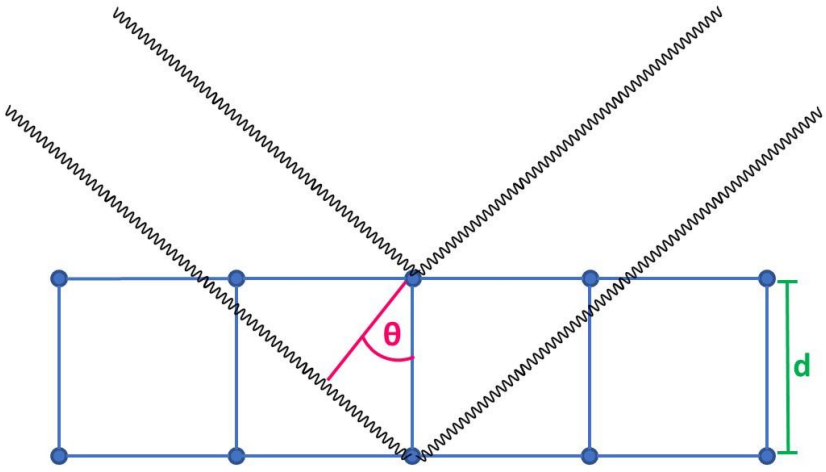

Figure 4.2 diagram of the Bragg condition for XRD peaks

When the angle of diffraction (θ or 2θ) is plotted against intensity, there will be a peak wherever this condition is fulfilled. These peaks correspond to diffraction from different crystal planes in the material structure, as shown by Figure 4.2. The crystal planes can be

defined using Miller indices denoted by h, k, and l. The 3 Miller indices can be used to describe a reciprocal lattice vector, which is orthogonal to the plane. The reciprocal lattice vector is given by: $g_{hkl} = hb_1 + kb_2 + lb_3$, and the planes are described by (*hkl*). As an example, the plane (111) for a cubic crystal lattice is drawn below in Figure 4.3:

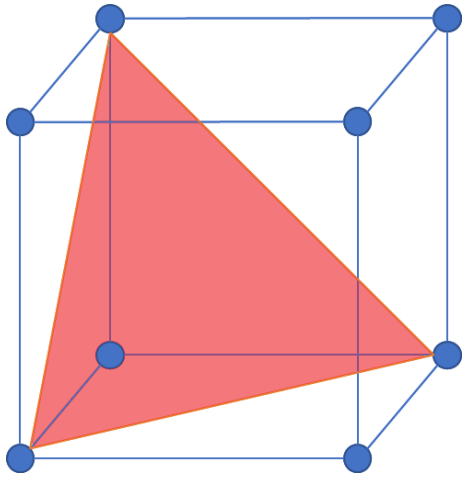

Figure 4.3 The (111) lattice plane shown by the red surface. Blue dots represent atoms.

The XRD peaks obtained can be compared to standard powder diffraction files (pdf) from JCPDS (The Joint Committee on Powder Diffraction Standards) to confirm the crystallographic structure of the material being tested.

XRD spectra for all samples were obtained using a Bruker D8 diffractometer with a Cu source. Measurements were taken from 2 to 80 ° (2θ). The X-ray energy was 1600 W and the samples were rotated during the whole measurement. The rotation of the sample ensures that the entire sample was illuminated by the X-ray slit. This provides a more reliable measurement that is more representative of the sample as a whole.

The samples were prepared by sandwiching a small amount of powder between two pieces of scotch magic tape. Scotch magic tape was selected as it is a cellulose based tape with an

amorphous structure, and gives a low background reading with no sharp peaks and only a small 'hump' around 20-30 degrees 2 θ. This is in contrast to other tapes which are made of polymers and tend to show diffraction peaks and sharp steps in the background of the spectra. This sandwich of tape and sample was compressed so that the tape and powder lay smooth. The tape-encapsulated powder was then attached to a plastic sample holder and placed inside the sample mounting stage of the XRD machine. The XRD peaks obtained were of low intensity, and broad in nature, as can be expected for nanomaterials[158–160]. In some cases, the crystallite sizes were so small that the peaks were very broad, and the intensity was so low that peaks were barely distinguishable from background.

XRD patterns were analysed for pattern matches to the JCPDS database using diffrac.suite EVA software. The patterns were subsequently plotted using OriginLab graphing software.

4.1.4 Thermo-Gravimetric Analysis (TGA):

Thermogravimetric analysis (TGA) is a measurement technique where a sample is heated and its mass measured[161]. From this, a range of different material alterations can be measured including: loss of water or solvent, oxidation, decomposition, amount of metallic catalytic residue remaining on carbon support, and weight % of fillers.

In a typical TGA measurement, a sample of the material to be tested (typically a few mg) is placed inside a small alumina crucible, on a precision balance[162]. The balance sits inside a sample chamber furnace. The atmosphere in the sample chamber furnace is controlled by flowing gas through it, allowing the material to be studied under different conditions e.g. an oxidising, reducing, or inert atmosphere. The sample is heated at a slow rate (typically 5-10°C per minute), whilst the desired gas is flowed through at a sufficient rate (typically around 50

mLmin^{-1}). The sample may lose or gain mass as it is heated, depending on the operating conditions and the process occurring. The temperature at which a mass change occurs in a given material (with given TGA parameters: heating rate, gas type, gas flow etc) is characteristic for certain processes. For example: in many materials there will be a water loss step around 100°C; and in graphene-based materials, the carbon backbone will be burnt off at 600°C in an air environment.

The TGA measurement typically reads a mass % (taking the starting mass as 100%), which can be plotted vs time or temperature. Reading off the mass change at given temperatures provides information on the composition of the material (e.g. water content, carbon content etc). By plotting the derivative of the curve, the points of maximum mass change can be read off by looking at the peaks of this derivative curve.

In all TGA measurements taken, the crucible and furnace should be clean, and a blank curve should be taken before measurement. The blank curve gives a background measurement so that the mass fluctuation of the crucible does not appear in the measurement results. In this work, a blank curve was taken before each measurement. Prior to running the blank curve, the crucible was wiped out with acetone and then placed in the TGA sample chamber furnace and heated under air flow to the max temperature (900°C) to remove any traces of organic and carbon residues[162].

TGA experiments were undertaken using a Netzsch 209 F1. 2 to 4 mg of sample was placed in an alumina crucible with lid. Air was flowed at 30 mL.min^{-1}, and with a temperature increase rate of 10°C.min^{-1}, from 20 to 900°C. At 900°C, a 10 minute isothermal hold was performed to ensure any residual mass was a consistent value.

The Netzsch Proteus analysis software was used to determine step positions and mass drops, as well as the residual mass. The data was then exported to OriginLab graphing software for plotting.

4.1.5 Inductively Coupled Plasma – Mass Spectroscopy (ICP-MS):

ICP-MS is a highly sensitive measurement that can detect most of the elements in the periodic table[163]. Exceptions to this include (but are not limited to) Oxygen and Nitrogen, as these elements are present in the plasma, and so cannot be quantified[164]. ICP-MS is used to measure the elemental composition of samples. Samples must be in liquid form, with no powder particles present else they will block the feed tube into the plasma. To achieve a liquid sample for the ICP-MS measurement, the powder materials first must be digested in dilute aqua regia. Then a small amount of sample is pumped into a plasma where it is ionised. The ionised sample is then directed to a mass spectrometer. The mass spectrometer uses an electromagnetic field to separate the ions so that they can be detected by the detector. The ICP-MS machine is capable of measuring down to parts per billion, provided suitable calibrations and standards are used, along with careful and accurate sample preparation.

In this work, to prepare the samples for ICP-MS, approximately 0.5 mg of sample powder was digested in 10 mL dilute aqua regia (16.8% HCl (Sigma, 37%) & 5.5% HNO_3 (Sigma, 70%)) by sonicating for 1 hour at 90°C. The samples were allowed to cool overnight, and then diluted to approximately 2% nitric acid concentration by adding 20 mL ultrapure water. The samples were then filtered using a filter-syringe before being pumped through the ICP-MS machine. This filtration step was to prevent any blockages of the pump tubes by any remaining powder.

Calibration standards were produced, containing Pt, Mn, and K at concentrations of 0.01, 0.05, 0.1, 0.5, 1, 5, and 0 ppm. Li, In and Ge were used as internal standards to reduce interference effects from other elements present in the sample. The potassium (K) measurement (and associated Li internal standard) was run under Helium KED (kinetic energy discrimination) to reduce polyatomic interferences. Helium KED pumps a portion of Helium into the machine to collide with the particles in the ion beam. Since polyatomic particles have a higher interaction cross section than single ions, they collide with the Helium, reducing their kinetic energy and removing the interference of polyatomic ions[164].

ICP-MS measurements were performed using a Perkin Elmer Nexion 300X, with a plasma power of 1500 W. A seaspray nebuliser connected to a cyclonic spray chamber was used for sample introduction. The sample was pumped through a peristatic pump at 0.3 $mL.min^{-1}$.

Once measured element concentrations (in ppm) were obtained, the original sample powder mass and digestion liquid volume were used to calculate the sample composition in %.

4.2 Ex-Situ Electrochemical Testing:

To test the catalyst performance ex-situ, a standard 3 electrode electrochemical cell setup and an Autolab potentiostat (PGSTAT101) was used. The counter electrode was a platinum mesh, and the reference electrode was an Hg/Hg_2SO_4 (saturated K_2SO_4) with a working potential of +0.65 vs SHE (potentials are converted to the SHE scale for convenience of comparing to literature unless otherwise stated). The working electrode was a 3 mm diameter glassy carbon disc, modified with the catalyst to be tested.

The reference electrode was tested vs a standard hydrogen electrode approximately every 4 weeks, and the potential monitored to ensure that the reference potential had not drifted.

Use of a platinum counter electrode in this case is justified, despite some controversy surrounding its use[165]. The controversy arises from the dissolution - deposition process of the platinum counter onto the working electrode, affecting the experimental results – particularly in the hydrogen evolution reaction. In the case of methanol oxidation reaction experiments, the process at the working electrode is an oxidation reaction, meaning a reducing potential is passed through the counter, so any platinum dissolution should come from the working electrode and be deposited on the counter electrode. This means that the platinum counter electrode should not affect the properties of the working electrode.

The produced Pt/MnOx-GO catalyst/support materials were tested against two commercial standard materials: Johnson Matthey HiSpec 3000 Pt/C and Johnson Matthey HiSpec 12100 PtRu/C. The PtRu/C was selected as it is a commercial standard DMFC anode catalyst, and the Pt/Ccom was selected as it is a single metal catalyst, and so is a closer comparison to the materials produced in this thesis. Hereafter, these commercial catalysts are referred to as $PtRu/C_{com}$ and Pt/C_{com} respectively.

To modify the working electrode the following method was used. First, a Nafion solution was prepared using 20 mL isopropanol (Fisher, HPLC grade), 0.5 mL Nafion 10% dispersion (Ion Power, 1100 EW, 10 wt%, water based), and 79.5 mL ultrapure water (resistivity $\geq$ 18.2 MΩ.cm; MilliQ, Millipore). Then, a catalyst ink was produced by thoroughly sonicating this Nafion solution and the catalyst powder to be tested at a concentration of 1 $mg.mL^{-1}$. Finally, 2 x 5 µL drops were deposited onto the 3 mm glassy carbon electrode and dried under a heat lamp. Once dry, the modified electrode was used in the set-up described above.

4.2.1 Electrochemical Surface Area Measurements (ECSA)

The ECSA was calculated using a widely adopted HUPD method. The catalyst was cycled in 0.5 M H_2SO_4 (Sigma, >98%) at 50 mV s^{-1} until a reproducible voltammogram was obtained (typically 30 - 50 cycles). Then, the ECSA measurement cycle is performed 3 times (to ensure reproducibility) at 20 mV s^{-1}. This measurement was repeated 3 times for each catalyst, to allow an average and error (the standard deviation) to be calculated.

4.2.2 Chronoamperometry

Chronoamperometry was performed in order to determine long term stability of the catalyst when working at a given potential. The electrolyte for these experiments was 1 M CH_3OH (Fisher, HPLC grade)/ 0.1 M H_2SO_4 (Sigma, >98%). The catalyst was cycled 50 times from 0 – 0.9 V vs SHE at 50 mV s^{-1} to ensure a reproducible voltammogram was obtained, and to measure the methanol oxidation reaction (MOR) performance of the catalyst. Then, the catalyst was held at a potential corresponding to that 50 mV beyond the oxidative (forwards) peak current (I_f) for either 1 hour or 13 hours, whilst the current was measured. Finally, a further 10 cycles, again from 0 – 0.9V vs SHE at 50 mV s^{-1}, were performed in order to measure the MOR performance of the catalyst after.

4.2.3 Cyclic Voltammetry and Degradation Cycling

Cyclic voltammetry was performed in order to determine the MOR performance of the catalyst over a long time. Initially, the catalyst was cycled at measurement conditions in order to obtain a reproducible voltammogram (typically 30 to 50 cycles). Then, the measurement was taken by cycling from 0 – 0.9 V vs SHE at 50 mV s^{-1} for 10 cycles. The peak current (I_P) for both the forwards (I_f) and backwards (I_b) MOR peak was used to calculate the forwards:

backwards peak current ratio, or I_f:I_b. A higher I_f:I_b indicates that the catalyst is less prone to poisoning, and so indicates that these catalysts will be more durable[166,167].

In the case of degradation studies, the catalyst was cycled for 1000 cycles to thoroughly degrade the catalyst. The forwards peak current ($I_{f\,Peak}$) value was plotted against scan number in order to measure the degradation of the performance of the catalyst.

CHAPTER 5 Investigation into GO vs MnOx-GO supports and their comparison to commercial catalysts.

Graphene oxide (made via a modified Hummers method) and manganese oxide- graphene oxide (made via a microwave method) – see section 3.1) supports were first tested to determine their composition and appearance before being decorated with platinum catalysts for testing.

5.1 Support characterisation

5.1.1 Graphene oxide

The graphene oxide (GO) was produced via a simple modified Hummers method[105,106] as described in section 3.1.1 in order to have some control over the type and amount of oxygen functional groups. Graphene oxide made through a modified Hummers method can have a range of properties, dependent on the functional groups present[148]. In order to determine the composition and oxidation level, a range of materials characterisations were performed.

First, ICP-MS was used in order to test for K, Mn and Pt contaminants present. Contaminant ions in graphene that has been produced chemically can impact dramatically on the performance of the material, therefore it is important to know if there are any contaminants – particularly in the case of Mn[168,169]. Table 5.1 shows that a small amount of Mn, Pt and K were present in the GO produced, however these are negligible compared to the amounts of Mn and Pt that were later added to the GO. These values may vary widely depending on the method selected to produce GO and the purity of chemicals used in its manufacture. The low

contaminant concentration reflects the high purity of the precursor chemicals and the cleanliness of the GO produced.

Table 5.1 Contaminant ion content in GO produced, values from ICP-MS.

	K / %	Mn / %	Pt / %
Graphene Oxide	0.00 ± 0.02	0.05 ± 0.03	0.04 ± 0.02

Secondly, XRD was used in order to confirm that the dried material retained its interlayer spacing and its graphene structure.

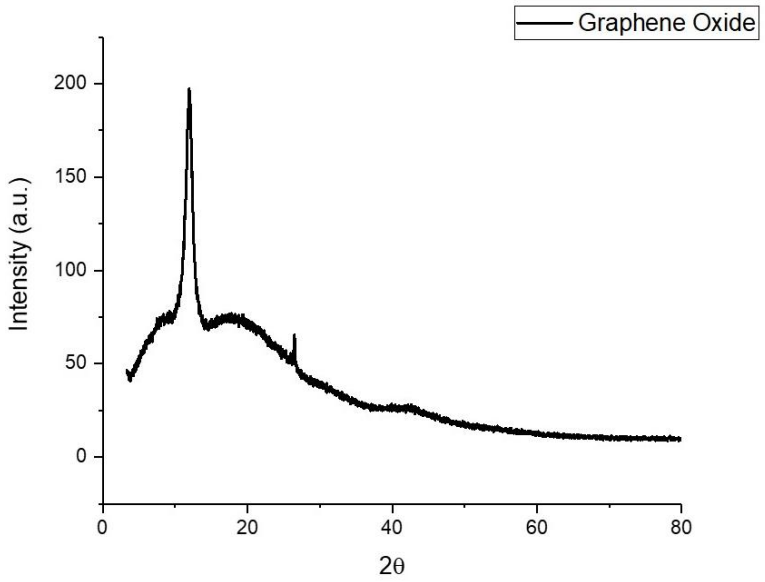

Figure 5.1 XRD spectra for graphene oxide, showing graphene and small graphite peaks.

From the XRD spectra seen in Figure 5.1, two peaks can be seen. These peaks fit with the JCPDS diffraction file shows both a broad graphene peak at 11.4° (JCPDS PDF 00-065-1528),

and a sharper graphitic peak at 26° (JCPDS PDF 00-001-0646). Using Bragg's law (Equation 5.1), the interlayer spacing, d can be calculated:

$$2d \sin\theta = n\lambda \quad (5.1)$$

where θ is the diffraction angle, n is an integer (in this instance n=1), and λ is the X-ray wavelength. By using the first peak at 11.4°, attributed to the (001) graphene peak, the interlayer spacing was calculated using the equation (5.1) to be 7.1 Å, suggesting that the GO has retained its sheet separation on drying, as the interlayer spacing for graphite is 3.35 Å[170]. The second peak at 26.6°, is attributed to the (002) graphite peak, which suggests that there are some of the layers remaining in the graphitic state, not fully exfoliated.

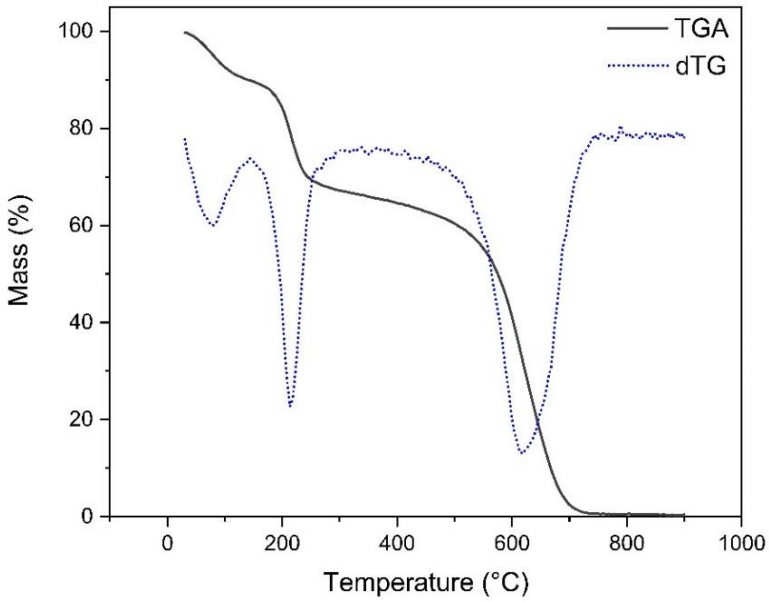

Figure 5.2 TGA curve and differential of TGA curve (dTG) showing mass losses at different temperatures for graphene oxide

Next, the oxygen content of the GO was determined by both TGA (Figure 5.2) and XPS (Figure 5.3). The TGA curve in Figure 5.2 shows three characteristic steps[106]. The first step, seen

around 100°C can be attributed to the loss of residual water molecules on the GO surface and intercalated between the GO sheets. The second step, at around 200 – 220°C is attributed to the loss of oxygen functional groups. The final step around 600°C is attributed to the burning of the carbon backbone of the GO. The lack of any final residue shows that the GO is not contaminated with any metal ions. The C:O ratio of this GO sample is calculated from the percentage weight loss at 200°C (Oxygen loss = 20%) and the percentage weight loss at 650°C (carbon loss = 66%). The C:O ratio is found to be 3.2 in this case, suggesting the graphene oxide is oxidised sufficiently[123].

The XPS wide energy survey spectra, which can be seen in Figure 5.3, shows the C:O ratio to be 3.0 in this case, which agrees with the value obtained from TGA.

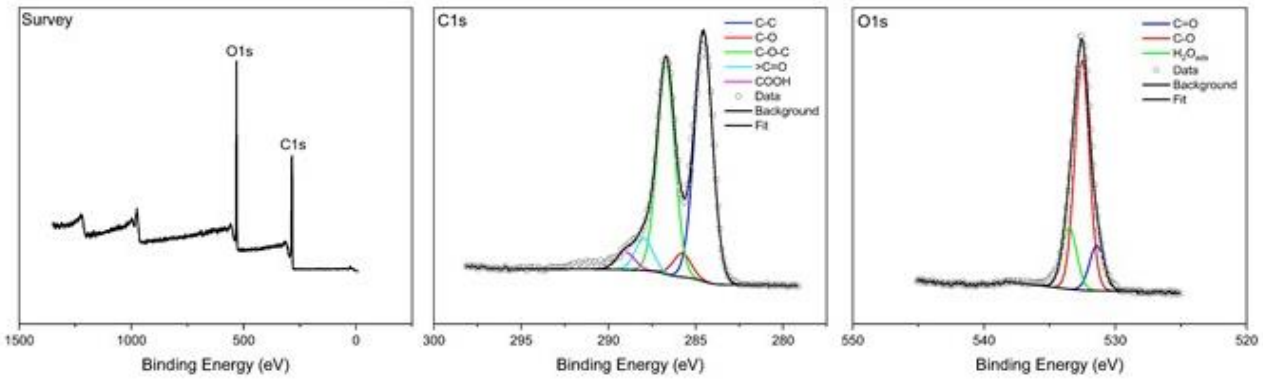

Figure 5.3 XPS Survey, C1s and O1s spectra for as-prepared graphene oxide

The high resolution C1s and O1s XPS spectra, seen in Figure 5.3, show the oxidation of the GO includes hydroxyl, epoxide, carbonyl and carboxyl oxygen functional groups. the peaks corresponding to C-C, C-O (hydroxyl), C-O-C (epoxide), >C=O (carbonyl), and COOH (carboxyl) were fitted with peak positions of 284.2 eV, 284.8 eV, 286.6 eV, 288.3 eV, 289.9 eV respectively, in agreement with literature[106]. The dominant oxygen groups on the graphene

oxide are hydroxyl and epoxide groups, with only a small contribution from carbonyl and carboxyl groups.

Figure 5.4 TEM image of as-prepared graphene oxide few layer sheets, with the lacey carbon TEM support film visible in the background.

Finally, TEM images, as shown in Figure 5.4, confirm the existence of few-layer and single layer GO sheets, with folds and wrinkles. The lacey carbon TEM support film can be seen in the background of the image.

5.1.2 Manganese oxide – graphene oxide (MnO_x-GO(52))

For this chapter, the MnO_x-GO was produced by modifying 100mg of the graphene oxide using 300 mg of the $KMnO_4$ precursor, and a microwave time of 4 minutes, as per section 3.1.2. This was then characterised through ICP-MS, TGA, XRD, XPS and TEM.

As shown in Figure 5.5, TGA was performed to determine the total MnO_x content. The residual mass % left in the TGA after heating to 900°C will only be MnO_x, as all the oxygen and carbon

from the GO will have burned by that temperature. This means that 52% of the MnOx-GO sample is MnO_x. A sharp step can be seen in the TGA curve at 380°C. This step is attributed to the graphene oxide being burned. The step looks different to the shape of the curve for un-modified graphene oxide (section 5.1.1), because the presence of the manganese oxide in the material catalyses the oxidation of the carbon structure[171]. This leads to the graphene burning step shifting to a lower temperature.

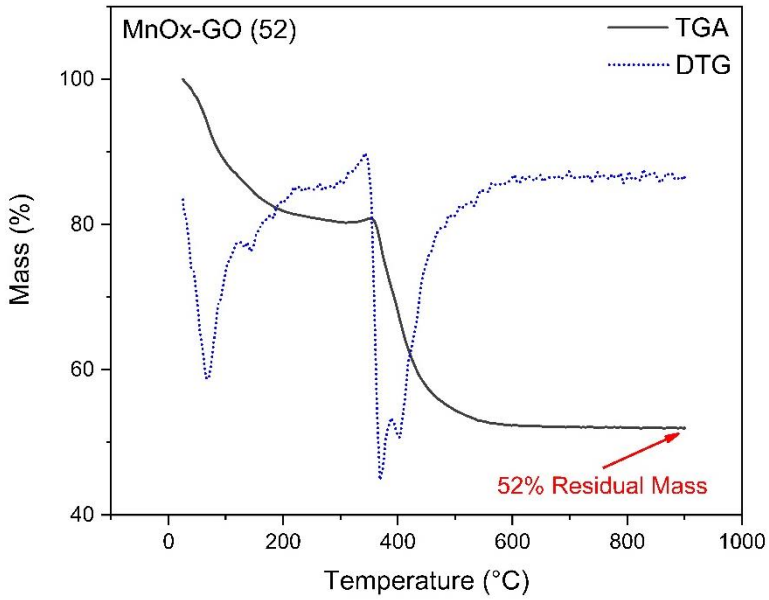

Figure 5.5 TGA curve and differential of TGA curve (dTG) showing mass losses at different temperatures and residual mass for MnO_x-GO(52)

Secondly, ICP-MS was used to determine the amount of Mn present in the sample, and to check for any potassium contaminants. The values for manganese content and potassium content can be seen in Table 5.2, which shows slightly lower amounts of metal compared to the TGA curve.

Table 5.2 Amount of Mn and K present in MnO_x-GO(52), values from ICP-MS

	K / %	Mn / %
MnO_x-GO(52)	6.6 ± 0.3	31.6 ± 0.5

ICP-MS measures only Mn in the sample, and so the value from ICP-MS is expected to be lower than the value from TGA, as the TGA % includes the oxygen contained in the MnO_x.

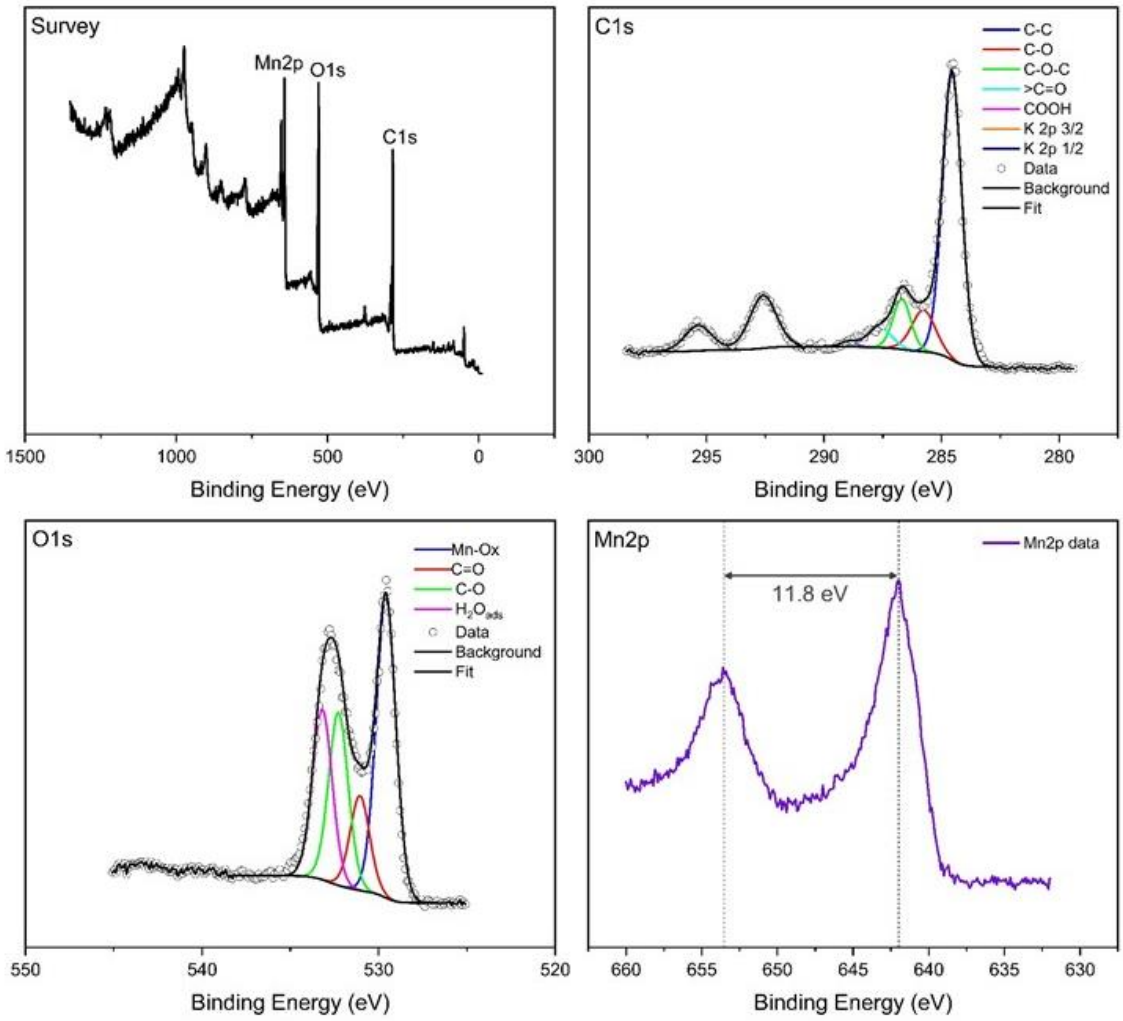

Figure 5.6 XPS Survey, C1s, O1s and Mn2p spectra for MnO_xGO(52)

The TGA and ICP-MS Mn % can be correlated by using XPS to identify the oxidation state of the Mn. XPS, which is shown in Figure 5.6, was also used to check the oxidation state of the GO, as it is expected to be reduced on addition of Mn.

The shape and peak separation of the Mn2p peak, and the absence of any satellite peaks suggests that the manganese is in a mixed oxide state of MnO_2/Mn_2O_3[172]. This information confirms the 52% MnOx - as seen from TGA, and the 31% Mn from ICP-MS, and proves that they are consistent with each other, taking into account the masses and oxidation state of the Mn.

The C1s peak was fitted with the same parameters as were used in section 5.1.1. On addition of MnO_x, there is a noticeable loss in oxygen containing groups, in particular the epoxide and hydroxyl moieties which are easier to remove. This is consistent with previous work which suggests that the MnO_x nucleates and grows on the sites of oxygen groups present on the GO[134]. In addition, a K2p peak is noticeable in the MnO_x-GO sample, indicating that a small amount of the potassium from the MnO_x precursor remains despite washing, potentially trapped in the MnO_x layered structure[173].

The O1s peak looks very similar to that of the GO O1s peak, however the C=O peak has reduced slightly, in line with the reduction of >C=O and COOH from the GO component of the material. There is also a noticeable MnO_x peak, in line with the addition of 52% MnO_x.

As shown in Figure 5.7, the XRD spectra for MnO_x-GO (obtained from a Bruker D8) shows both broad graphene peaks at 8.4° and 18.5° (JCPDS PDF 00-065-1528), and a sharper graphitic peak at 26° (JCPDS PDF 00-001-0646). This graphitic peak indicates that there has been some

re-stacking of the GO sheets during the MnO_x deposition process. There is no evidence for manganese diffraction peaks in this XRD spectra.

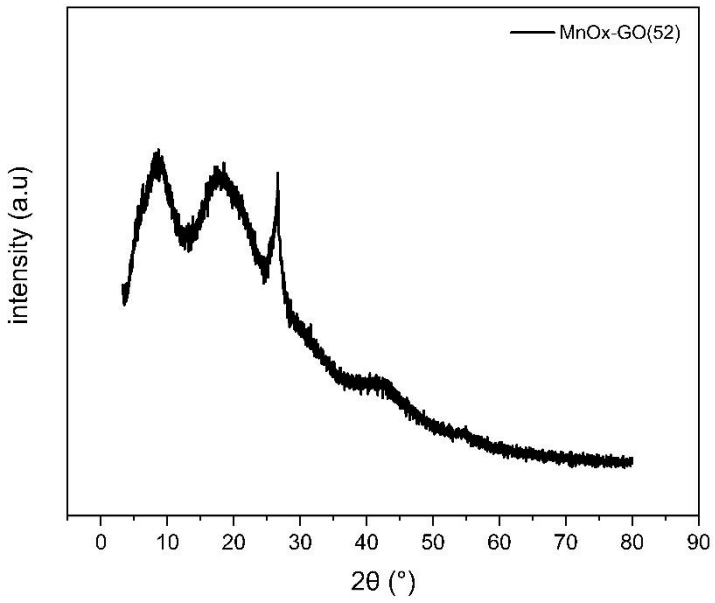

Figure 5.7 XRD spectra for MnO_x-GO(52) showing both GO and graphitic peaks

TEM imaging and the accompanying EDX mapping (Figure 5.8) shows single and few layer sheets of graphene oxide with manganese oxide uniformly distributed across the GO sheets. This confirms the XRD spectrum which shows some graphene and some graphitic structure.

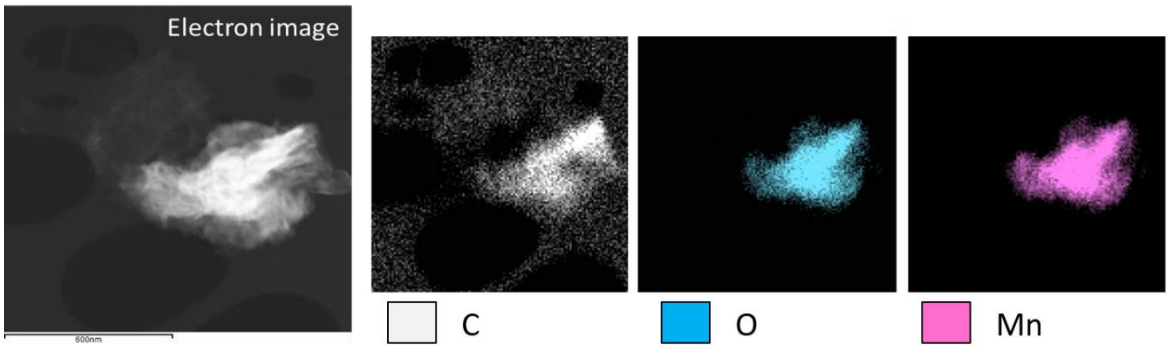

Figure 5.8 TEM image and corresponding EDX mapping showing MnO_x-GO(52) with manganese oxide uniformly distributed across the GO sheet.

HR-TEM images (Figure 5.9) confirm the presence of MnO_x patches with the interlayer spacing of 0.27 nm ± 0.02 nm, which is consistent with the (031) plane of MnO_2[174].

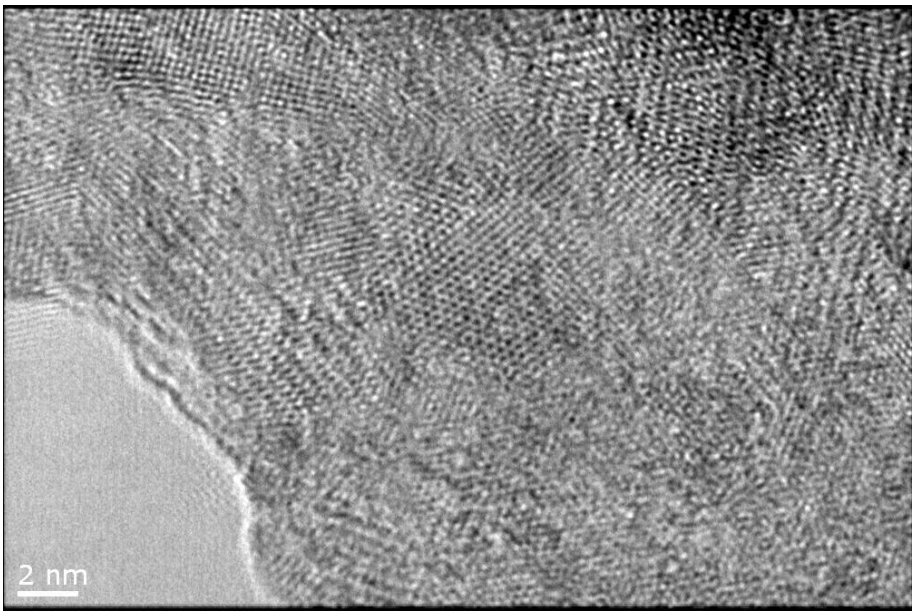

Figure 5.9 HR-TEM image showing the crystalline structure of the MnO_x deposited in the sample MnO_x-GO(52)

Although the MnO_x structure is very difficult to clearly resolve on the TEM images, it is visible as thin patches across the graphene sheets, rather than as a defined particle structure. The

MnOx presence can also be seen in the EDX mapping, shown in Figure 5.8. This thin sheet/patch structure of the MnO_x explains why there were no peaks seen in the XRD spectra for MnO_x. The TEM interlayer space is also within the range for graphene interlayer spacings[175]. However, the strong TEM image contrast suggests that this is in fact MnO_x layers that are seen, it cannot be ruled out that the structure seen is due to graphene layers.

5.2 Platinum decorated supports (Pt/GO and Pt/MnO_x-GO)

Platinum was deposited on both the GO and MnO_x-GO supports as described in section 3.2 so that they could be tested for use in a DMFC anode.

5.2.1 Characterisation

The Pt/GO and Pt/MnO_x-GO were first characterised through a range of characterisations to see what kind of Pt was deposited and the effect the Pt deposition had on the support.

First, ICP-MS was used to determine the Pt, Mn and K present in the sample. This technique was selected, as TGA would fail for the Pt/MnO_x-GO(52) sample, as the residual mass would be a combination of Pt and MnO_x and there is no way to de-convolute these masses in TGA.

Table 5.3 Pt, Mn and K present in Pt/GO and Pt/MnO_x-GO(52), values from ICP-MS

	K / %	**Mn / %**	**Pt / %**
Pt/GO	0.23 ± 0.15	0.00 ± 0.01	30.20 ± 0.50
Pt/MnO_x-GO(52)	0.41 ± 0.10	9.80 ± 0.30	31.73 ± 0.50

The ICP-MS results (Table 5.3) show that the Pt deposited is close to the expected value of 30%, based on the synthesis route selected. The percentage of Pt deposited is similar in both samples, indicating that the addition of MnO_x to the GO does not significantly affect the quantity of Pt that is deposited on the support. In addition, there is very little potassium left in both the Pt/GO and Pt/MnO_x-GO(52), suggesting that the K has been released or washed out during the Pt deposition and washing steps. For Pt/MnO_x-GO(52), the value of 10 % Mn is consistent with the proportion of Mn in the support remaining constant as MnO_2, when accounting for the addition of Pt to the sample. This means that the MnO_x is not replaced or altered when Pt is deposited.

Second, XPS was used to confirm the oxidation state of the deposited Pt, and to determine if the Pt deposition had any effect on the MnO_x or GO supports, and their oxidation. The XPS spectra for Pt/GO can be seen in Figure 5.10, while those for Pt/MnO_x-GO(52) are shown in Figure 5.11.

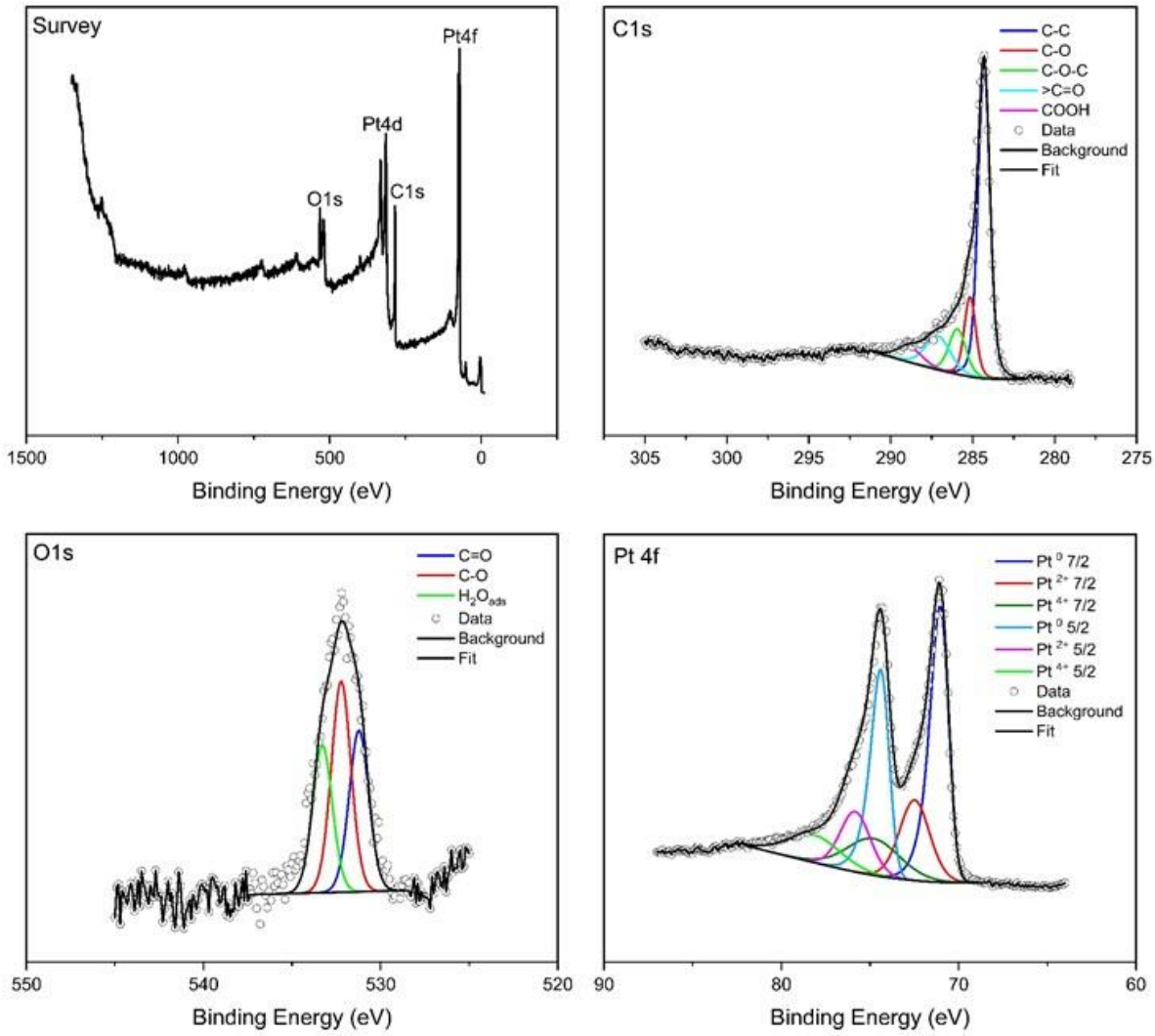

Figure 5.10 XPS Survey, C1s, O1s and Pt4f spectra for Pt/GO

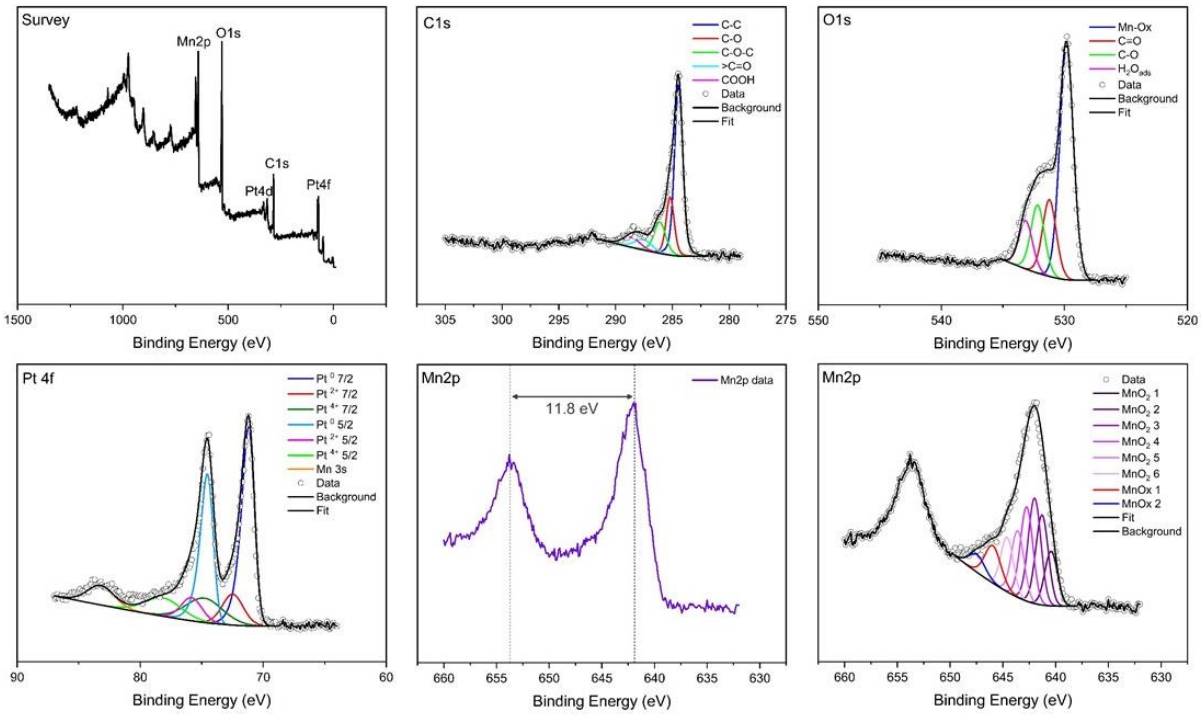

Figure 5.11 XPS Survey, C1s, O1s, Pt4f and Mn2p spectra for Pt/MnO_xGO(52)

For both Pt/GO and Pt/MnO_xGO(52), the C1s spectra show that the graphene component of the support has been reduced, with only a small amount of oxygen containing groups left, and a strong C-C peak remaining. The Pt/MnO_x-GO(52) shows a significantly more reduced graphene support, due to the two stages of reduction that this sample has undergone – first to reduce MnO_x onto the GO, and second to reduce Pt onto the MnO_x-GO.

The O1s peak shows a the C-O, C=O and H_2O_{ads} peaks as expected for the GO, but also a large Mn-O peak in the case of the Pt/MnO_x-GO(52), confirming the presence of the MnO_x in this sample.

For both Pt/MnO_x-GO(52) and Pt/GO, the Pt4f peak was analysed in terms of its Pt^0, Pt^{II}, and Pt^{IV} components. The Pt^0 component was found to account for 54% for Pt/GO and 56% for

Pt/MnO_x-GO(52) of the total Pt4f signal, suggesting that the deposited Pt nanoparticles should be a good candidate catalyst.

The Mn2p peak for the Pt/MnO_x-GO(52) sample was analysed, and again the shape and peak separation suggests a mixed oxide state of MnO_2/Mn_2O_3[172]. In addition to this shape analysis, the Mn2p peak was fitted using the standard 6-peak analysis from Biesinger et al[172], and was found to require 2 additional peaks, indicating that the MnO_x is bound to the GO and Pt.

The XRD for these two samples was run on a different machine to the other XRD spectra in this work – in this case a Bruker D2 Phaser machine, using a Co X-ray source. Therefore, the peaks are slightly shifted from the peaks from the previous sections in this chapter, which were taken using a Bruker D8 (Cu source).

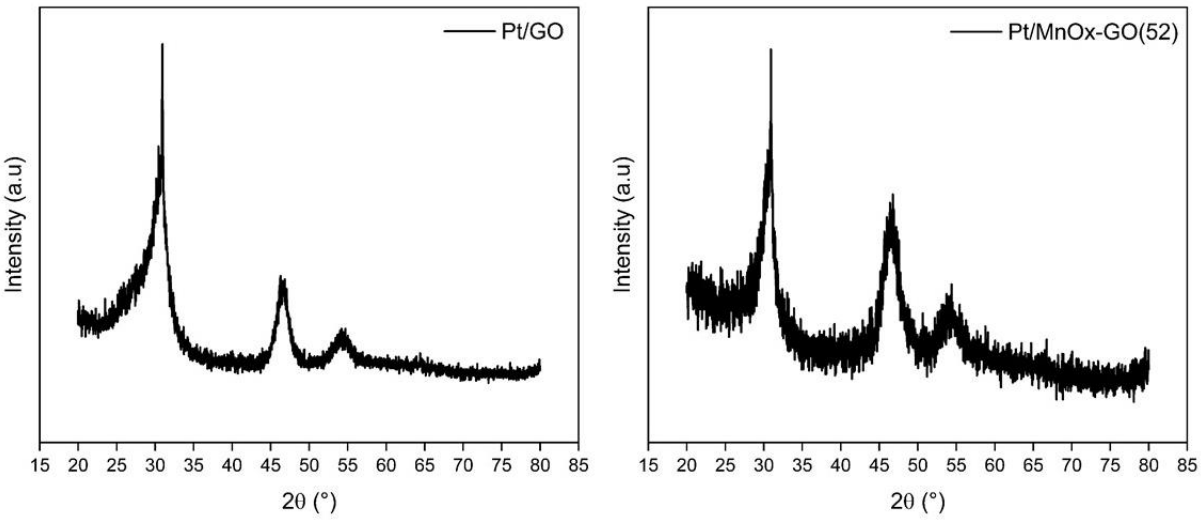

Figure 5.12 XRD spectra of Pt/GO and Pt/MnO_x-GO(52) showing clear Pt peaks

Figure 5.12 shows that clear Pt peaks can be seen at 46.5° and 54.3° 2θ, corresponding to the Pt(111) and Pt(200) crystal planes, showing that the particles grown are crystalline in nature (JCPDS pdf 00-001-1194). The peaks again are broad, indicating that these peaks originate

from nanoparticles. The graphitic peak seen previously in the supports is now seen at 30.9°, due to the Co source having a longer wavelength and shifting the peaks to a higher 2θ value compared to the Cu X-ray source used previously.

Finally, TEM images of the Pt/GO and Pt/MnO_x-GO(52) samples were taken, including HR-TEM for Pt particle sizing, and STEM-EDX maps to identify locations of C, O, Pt and Mn.

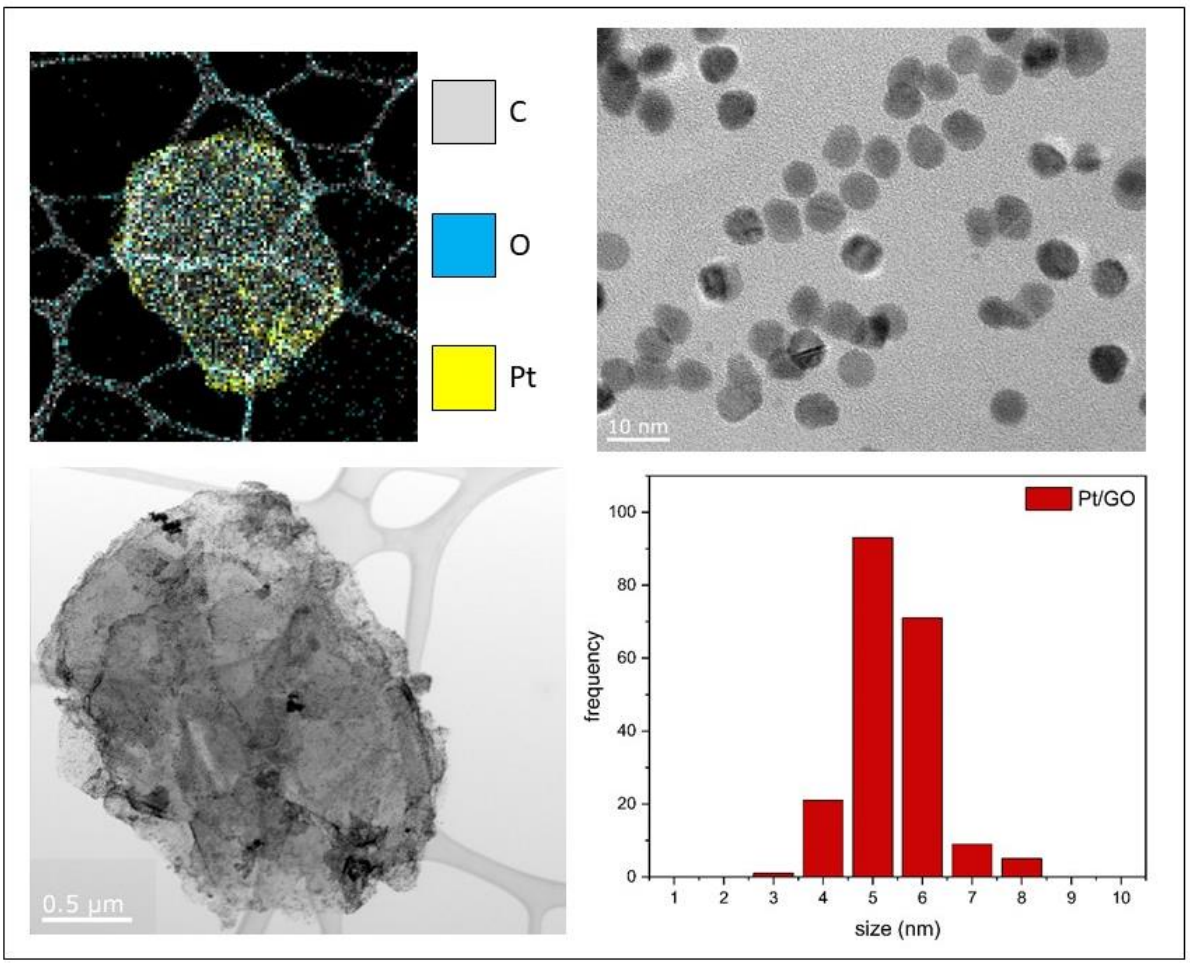

Figure 5.13 Pt/GO TEM image and EDX map, HR-TEM image and size distribution histogram.

For the Pt decorated samples, the Pt crystal structure is clearly visible, indicating a high degree of crystallinity of the as-synthesised Pt nanoparticles. The Pt/GO (seen in Figure 5.13) shows

an average particle size of 4.9 ± 0.8 nm, whilst Pt/MnO_x-GO(52) (Figure 5.14) shows an average particle size of 3.3 ± 0.5 nm.

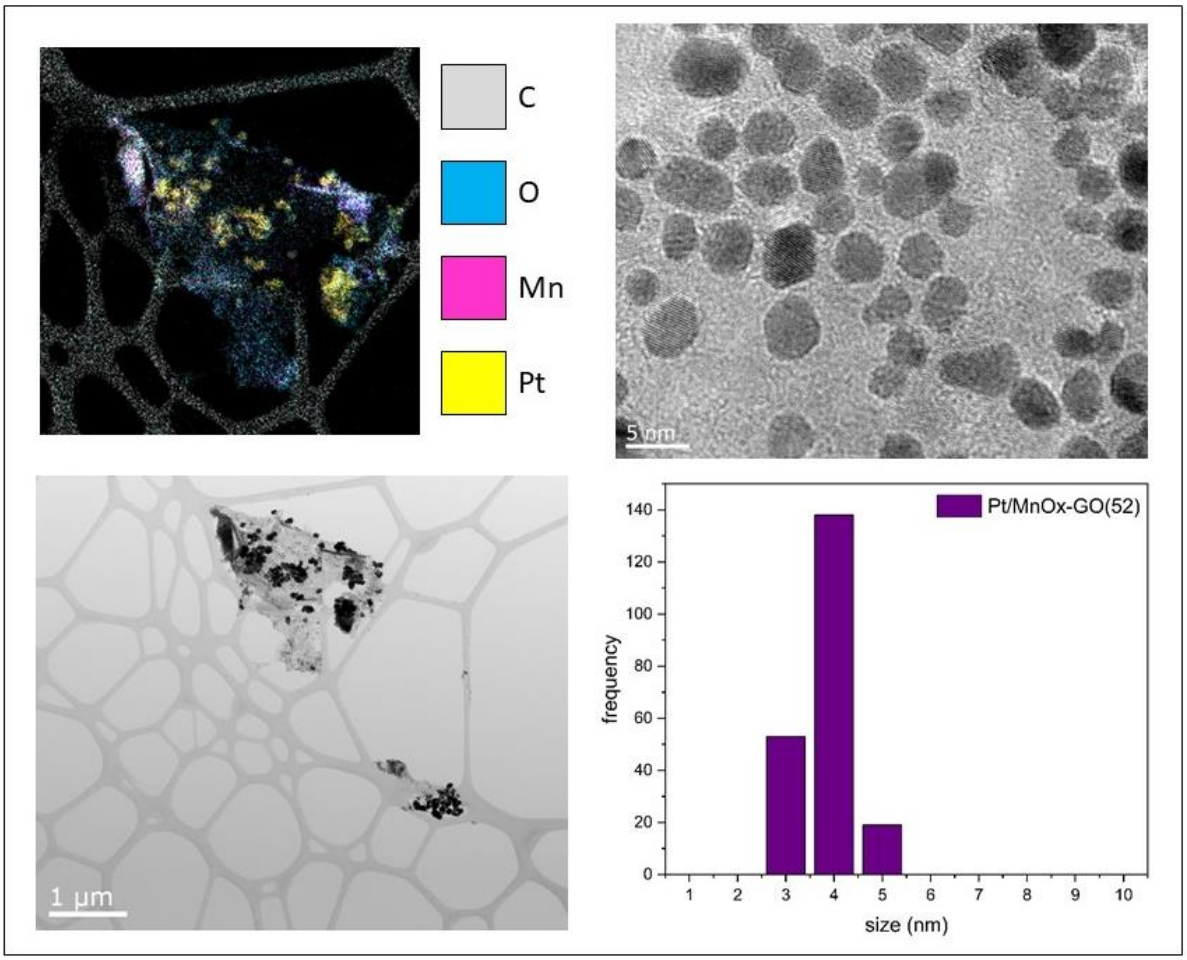

Figure 5.14 Pt/MnO_x-GO(52) TEM image and EDX map, HR-TEM image and size distribution histogram.

The distribution of sizes was also narrower for Pt/MnO_x-GO(52), showing that the addition of MnO_x gives more control of the particle size during this direct growth method. EDX mapping of the Pt/GO and Pt/MnO_x-GO(52) shows how the Pt particles and MnO_x are deposited on the GO sheets. For Pt/GO, the Pt is uniformly deposited and more regularly shaped, whereas for

Pt/MnO_x-GO(52), the position of the Pt nanoparticles appears to be associated with sites of higher Mn concentration, and the particles are more angular and less regularly shaped.

5.2.2 Electrochemical Performance of Pt/GO and Pt/MnO_x-GO

The Pt/GO and Pt/MnO_x-GO were first tested to see how well they performed the methanol oxidation reaction (MOR), and compared against two commercial standards: HiSpec 3000 Pt/C (hereafter: Pt/C_{com}) and HiSpec 12100 PtRu/C (hereafter: PtRu/C_{com}), both from Johnson Matthey. The cyclic voltammograms (CVs) are shown in Figure 5.15:

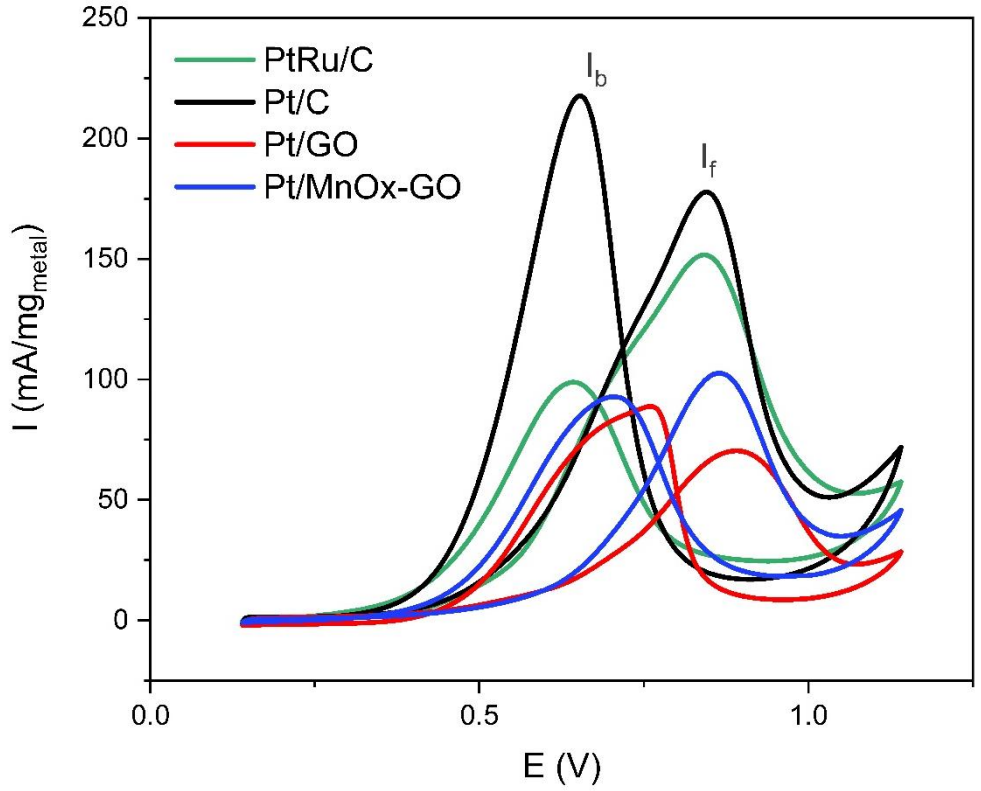

Figure 5.15 MOR plot showing I_f and I_b peaks for Pt/GO, Pt/MnO_x-GO(52), Pt/C_{com} and PtRu/C_{com}

The MOR activity of each sample was assessed by measuring the forwards : backwards peak current ratio (I_f:I_b) for all samples. This was measured when cycling in 1M CH_3OH / 0.1M H_2SO_4

solution at 50 mV/s. A higher I_f:I_b indicates that the catalyst performs better at removing the poisoning intermediates such as -CO_{ads}. The values for the I_f:I_b ratios are shown in Table 5.4, and found to be PtRu/C_{com} > Pt/MnO_x-GO > Pt/C_{com} > Pt/GO, indicating that the Pt/MnO_x-GO catalyst shows promise for being a durable catalyst, being higher than both Pt/C_{com} and Pt/GO. However, there is some dispute to the validity to using the I_f:I_b ratios to determine a Pt catalysts durability and tolerance to CO, as Chung et.al.[176] have suggested that the backwards peak is related to the oxophilicity of the metal, and not the CO tolerance. In addition, Hofstead-Duffy et.al[177] and Zhao et.al[178] suggest that the origin of the backwards MOR peak is not related to CO, and instead has the same origin as the forwards peak – oxidation of freshly adsorbed methanol. Therefore, it is important to deploy accelerated degradation cycling tests in order to validate these preliminary findings.

Table 5.4 MOR I_f:I_b and ECSA values for Pt/GO, Pt/MnO_x-GO(52), Pt/C_{com} and PtRu/C_{com}

	I_f:I_b	**ECSA / $m^2.g_{Pt}^{-1}$**
PtRu/C_{com}	1.54 ± 0.05	-
Pt/C_{com}	0.82 ± 0.05	88.7 ± 2.3
Pt/GO	0.80 ± 0.05	4.0 ± 1.3
Pt/MnO_x-GO(52)	1.10 ± 0.05	4.1 ± 0.4

The ECSA was obtained by the H_{upd} method (described in section 4.2.1) for the Pt/GO, Pt/MnO_x-GO(52) and the Pt/C_{com} samples. No ECSA was obtained for the PtRu/C_{com} sample, as the H_{upd} method is not accurate due to the differences in the Pt and Ru active sites. The

largest ECSA is obtained for commercial Pt/C, with much lower values obtained for Pt/GO and Pt/MnO_x-GO. This may be due to re-stacking of the graphene sheets during drop-casting and drying onto the glassy carbon electrode, resulting in a much lower ECSA. In addition, the size of the Pt particles on the GO and MnO_x-GO samples (4.9 nm and 3.3 nm respectively) is much larger than the commercial Pt/C HiSpec 3000, which has a maximum particle size of 2 nm. This larger size particle size of the platinum in the Pt/GO and Pt/MnO_x-GO(52) will give a much lower surface area.

In order to validate the initial durability findings from the I_f:I_b ratios, accelerated degradation cycling tests were performed. The candidate catalyst samples were subject to 1000 MOR cycles at 50 mV/s in 1M CH_3OH / 0.1M H_2SO_4 solution.

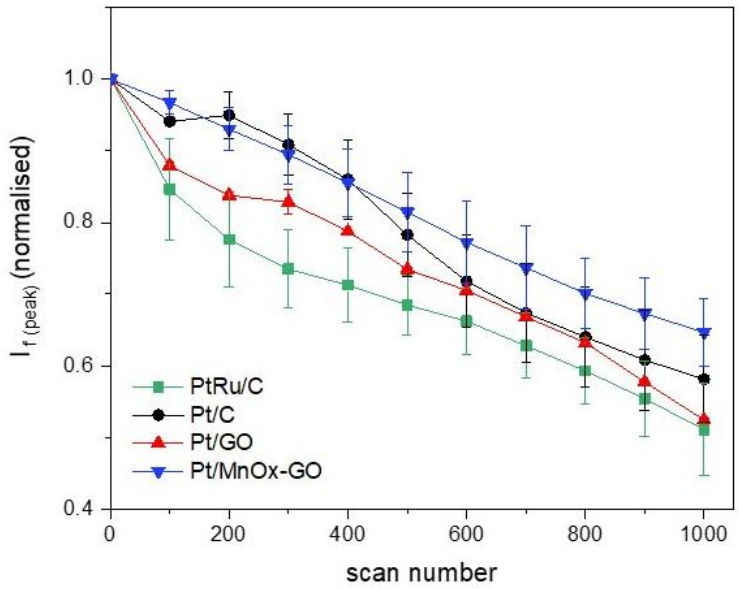

Figure 5.16 Normalised MOR $I_{f\,Peak}$ degradation over 1000 cycles for Pt/GO, Pt/MnO_x-GO(52), Pt/C_{com} and PtRu/C_{com}

The accelerated tests can be seen in Figure 5.16, where the scan number is plotted on the x-axis, and the y-axis is a normalised forwards peak current ($I_{f\,Peak}$), and in Figure 5.17, where

the current – voltage curves for MOR cycles 1 and 1000 are plotted. The Pt/MnO_x-GO(52) catalyst exhibits the highest MOR durability over cycling, since it shows the shallowest gradient in this graph. The commercial PtRu/C_{com} and Pt/C_{com} exhibit a 49 % and 42% drop in initial forwards peak current after 1000 cycles respectively, whilst Pt/MnO_x-GO(52) shows only a 35% drop. There is a large initial drop in the forwards peak current for the commercial samples, which is not the case for the GO and MnO_x-GO samples. This accounts for a large portion of the drop in activity for these commercial catalysts, and afterwards the degradation for these commercial catalysts levels out. In contrast, the MnO_x-GO degradation does not have this sharp initial drop, and instead has a constant drop in activity. It may be interesting to investigate the degradation beyond 1000 cycles for future experiments to see the effects of these different degradations over a longer time. However, it is clear that addition of MnO_x improves the durability of the Pt-GO system.

There are a number of reasons why the addition of MnO_x may improve the durability[40]. The first being that the channels in the tunnel structures of manganese oxides allows for fast ion (and proton) transport, improving the adsorption and desorption of hydrogen, and helping the adsorbed CO to be oxidised. The second reason is that hydrogen and CO are believed to be able to migrate from the Pt to the MnO_x support, leaving the Pt active sites available. Finally, MnO_2 may generate hydroxyl species, which can then help to oxidise the CO intermediates on the Pt[179]. All of these effects improve the efficiency of the indirect pathway in the MOR reaction, enabling the -CO_{ads} to be more easily removed from the Pt surface.

The gradient of the normalised $I_{f\ Peak}$ degradation line (shown in Figure 5.16) was calculated for the later part of the line from 600 to 1000 cycles, and these can be seen in Table 5.5. A

higher gradient means the degradation is faster, and a lower gradient means a slower degradation rate.

Table 5.5 $I_{f\ Peak}$ degradation gradient showing the rate of degradation of Pt/MnOx-GO and Pt/GO compared to the commercial PtRu/C_{com} and Pt/C_{com}

	Normalised $I_{f\ Peak}$ degradation gradient from 600-1000 MOR cycles
PtRu/C_{com}	-0.00038
Pt/C_{com}	-0.00034
Pt/GO	-0.00045
Pt/MnO_x-GO(52)	-0.00031

The smallest gradient is seen for Pt/MnO_x-GO(52), which indicates that this catalyst/support system exhibits the lowest rate of degradation compared to the commercial catalyst. The Pt/GO material has the highest degradation gradient, suggesting that this has the fastest degradation rate of the materials tested. This indicates that the incorporation of the MnO_x into the Pt/GO system to form Pt/MnO_x-GO significantly improves the stability of the material.

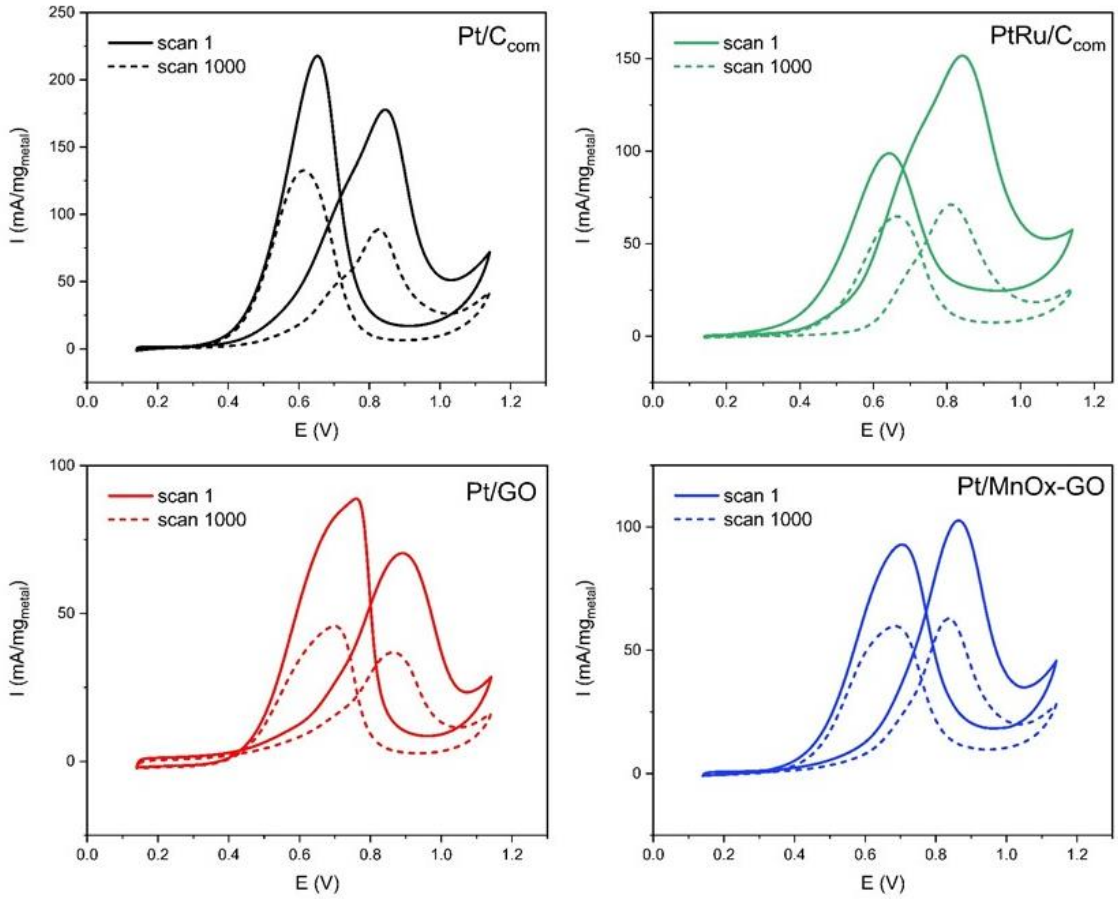

Figure 5.17 MOR degradation cycles. Shown are cycle 1 and cycle 1000 for Pt/GO, Pt/MnO_x-GO(52), Pt/C_{com} and PtRu/C_{com}

It is also important to refer back to the original degradation cycle graphs (Figure 5.17) and note that the commercial catalysts display a much greater current than the Pt/MnO_x-GO(52) and the Pt/GO catalysts. This, linked with the poor ECSA values obtained for the Pt/MnO_x-GO(52) and Pt/GO suggests that with some materials improvements such as preventing re-stacking of the GO sheets, and improvement of the Pt particle size the MnO_x-GO supports could be promising.

In addition, the shape of the MOR CV plot (Figure 5.17) does not change over 1000 cycles. The initial scans and the final scans have the same general shape, with just a lower peak current.

This reflects the degradation of the catalyst, but also indicates that the methanol oxidation pathway does not alter due to the degrading catalyst in any of the tested materials. If the methanol oxidation pathway did change over the lifetime of the catalyst, it is expected that the shape of the MOR CV plot would change, as the oxidation potential depends on the MOR pathway[34].

5.3 Conclusions

Both a graphene oxide and a manganese oxide – graphene oxide hybrid support were successfully produced, with the manganese oxide forming a MnO_2/Mn_2O_3 mixed oxide state. The manganese oxide forms as a thin, crystalline sheet structure across the graphene oxide. These were decorated with crystalline platinum nanoparticles, which for Pt/GO are 4.9 ± 0.8 nm, whilst for Pt/MnO_x-GO(52) they are slightly smaller, at 3.3 ± 0.5 nm. Both GO and Pt/MnO_x-GO(52) show that the platinum nanoparticles grow favourably on defect sites, most noticeably on folds of the graphene sheets, or on areas of high Mn content.

Whilst the ECSA for Pt/GO and Pt/MnO_x-GO(52) are very poor in comparison to the commercial Pt/C_{com} and PtRu/C_{com}, the Pt-MnO_x-GO exhibits a high durability, both when considering the forwards : backwards peak current ratio, and when looking at the performance over 1000 degradation cycles.

Some materials improvements may be made (for example preventing re-stacking of the graphene oxide sheets) in order to improve the ECSA with a view to improving the performance. When combined with the good durability exhibited by the MnO_x-GO supported Pt catalyst, this may produce a promising catalyst.

Moving forwards, the effect of the manganese will be investigated more thoroughly by altering the MnO_x content.

CHAPTER 6 Varied manganese content in MnO_x-GO supports, and its effect on the durability of the Pt/MnO_x-GO system

Since the MnO_x-GO support showed promise in Chapter 5, the Mn content on the GO was altered in order to investigate the effect of the Mn on the overall Pt/MnO_x-GO system.

6.1 Synthesis of MnO_x-GO with varied MnO_x content

The synthesis route outlined in Chapter 3 was followed, however the GO and $KMnO_4$ precursor concentrations were varied to alter the Mn content, as shown in Table 6.1. All other parameters were kept the same: mixing time, solvent, and washing steps.

Table 6.1 parameters used to produce MnO_x-GO with varied MnO_x content

	GO / g	**$KMnO_4$ precursor / g**	**Microwave time / min**	**MnO_x / %**
MnO_x-GO(50)	0.10	0.20	4	50.0
MnO_x-GO(61)	0.15	0.30	4	61.2
MnO_x-GO(68)	0.10	0.45	4	67.8

TGA showed the percentage of MnO_x in the support was increased in approximately 10% intervals: 50%, 62%, 68%.

6.2 Characterisation of MnO_x-GO with varied MnO_x content

After initial testing by TGA, the MnO_x-GO was characterised by ICP-MS to determine more accurately the Mn content in the samples.

Table 6.2 Pt, Mn and K present in MnO_x-GO(50), (61) and (68), values from ICP-MS

	K/ %	**Mn / %**	**Pt / %**
MnO_x-GO(50)	5.09 ± 0.20	26.10 ± 0.50	0.00 ± 0.01
MnO_x-GO(61)	6.04 ± 0.20	33.72 ± 0.50	0.00 ± 0.01
MnO_x-GO(68)	7.20 ± 0.20	42.73 ± 0.50	0.00 ± 0.01

ICP-MS – results seen in Table 6.2 shows that there is no Pt present in the MnO_x-GO supports of varying Mn content. It can be seen that the Mn % increases on increasing $KMnO_4$ precursor in the synthesis solution, however there is also a notable increase in the K content as the Mn content increases. This indicates that the potassium is not fully removed on washing the samples, and may be trapped in the hollow tunnel structures or layers formed by manganese oxides[88,173].

Secondly, XPS was performed on these MnO_x-GO supports to determine the oxidation state of the Mn and C in the MnO_x-GO support prior to addition of Pt catalyst nanoparticles, with these spectra shown in Figure 6.1.

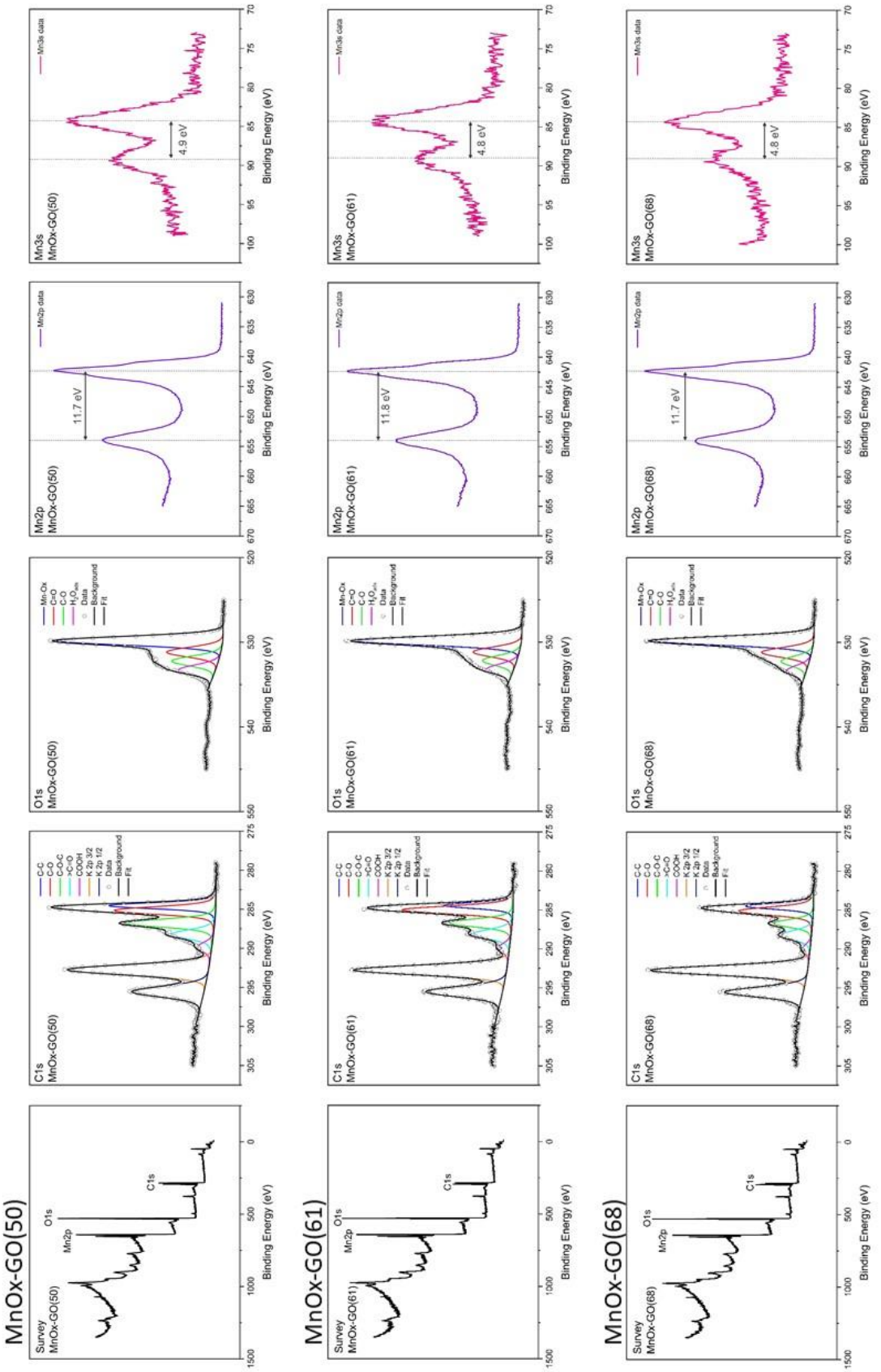

Figure 6.1 XPS survey, C1s, O1s, Mn2p and Mn3s spectra for MnO_x-GO(50), (61), and (68)

The XPS survey spectra all show the main components of the material: C1s, O1s, and Mn2p. Also evident on these survey spectra (though not labelled) are other Mn peaks, and some K peaks. There is no evidence for any other contaminants.

The C1s spectra[106] all show that the GO has only been partially reduced, as previously seen in Chapter 5. All contributing peaks except the C-C peak have been reduced (hydroxyl, epoxide, carbonyl and carboxyl), but there remains a moderate contribution from the hydroxyl and epoxide groups, however even these have been reduced somewhat from that of the GO. The C1s spectra also shows a large K2p peak, indicating that there remains some potassium even after washing, as expected from the ICP-MS results. Again, this is believed to have remained after washing as it is trapped in the MnO_x tunnel structure.

The O1s peaks all show a strong Mn-Ox peak, indicating that there exists a substantial amount of Mn-O bonds. Also evident are the C-O and C=O bonds, and water. The water will be present, as the GO is highly hydrophilic, and so even after drying, retains some water in its structure.

Finally, the Mn2p and Mn3s peaks all indicate that the MnO_x is deposited as predominantly MnO_2. The Mn2p peak separation is 11.8 eV or 11.7 eV for all samples, and when coupled with the peak shape, this indicates a Mn_2O_3/MnO_2 mixed oxide. The Mn3s peak which is more accurate at determining the oxidation state of manganese[180], shows a peak separation of 4.7 eV or 4.8 eV, which is much closer to the value for MnO_2 (4.7 eV) than Mn_2O_3 (≥ 5.3 eV), indicating that the MnOx is predominantly deposited as MnO_2[172].

XRD was performed to determine if there was any crystallinity to the MnO_x and to determine the interlayer spacing of the GO sheets for all 3 MnO_x loadings, shown in Figure 6.2.

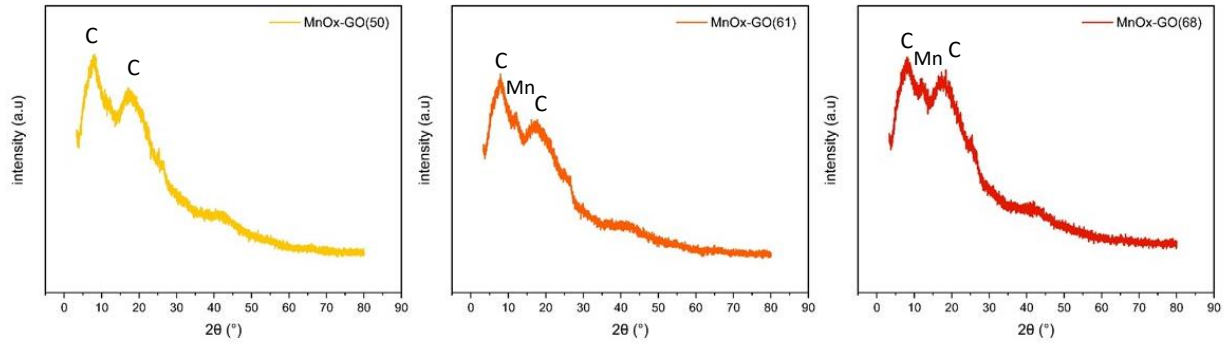

Figure 6.2 XRD spectra for MnO_x-GO(50), MnO_x-GO(61), and MnO_x-GO(68)

The two broad graphene peaks at 8.4 and 18.5° are visible for all 3 samples (JCPDS PDF 00-065-1528). There is no evidence for a graphite peak as was the case in Chapter 5, indicating that the sheets have not re-stacked on drying in this case. However, for the MnO_x-GO(61) and even more so for the MnO_x-GO(68), there is a small peak appearing between these 2 graphene peaks at 12°, which can be attributed to MnO_2 (JCPDS PDF 01-074-4231). The intensity of this peak increases in line with an increase of MnO_x content, confirming the presence of MnO_2 in these supports.

6.3 Platinum deposition on MnO_x-GO with varied MnO_x content

Platinum nanoparticles were deposited on the MnO_x-GO supports, using an identical Pt deposition procedure for each support. The aim was to deposit 30% of Pt nanoparticles on each support to compare to similar levels used in commercial DMFC catalysts, using 40 mg of support in 20 mL ethylene glycol and 1 ml of 0.1 M solution of potassium hexachloroplatinate, which was thoroughly mixed, and microwaved for 60 seconds. These were named after the supports on which the catalysts were grown, Pt/MnO_x-GO(51), Pt/MnO_x-GO(61), and Pt/MnO_x-GO(68).

The first characterisation technique employed was ICP-MS. This was to determine the Pt loading on each support and the results can be seen in Table 6.3.

Table 6.3 Pt, Mn and K present in Pt/MnO_x-GO(50), (61) and (68), values from ICP-MS

	K / %	**Mn / %**	**Pt / %**
Pt/MnO_x-GO(50)	0.26 ± 0.20	8.52 ± 0.50	32.34 ± 0.50
Pt/MnO_x-GO(61)	0.26 ± 0.20	11.47 ± 0.50	26.55 ± 0.50
Pt/MnO_x-GO(68)	0.25 ± 0.20	15.27 ± 0.50	23.96 ± 0.50

For all 3 samples, the level of potassium has dramatically decreased, to a negligible level. This suggests that the Pt deposition process and subsequent washing steps enable the potassium to be removed from the tunnel structures of the MnO_x in the support. The amount of platinum deposited decreases with increasing Mn content in the support. This indicates that the MnO_x inhibits the deposition of the Pt on the support because the Pt deposits on defect sites, and the MnOx layer has fewer defects than the highly defected reduced graphene oxide support.

The XPS for these three Pt/MnO_x-GO samples (Figure 6.3) shows the oxidation state of the deposited platinum, in addition to showing how the GO and MnO_x components of the support are affected by this deposition step.

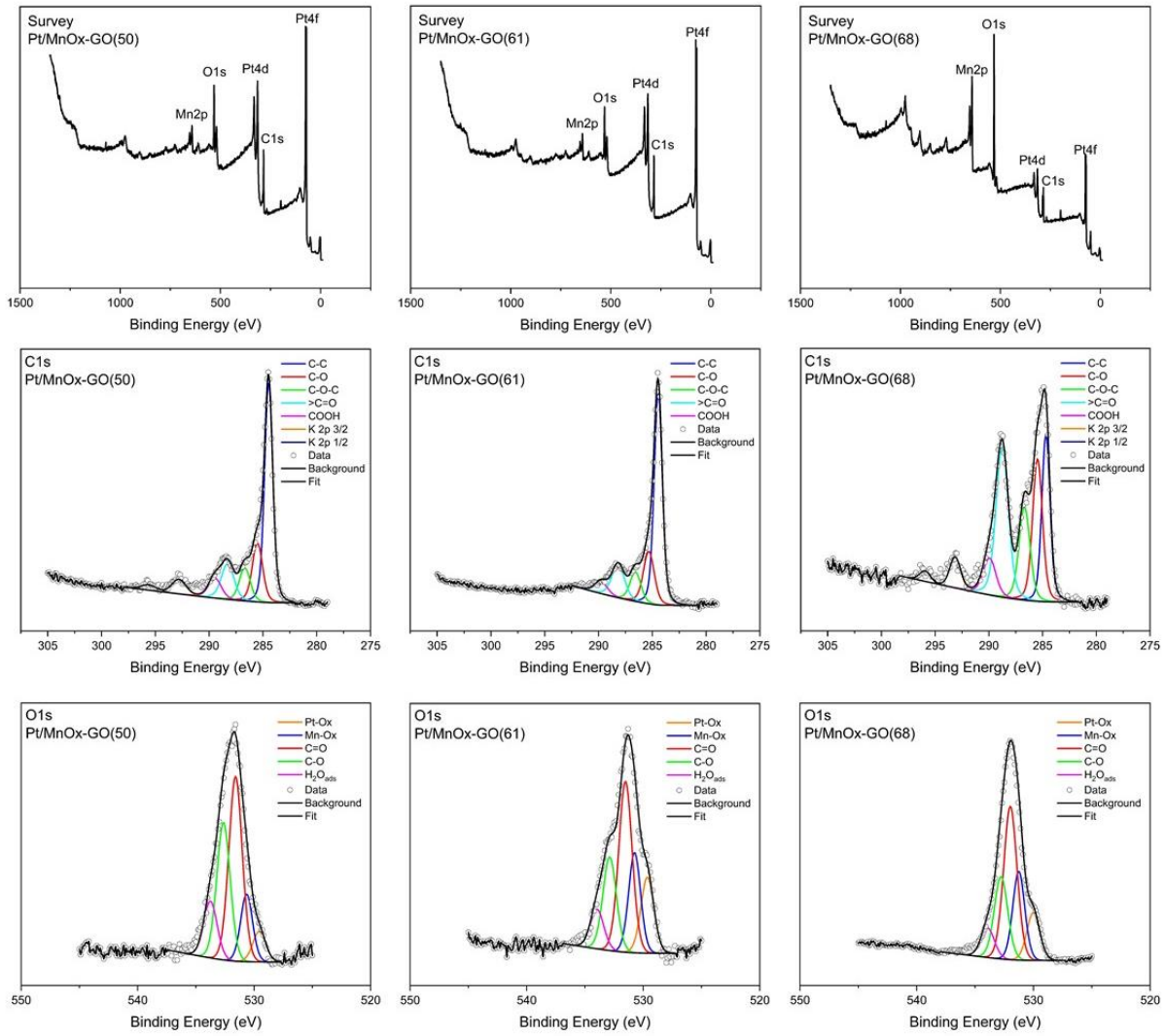

Figure 6.3 XPS survey, C1s, and O1s spectra for Pt/MnO_x-GO(50), (61), and (68)

The survey scan shows that C, O, Mn, and Pt are present in all samples despite their varying Mn content. The Mn2p peak is much more noticeable for Pt/MnO_x-GO(68), the sample with the highest Mn content. The survey scans also show that there are no other major contaminants present in any of the samples.

The C1s spectra show a variance in the carbon component of the support between the Pt/MnO_x-GO(68) vs Pt/MnO_x-GO(61) and (50). The carbon in the Pt/MnO_x-GO(50) and Pt/MnO_x-GO(61) has been further reduced from the MnO_x-GO(50) and (61) supports, with

large reductions in the hydroxyl and epoxide peaks. The potassium K2p peaks which were very clear in the XPS C1s spectra for the supports have been dramatically reduced, to a very small amount, as evidenced by the ICP-MS results. This indicates that the potassium which was previously trapped in the Mn tunnel structures has been able to be released during the Pt deposition and washing steps. For the Pt/MnO_x-GO(68) sample, the C1s signal from this sample is not as high as for the previous two samples, as is evident from the higher background noise seen outside the fitted area. The carbon in this sample has not been as highly reduced, with a large carbonyl peak still present. The potassium peak that was also present in the blank MnO_x-GO(68) support has been diminished, again indicating that this has been removed during the Pt deposition and washing stages. The component C1s peaks from this Pt/MnO_x-GO(68) suggest that the high manganese content hinders the reduction of the GO component of the support. This may be due to the MnO_x sheet-like structure covering the GO surface more completely, impeding the removal of the GO oxygen functional groups.

The O1s spectra for all 3 samples are made of a very similar set of component peaks. The predominant signal is from the C-O peak, with contributions from the C=O and Mn-O_x peaks. There are small contributions from the Pt-O_x peak, and H_2O, which is retained in the GO sheets due to its hydrophilic nature.

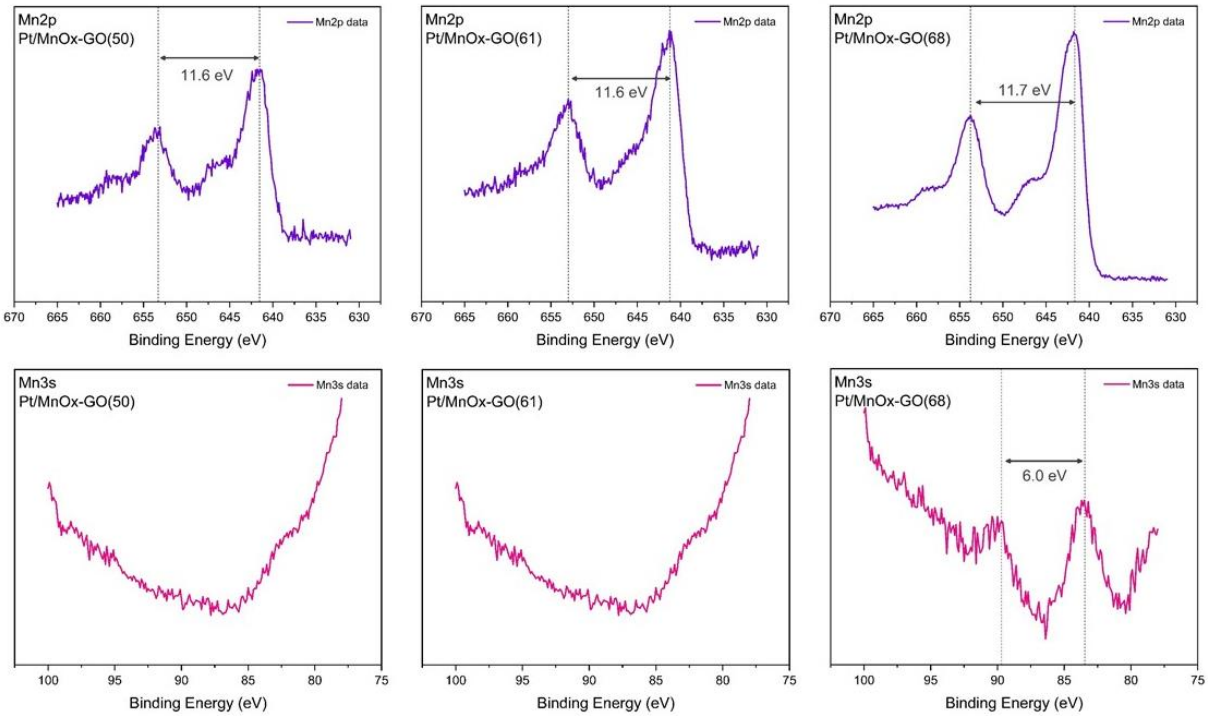

Figure 6.4 Mn2p and Mn3s spectra for Pt/MnO_x-GO(50), (61), and (68)

The Mn 2p and Mn3s peaks (highlighted in Figure 6.4) were used to identify the Mn oxidation state[172]. The Mn2p peak is present and very similar for all samples. The peak shape at the top of the 3/2 peak and the energy split suggests that the MnO_x is in the MnO_2 form, however the existence of the shoulder around 647 eV may be due to the MnO satellite peak, indicating that this MnO_x is deposited in a mixed oxide state. Although the Mn3s peaks are more accurate for determining the oxidation state for the manganese[180], the Mn3s peaks were not visible for the lower MnO_x content samples, this may be due to the lower Mn content in these, or simply due to the low intensity Mn3s peak not being visible through the noise next to the much more intense Pt4f peak. For the highest MnO_x content – Pt/MnO_x-GO(68) sample, the Mn3s peak is just visible, and the peak separation indicates that the MnO_x is deposited as MnO. This may explain the minimal reduction of the carbon in the support for this sample, as the Mn seems to have reduced rather than the GO component of the support.

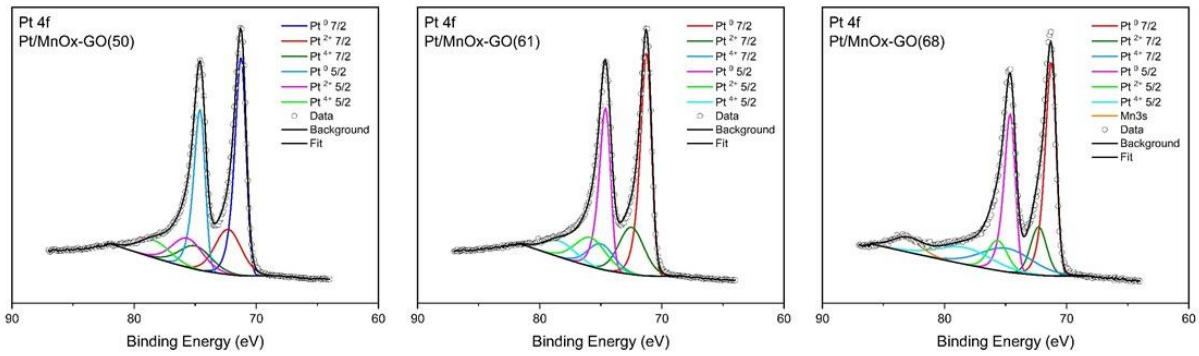

Figure 6.5 Pt 4f spectra for Pt/MnO_x-GO(50), (61), and (68)

The Pt 4f spectra shown in Figure 6.5 all show Pt^{II} and Pt^{IV} contributions, however the Pt^0 component is the largest component for all samples. This Pt^0 corresponds to Pt metal, which is best for MOR, meaning that these Pt nanoparticles are good candidate catalysts.

Next, XRD spectra were obtained for all three Pt decorated samples in order to determine the crystallinity of the deposited Pt nanoparticles, and to see if the Pt deposition had affected the MnO_x-GO supports. These are shown in Figure 6.6.

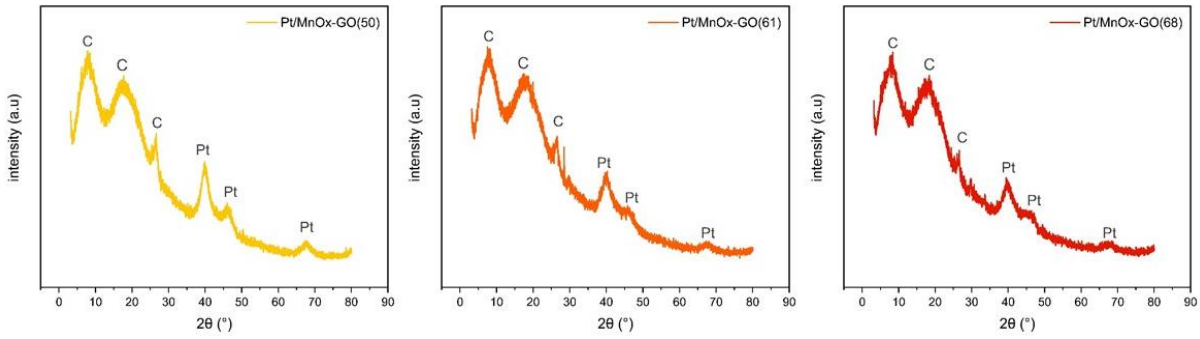

Figure 6.6 XRD spectra for Pt/MnO_x-GO(50), Pt/MnO_x-GO(61), and Pt/MnO_x-GO(68)

The broad graphene peaks are still visible on these 3 Pt decorated MnO_x-GO supports at 8.4° and 18.5° 2θ (PDF 00-065-1528). The small peak which appeared at 12° for the blank MnO_x-GO supports, attributed to MnO_2 (JCPDS PDF 01-074-4231) has appears to have disappeared

possibly due to its low intensity when compared to other components on the material. This peak was only very small compared to the GO peaks in Figure 6.2, so when the much stronger Pt peaks are seen in these XRD patterns, the intensity of the MnO_x peak is too low for it to be visible. There is a graphitic peak around 26° (JCPDS PDF 00-001-0646) on all of these Pt/MnO_x-GO samples, which was not present for the blank supports, indicating that through the process of Pt deposition, washing and a further drying stage, the graphene sheets have begun to re-stack and form some graphite structures, or few-layer graphene structures. This is expected to impact on the ECSA of these materials. Three clear platinum peaks can be seen at 40°, 46°, and 68° 2θ (JCPDS PDF 00-001-1194), indicating that the deposited platinum nanoparticles are crystalline, and the MnO_x content in the support does not drastically affect the crystallinity of them.

Finally, TEM images of the Pt/MnO_x-GO(50), (61), and (68) samples were taken, including HR-TEM for Pt particle sizing, and STEM-EDX maps to identify locations of C, O, Pt and Mn.

For Pt/MnO_x-GO (50), the EDX map (Figure 6.7) shows Pt covering the whole surface, with a correlation between the Pt deposits and the Mn deposits.

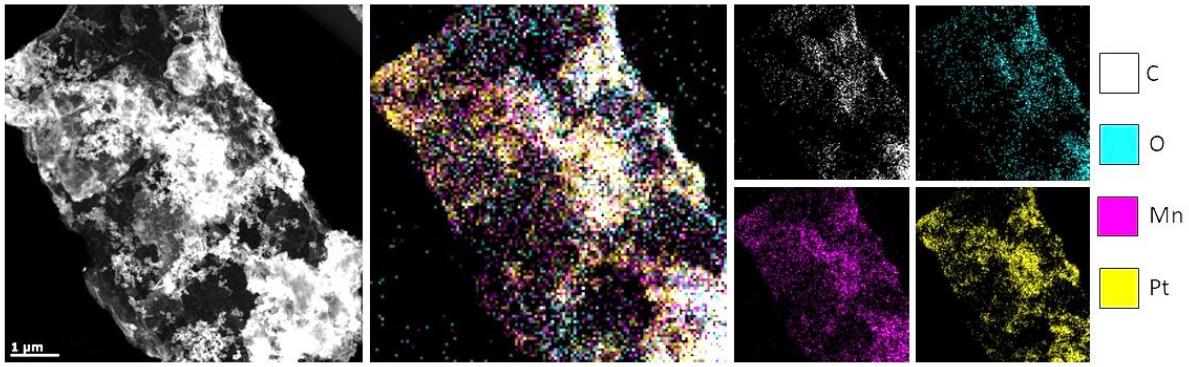

Figure 6.7 HAADF-STEM image and corresponding EDX maps of Pt/MnO_x-GO(50)

There are some parts of the sheet that are not in focus, which arises from the 3D nature of this sheet. When coupled with the EDX maps which show a much more intense signal in these de-focussed areas, this suggests that there are some areas that are much thicker than others on the sheet. The positions of the Mn and Pt deposits show that the Pt deposits favourably on the Mn, which is believed to be due to the higher presence of defect sites in these locations.

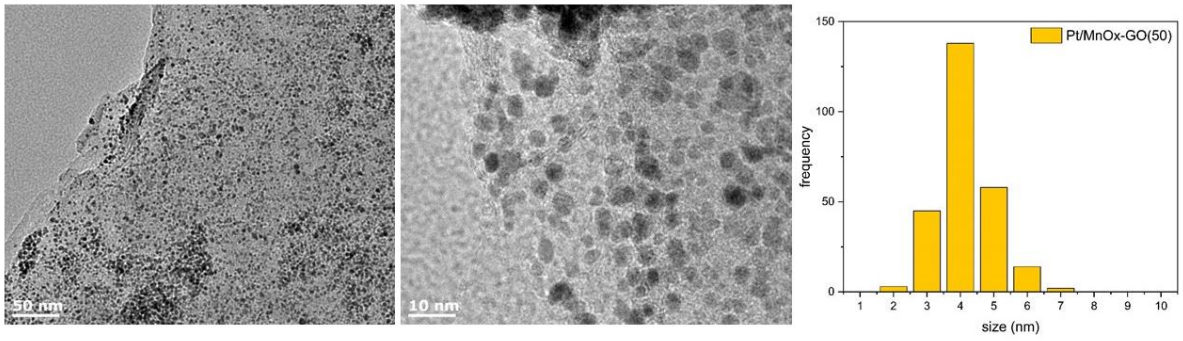

Figure 6.8 HR-TEM images of Pt/MnO_x-GO(50) and the corresponding particle size histogram

The HR-TEM images as seen in Figure 6.8 show Pt particles across the whole of the sheet, which indicates that while Pt will grow across the whole of the sheet. The bright intensity of Pt shown in the EDX map is due to a higher concentration of particles in this location, and not

due to a lack of Pt elsewhere. Such a highly concentrated patch of Pt particles can be seen in the left image of Figure 6.8 towards the bottom.

The particle sizes of the Pt/MnO_x-GO(50) were measured using a sample of 260 particles, giving an average size of 3.7 nm ± 0.7 nm, which is similar to the Pt/MnO_x-GO(52) sample from Chapter 5 of 3.3 nm, indicating that the Pt deposition onto MnO_x-GO is relatively consistent when using supports with similar MnO_x loadings (in this case approximately 50%).

For Pt/MnO_x-GO(61), the images show some very thick parts of many layers, and some thinner parts of few or single layer MnO_x-GO sheets.

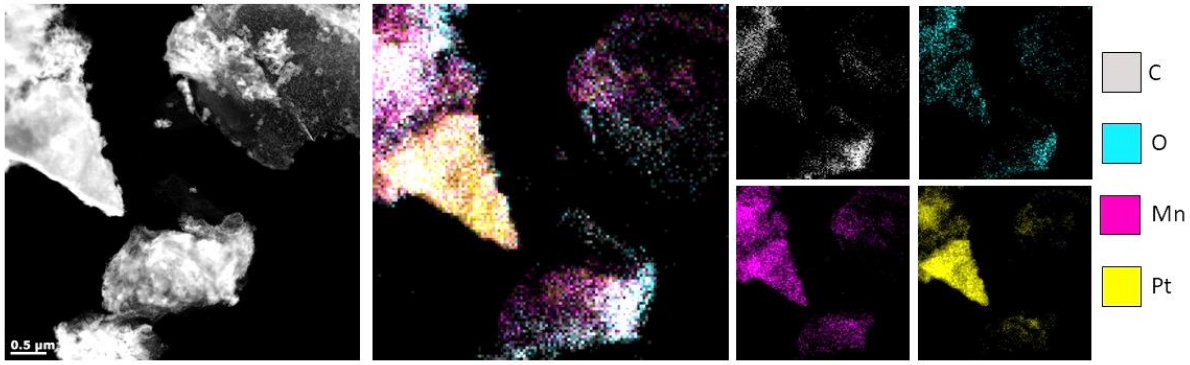

Figure 6.9 HAADF-STEM image and corresponding EDX maps of Pt/MnO_x-GO(61)

There are 3 sheets contained within the EDX map for Pt/MnO_x-GO(61) (Figure 6.9), all showing a similar story. The sheet at the bottom centre of the images is perhaps the easiest to distinguish the arrangement of elements, as it is a thinner sheet. There is a large GO component of this sheet towards the bottom right, identified by a brighter intensity in the C and O EDX, whilst the Mn and Pt are more intense towards the top left of this sheet, indicating that the Mn deposits preferentially on defect GO sites (sites where the GO has reduced, leaving defects) and the Pt again deposits preferentially onto defect sites, which in the case

of the MnO_x-GO support is sites of more MnO_x, such as step edges or folds in the sheet. A similar pattern is observed on the other 2 sheets contained within this EDX map, with the C and O being more intense in one area, and the Pt and Mn being more intense in another.

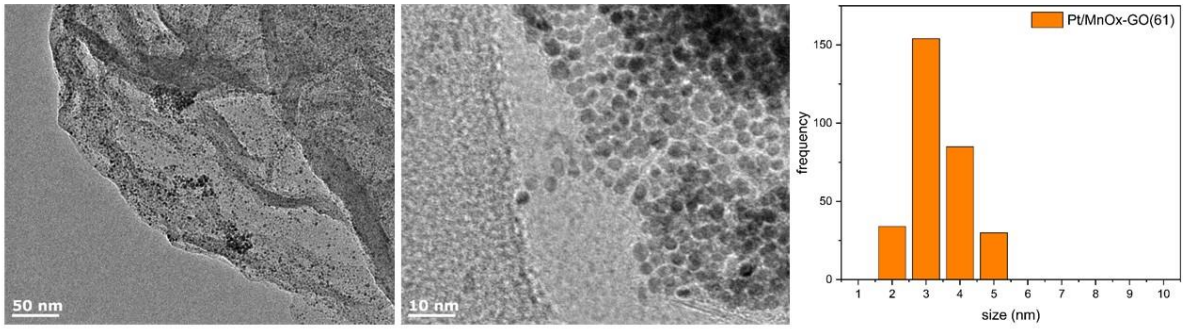

Figure 6.10 HR-TEM images of Pt/MnO_x-GO(61) and the corresponding particle size histogram

The HR-TEM image to the left in Figure 6.10 shows the deposition of Pt particles on Pt/MnO_x-GO(61) is again across the whole sheet, and clearly shows some clustering of Pt particles at folds and wrinkles in the sheet. The second image (centre) shows a very dense accumulation of particles towards the top right of the image, and some more disperse areas towards the left of the image. These dense accumulations exist across the sheet, however there are also many areas of disperse Pt particles. The very left hand side of the image is the carbon TEM support film.

The particle sizes of the Pt/MnO_x-GO(61) were measured using a sample of 276 particles, giving an average size of 2.8 nm ± 0.6 nm, which is smaller than Pt/MnO_x-GO(50) 3.7 nm, indicating that the Pt deposition onto MnO_x-GO(61) has been altered by the MnO_x content on the support and caused smaller Pt nanoparticles to grow.

EDX maps shown in Figure 6.11 show that the deposition of Platinum goes across the whole sheet on the Pt/MnO_x-GO(68), however again there are noticeable groups of densely packed particles, as was the case for other materials in this chapter.

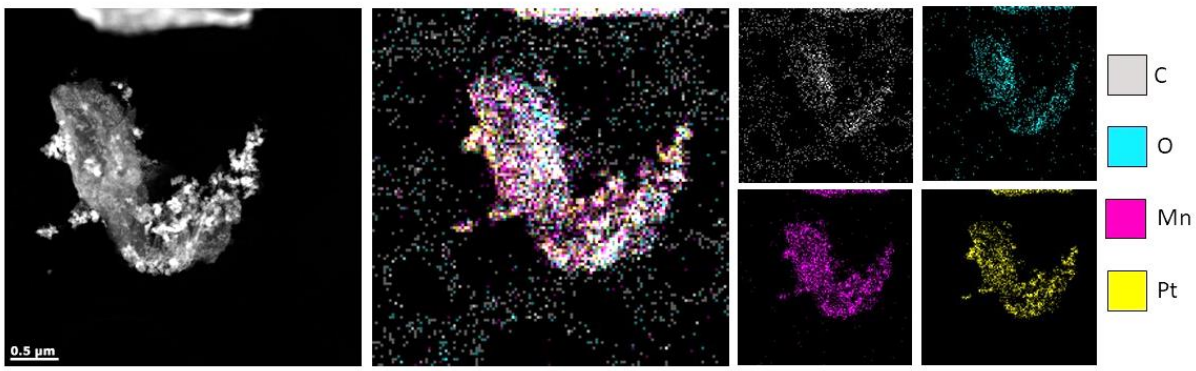

Figure 6.11 HAADF-STEM image and corresponding EDX maps of Pt/MnO_x-GO(68)

The HAADF-STEM image (on the right of Figure 6.11) shows some clear bright patches across the sheet, particularly at the edges. These coincide with areas of Pt and Mn in the EDX maps. Like the previous Pt/MnO_x-GO(50) and Pt/MnO_x-GO(61), the Pt map shows a very similar pattern to the Mn map, indicating that the Pt deposits preferentially onto areas where there is more manganese. Again, it is believed that this is due to the larger amount of defect sites such as steps and edges present here.

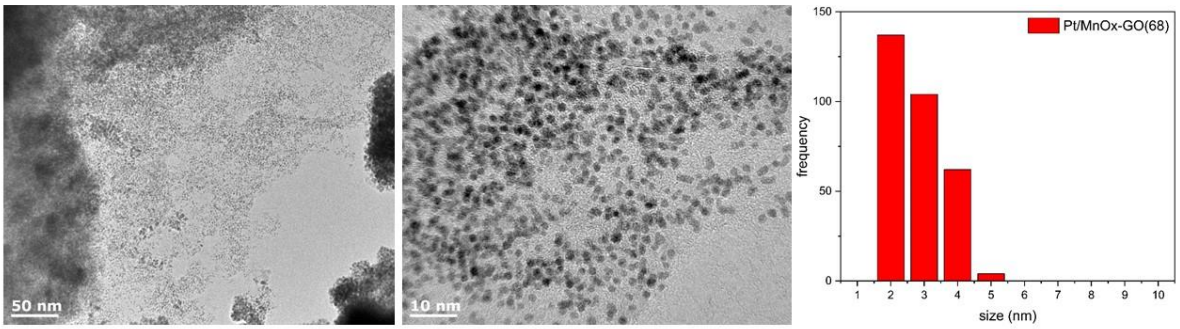

Figure 6.12 HR-TEM images of Pt/MnO_x-GO(68) and the corresponding particle size

The HR-TEM images of Pt/MnO_x-GO(68) (Figure 6.12) show Pt particles dispersed across the MnO_x-GO sheet. There are areas of single layers of support, and areas of multiple support layers stacked on top of each other. The areas where the HAADF images show bright Pt areas show that they are formed of Pt particles that are distinct particles clustered together. There are some of these clusters of particles across the sheet, tending to be at edges or near folds or wrinkles of the MnO_x-GO sheets. Between these clusters of particles are uniformly dispersed particles that occupy both sides of the support sheet.

The particle sizes of Pt/MnO_x-GO(50), Pt/MnO_x-GO(61) and Pt/MnO_x-GO(68) are shown in Figure 6.13. The Pt particles of Pt/MnO_x-GO(68) were measured using a sample of 307 particles, giving an average size of 2.3 nm ± 0.7 nm, which is smaller than Pt/MnO_x-GO(50) at 3.7 nm, and Pt/MnO_x-GO(61) at 2.8 nm, indicating that the Pt deposition onto MnO_x-GO is affected by the MnO_x content. MnO_x-GO supports with more Mn content grow smaller Pt particles. This is clearer in Figure 6.13, where the particle size histograms are shown in comparison to each other.

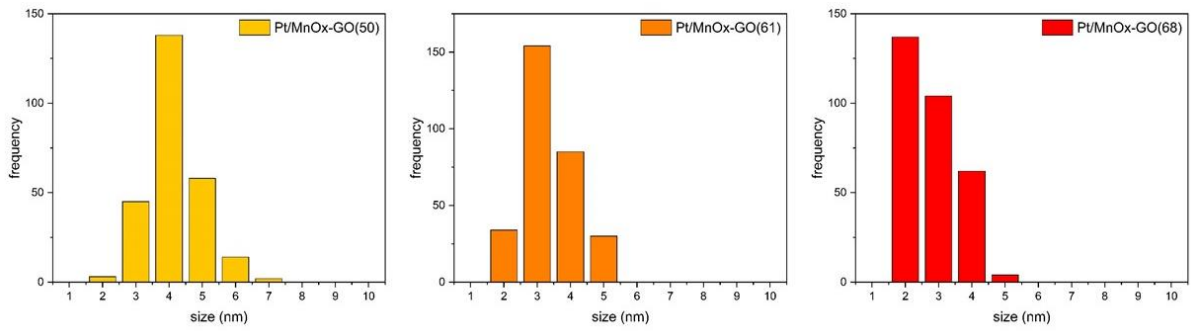

Figure 6.13 Particle sizes for Pt/MnO_x-GO(50), (61), and (68) measured by >200 particles

While the Pt particle sizes decreases with MnO_x content. The total Pt content (from ICP-MS) also decreases with MnO_x content. The Pt particles are known to grow on defect sites, and the nature and location of these defects also affects the growth of the particles, as shown by the TEM and EDX maps. It is expected that there are disperse defect sites on the GO, from reduced oxygen groups, and the MnO_x grows in flat layers, originating from these defects. For the MnO_x, it is expected that the defect sites are the locations of MnO_x step edges and crystal defects, which are closer together, meaning lots of smaller Pt particles start to grow on these, leading to the pattern seen in the TEM images, where there are more clusters of smaller particles on the higher MnO_x content supports, and less total Pt content evidenced by the ICP-MS results. The addition of MnO_x on the GO support appears to control the Pt particle size through the nature and locations of the defect sites which are available for Pt particles to grow onto.

6.4 Electrochemical performance of Pt/MnO_x-GO with varying MnO_x content

The Pt/MnO_x-GO samples were tested electrochemically to determine the effect of the varied Mn content on the durability of the Pt catalyst. Initially, the MOR was assessed by measuring the forwards : backwards peak current ratio (I_f:I_b). The MOR cyclic voltammograms are shown

in Figure 6.14. This may provide a good indication of the durability of the catalyst and tolerance to CO, however this is disputed[176–178], so the I_f:I_b ratio can only be used as an initial test to check the catalyst performs the methanol oxidation reaction, and to give an indication as to its durability.

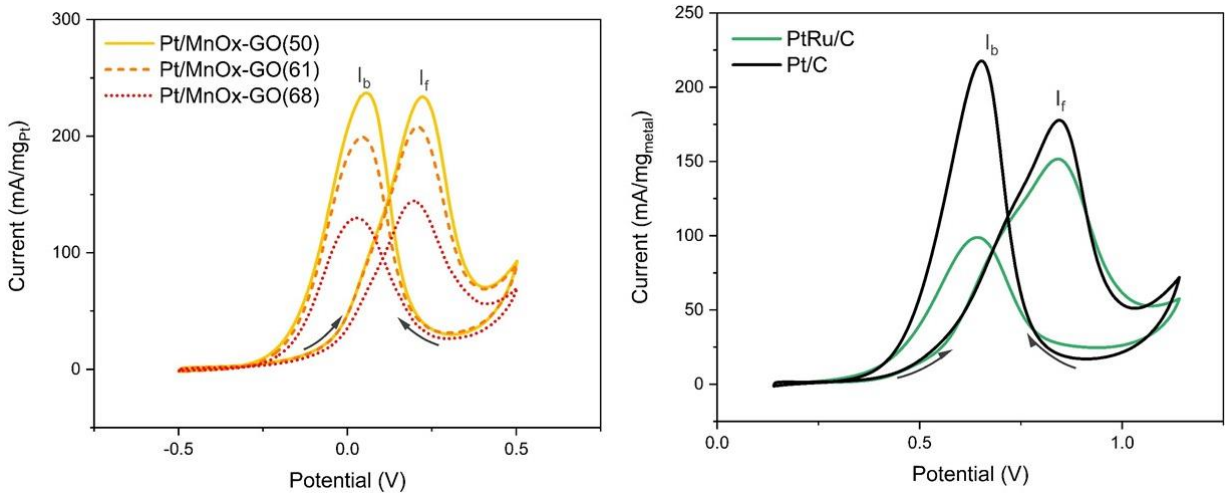

Figure 6.14 MOR plot showing I_f and I_b peaks for Pt/MnOx-GO(50), (61), and (68) and for comparison, Pt/C_{com} and PtRu/C_{com}.

The values for the I_f:I_b ratios can be found in Table 6.4, where they are shown to be PtRu/C_{com} > Pt/MnO_x-GO(68) > Pt/MnO_x-GO(61) > Pt/MnO_x-GO(50) > Pt/C_{com}, indicating that the PtRu/C_{com} catalyst shows the best promise for being a durable catalyst. However, for the Pt based catalysts, all of the Pt/MnO_x-GO catalysts have a higher I_f:I_b than Pt/C_{com}. The catalysts with higher MnO_x content in the support exhibit a higher I_f:I_b ratio, indicating that the MnO_x does have an effect on the catalysts and their durability.

In addition, the initial MOR plots show that there is a noticeable drop in current per mg platinum as the MnO_x content in the support is increased. This may be due to the high MnO_x content hindering performance, as MnO_x is not electrically conductive.

Table 6.4 I_f:I_b ratios and ECSA values for Pt/MnO_x-GO(50), (61) and (68), and for comparison, Pt/C_{com} and PtRu/C_{com}

	I_f:I_b	ECSA / $m^2.g_{Pt}^{-1}$
PtRu/C_{com}	1.54 ± 0.05	-
Pt/C_{com}	0.82 ± 0.05	88.7 ± 2.3
Pt/MnO_x-GO(50)	0.98 ± 0.05	4.4 ± 0.7
Pt/MnO_x-GO(61)	1.04 ± 0.05	5.3 ± 1.8
Pt/MnO_x-GO(68)	1.12 ± 0.05	3.5 ± 1.1

As shown in Table 6.4, the ECSA values for the commercial Pt/C_{com} Johnson Matthey HiSpec 3000 catalyst is far superior to the ECSAs of the Pt/MnO_x-GO catalysts, which is much smaller than previously reported for ECSAs of graphene supported catalysts[181]. This is believed to be due to the re-stacking effect of the GO sheet structure. In addition, the clusters of Pt particles that can be seen in the TEM may contribute to this low ECSA, as there will be a large mass of platinum that is on the inside of these clusters of particles that will not be fully accessible for the electrolyte, reducing the ECSA further.

Finally, accelerated degradation MOR tests were performed to determine the durability of the Pt catalysts on the MnO_x-GO supports with varied MnO_x content. These are shown in Figure 6.15. The current is normalised to mg of platinum on the electrode, so accounts for the slightly different Pt loading on the different supports.

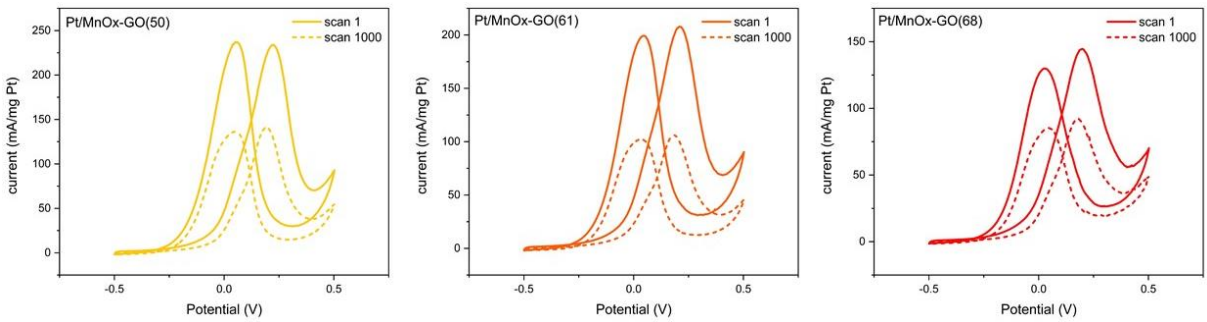

Figure 6.15 MOR accelerated degradation cycles for Pt/MnO_x-GO(50), (61), and (68).

The Pt/MnO_x-GO(68) catalyst exhibits the highest MOR durability over cycling, with only a 36% drop compared to the initial forwards peak current, whilst Pt/MnO_x-GO(50) shows a 40% drop , and Pt/MnO_x-GO(61) shows a 49% drop. The commercial PtRu/C_{com} and Pt/C_{com} exhibit a 49 % and 42% drop in initial forwards peak current after 1000 cycles respectively, meaning that the larger MnO_x content in the MnO_x-GO supports leads to a greater durability, even above the durability of the commercial Johnson Matthey HiSpec catalysts.

Again, there are a number of reasons why the addition of MnO_x may improve the durability[40]. The first being that the channels in the tunnel structures of manganese oxides allows for fast ion (and proton) transport, improving the adsorption and desorption of hydrogen, and helping the adsorbed CO to be oxidised. The second reason is that hydrogen and CO are believed to be able to migrate from the Pt to the MnO_x support, leaving the Pt active sites available. Finally, MnO_2 may generate hydroxyl species, which can then help to oxidise the CO intermediates on the Pt[179]. However, in addition to these suspected improvements from the MnO_x, it must be remembered that the structure of the Pt on the differing MnO_x supports is also different. It is widely documented that there exists an optimum platinum particle size, where the particles are not too large, to maximise activity per gram of platinum, and not too small so as the particles degrade quickly. Degradation of particles depends not only on size,

but also on inter-particle distance, and particle size distribution[47]. A platinum particle which is less than 2 nm in diameter will have >50% of its atoms not fully co-ordinated, and thus will be inherently unstable. Particles that are too close together will be attracted to each other through electrostatics, and so will tend to agglomerate or coalesce. A wide particle size distribution will waste precious mass of platinum on particles that are too large and so have a lower activity, or too small and are unstable. The tight distribution of particles just larger than 2 nm for the Pt/MnO_x-GO(68) sample suggests that these particles have been optimally grown, which when combined with the benefit from the MnO_x-GO support providing stability (as outlined in Chapter 5) leads this to be the most durable of the three variations of Pt/MnO_x-GO tested.

The increase in MnO_x however has a detrimental effect on the MOR forwards peak current, which drops by around 50 mV between Pt/MnO_x-GO(50) and (61) and around a further 50 mV between Pt/MnO_x-GO(61) and (68). This is down to the greater proportion of the poorly conducting MnO_x in the support, and in the case of the Pt/MnO_x-GO(68) is due to the greater proportion of oxygen functional groups which remain on the GO component of the support, again decreasing the electronic conductivity of the support, and decreasing the maximum current that can be obtained.

6.5 Conclusions

Varied amounts of MnO_x have been incorporated into the MnO_x-GO supports, using an increased $KMnO_4$ precursor. This led to the production of supports with 50%, 61% and 68% MnO_x: labelled MnO_x-GO(50), MnO_x-GO(61) and MnO_x-GO(68) respectively. These all formed

a MnO_2/Mn_2O_3 mixed oxide as shown by XPS, which also shows a significant potassium contamination. This potassium is believed to be trapped in the tunnel structures of the manganese oxides. XPS also shows that for the MnO_x-GO(68) sample, the carbon in the GO was not as significantly reduced, believed to be due to the large proportion of MnO_x in this sample.

On addition of platinum to all three supports, there is a further reduction in the carbon component of the support, however the MnO_x-GO(68) support did not reduce as much as the other two supports with lower MnO_x content. XRD, TEM, and EDX results show that the platinum is deposited as crystalline nanoparticles, but that the deposition is affected by the MnO_x content in the support. An increase in MnO_x leads to a decrease in platinum particle size and a narrower size distribution.

Two out of the three Pt/MnO_x-GO catalysts exhibited an increase in MOR cycling durability when compared to Pt/C_{com} and PtRu/C_{com} commercial catalysts, with the Pt/MnO_x-GO(50) showing a drop of 40% and Pt/MnO_x-GO(68) showing the highest durability with only a 36% drop in MOR performance after 1000 cycles. This is in comparison to a 42% drop for PtRu/C_{com} and 49% for Pt/C_{com}. However as was the case in Chapter 5, the Pt/MnO_x-GO catalysts suffer from a re-stacking effect of the sheet structure, which leads to poor ECSA values, inhibiting the attractiveness of this support to be used in a fuel cell.

Further work into improving the 3D structure of the catalyst support, preventing re-stacking of the graphene oxide sheets will be undertaken.

CHAPTER 7 Using manganese oxide to improve the durability of platinum catalysts on carbon black supports

Since the MnO_x-GO offers enhanced durability, but poor ECSA performance due to re-stacking of the graphene sheets, an alternative 3-D carbon was selected to be used in an alternative manganese oxide - carbon hybrid support. The aim being to provide the enhanced methanol oxidation durability from the manganese oxide, combined with carbon for electrical conductivity. In this instance a carbon which is 3-D was selected as it would not be affected by the re-stacking issues on drying like the graphene oxide was. Vulcan XC-72 carbon black was selected as it is a 3D structured conductive carbon and is a common commercial carbon catalyst support used in fuel cells.

7.1 Growth of manganese oxide on carbon black (MnO_x-CB)

Manganese oxide was added to carbon black in a similar synthesis route to the MnO_x-GO described in Chapter 5 and Chapter 6. 0.3g $KMnO_4$ was added to 50 mL deionised water and stirred. Meanwhile 0.1g Vulcan XC72 carbon black was added to 50mL deionised water and sonicated in a sonic bath for 30 minutes to ensure it was dispersed evenly. After, the $KMnO_4$ solution was added to the carbon black solution and mixed thoroughly by stirring for 15 minutes followed by 15 minutes of sonication. The mixture was then microwaved at 700 W for 4 minutes. After cooling, the mixture was washed in water and centrifuged (20,000 rpm, 21°C, 30 minutes) at least 3 times, until the supernatant was clear. The MnO_x-CB product was finally oven - dried at 60°C.

This MnO_x-CB support was first characterised by TGA and ICP-MS to determine the MnO_x loading.

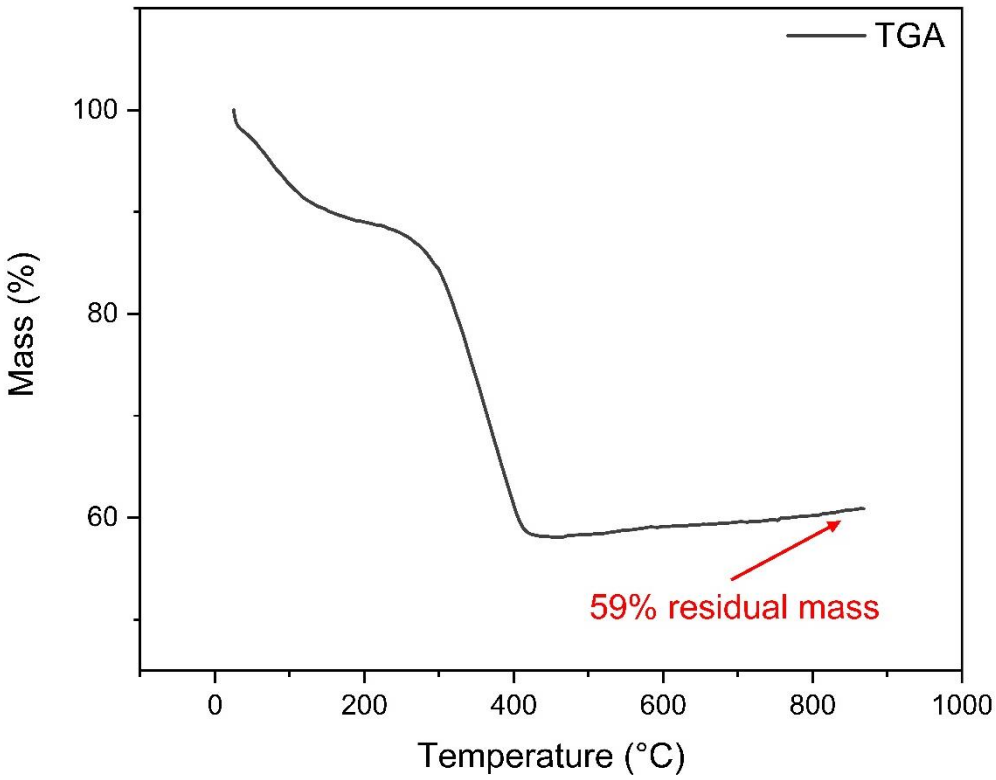

Figure 7.1 TGA curve for MnO_x-CB showing mass loss at different temperatures

The TGA curve for MnO_x-CB (Figure 7.1) has a slightly different shape to the GO shown in previous chapters. This is because the XC72 has a much lower oxygen content. Therefore, the only steps which are visible are the water loss step, around 100°C, and the burning of the carbon at 400°C. The carbon component burns at 400°C rather than the typical 600°C because of the metal content in the sample, which catalyses the carbon oxidation. The residual mass of 59% is assigned to MnO_x, as all of the carbon will have burned off at 900°C.

Figure 7.2 shows the XPS of the MnO_x-CB, which includes the oxidation state of the manganese, and any bonds present in the oxygen and carbon.

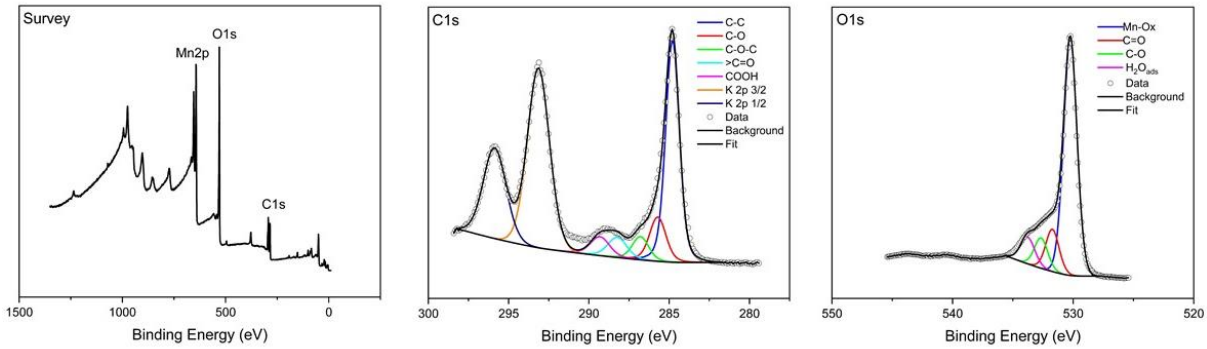

Figure 7.2 XPS survey, C1s and O1s spectra for MnO_x-CB

From the survey spectra it is evident that only Mn, C, O and K are present in the support, and no other significant contaminants are present. The large intensity of the Mn2p peak indicates that a substantial amount of Mn has been added to the carbon black support.

The C1s spectrum shows a noticeable contribution from the K2p peaks around 294 eV and 296 eV. This is believed to be similar to the MnO_x-GO supports, whereby the potassium ions get trapped into the tunnel structures of the MnO_x, preventing them from being successfully washed out. The shape of the C1s peak differs from the C1s peaks seen in previous chapters for graphene based materials. The C-C component for the C1s peak is very strong, with only small contributions from C-O, C-O-C, >C=O and COOH peaks, as the carbon black contains few oxygen groups in comparison to the GO used previously.

The O1s peak also reflects the low oxygen content, with the majority of the peak being attributed to the Mn-O_x component, with only small contributions from the C-O and C=O peaks. In addition, there is a smaller water peak seen, which is due to the nature of the carbon black, which is much less hydrophilic than the GO in previous chapters.

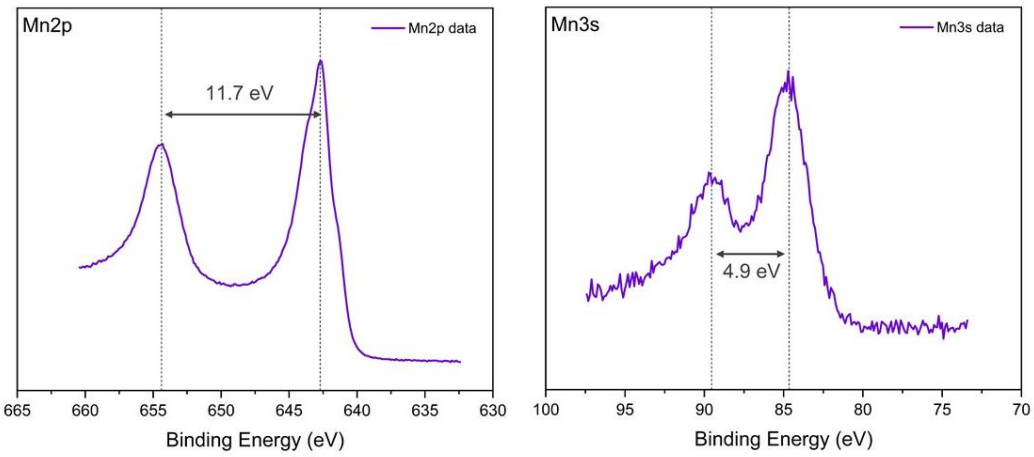

Figure 7.3 XPS Mn2p and Mn3s spectra for MnO_x-CB

The XPS Mn2p peak and Mn3s peaks are shown in Figure 7.3. The Mn2p peak shape and separation suggests a MnO_2/Mn_2O_3 mixed oxide, similar to the MnO_x deposited on GO. The peak separation of 4.9 eV for the Mn3s peak is slightly larger than the 4.7 eV for MnO_2, but much smaller than the 5.3 eV for Mn_2O_3, suggesting a mixed oxide, but predominantly MnO_2.

Table 7.1 Mn present in MnO_x-CB, values from ICP-MS

	Mn / %
MnO_x-CB	22.8 ± 0.5

ICP-MS (results shown in Table 7.1) shows a 22% Mn content in the MnO_x-CB sample, which matches with the 59% MnO_x content obtained from TGA, when accounting for the oxygen content of the MnO_x.

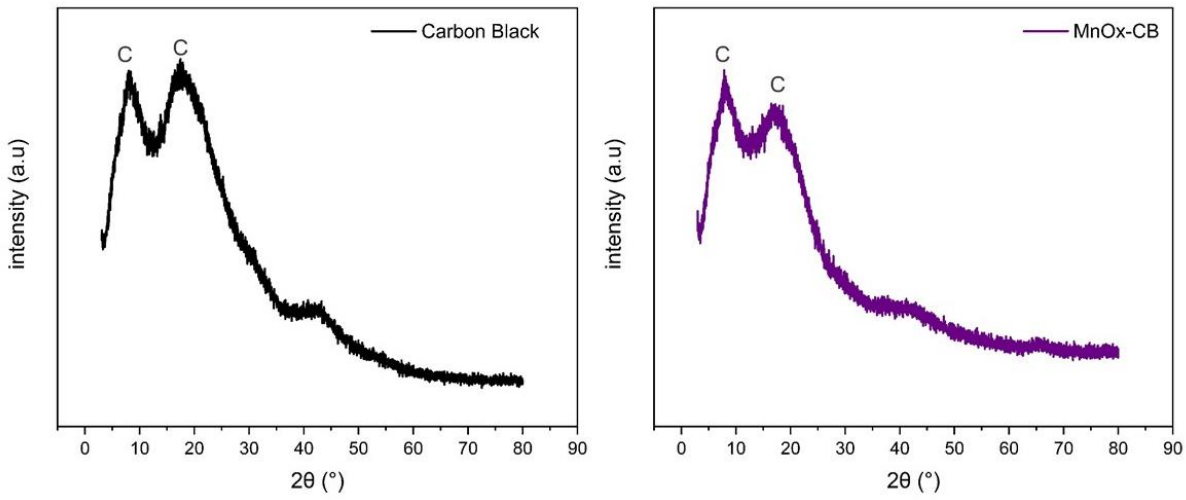

Figure 7.4 XRD spectra for carbon black (CB) and MnO_x-CB

XRD results (Figure 7.4) show two carbon peaks at 8° and 18°. There is no noticeable difference between the CB and MnO_x-CB, indicating that the crystallinity of the carbon support is unaffected by the deposition of MnO_x. There are no visible Mn XRD peaks, despite its presence being confirmed by ICP-MS and XPS. This may be due to a similar effect observed in earlier chapters, whereby the MnO_x deposits are so small and thin that they do not diffract sufficiently to cause a visible XRD peak.

Finally, TEM images show the carbon black support in Figure 7.5 which is a smooth sphere before addition of the MnO_x.

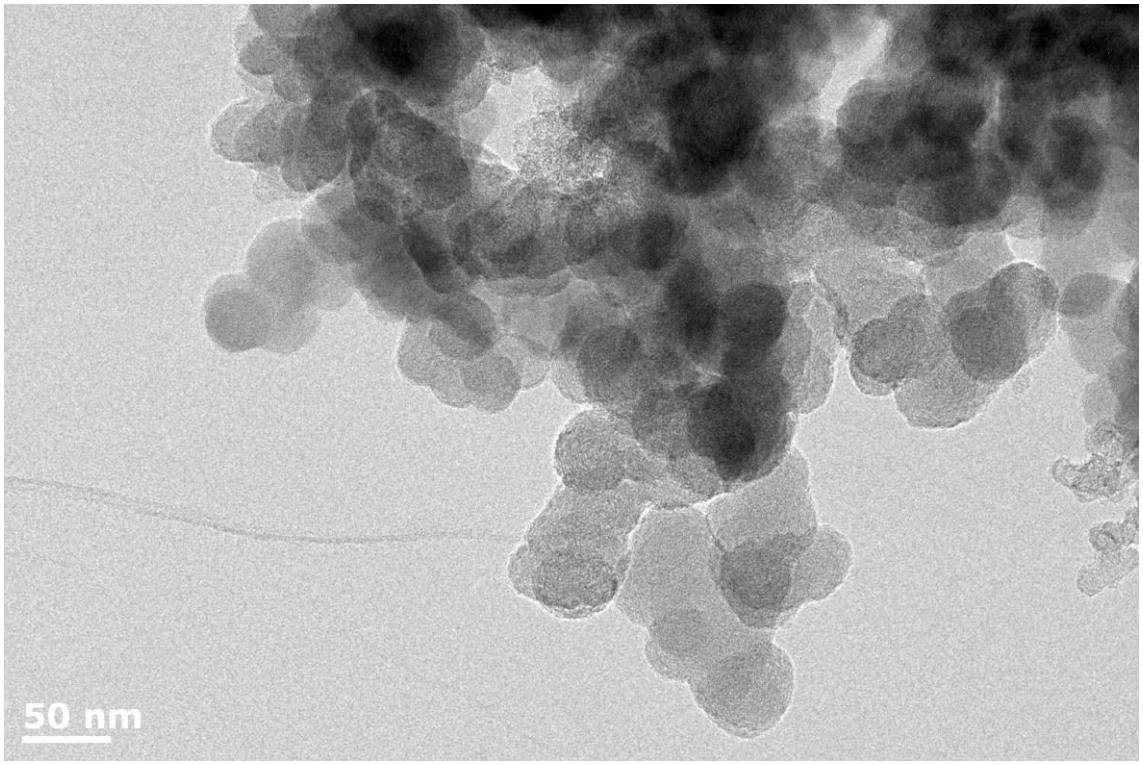

Figure 7.5 TEM image of carbon black, before any processing or deposition.

This morphology is to be expected for the XC72 Vulcan carbon used. The carbon spheres are 15 to 60 nm in diameter and form a 3D network with pores. These pores allow for good reactant flow when the carbon black is used as a catalyst support, while the 3D network allows for good electrical conductivity.

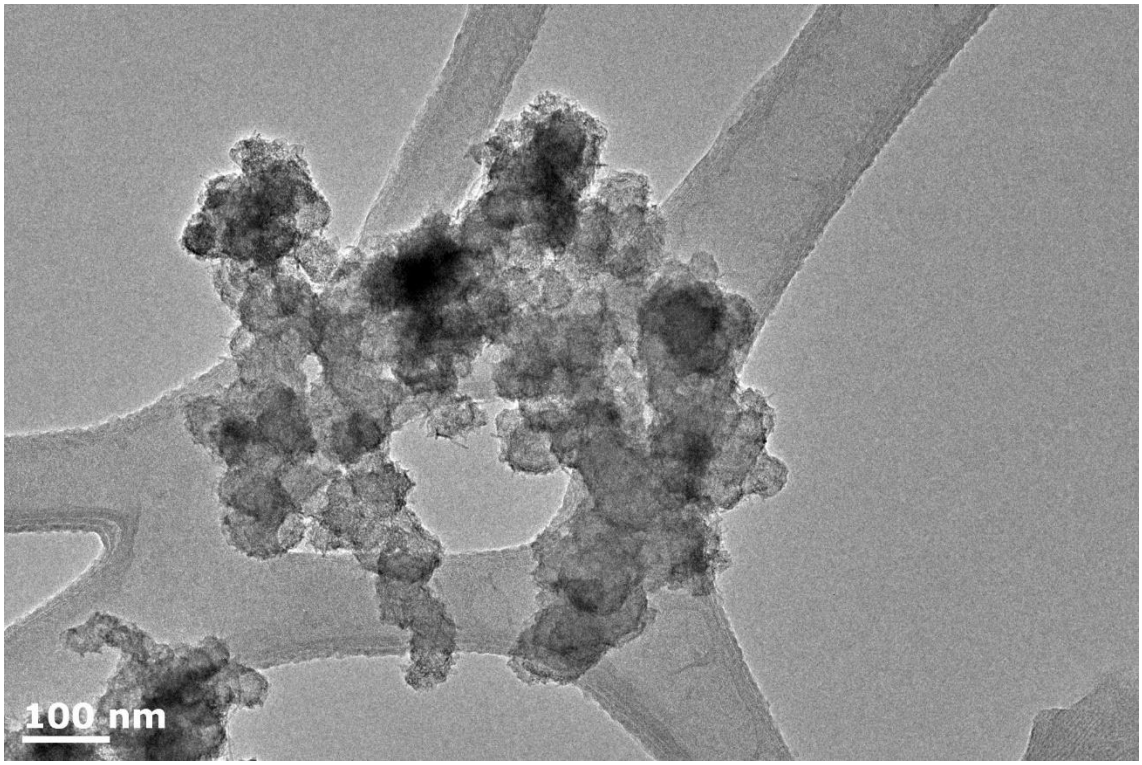

Figure 7.6 TEM image of MnO_x-CB

Figure 7.6 shows the MnO_x-CB, with the lacey carbon TEM grid visible in the background. It can be seen that on addition of the MnO_x, the carbon spheres appear rough, as if the MnO_x has deposited differently to the smooth patches of MnO_x seen on the GO in previous chapters.

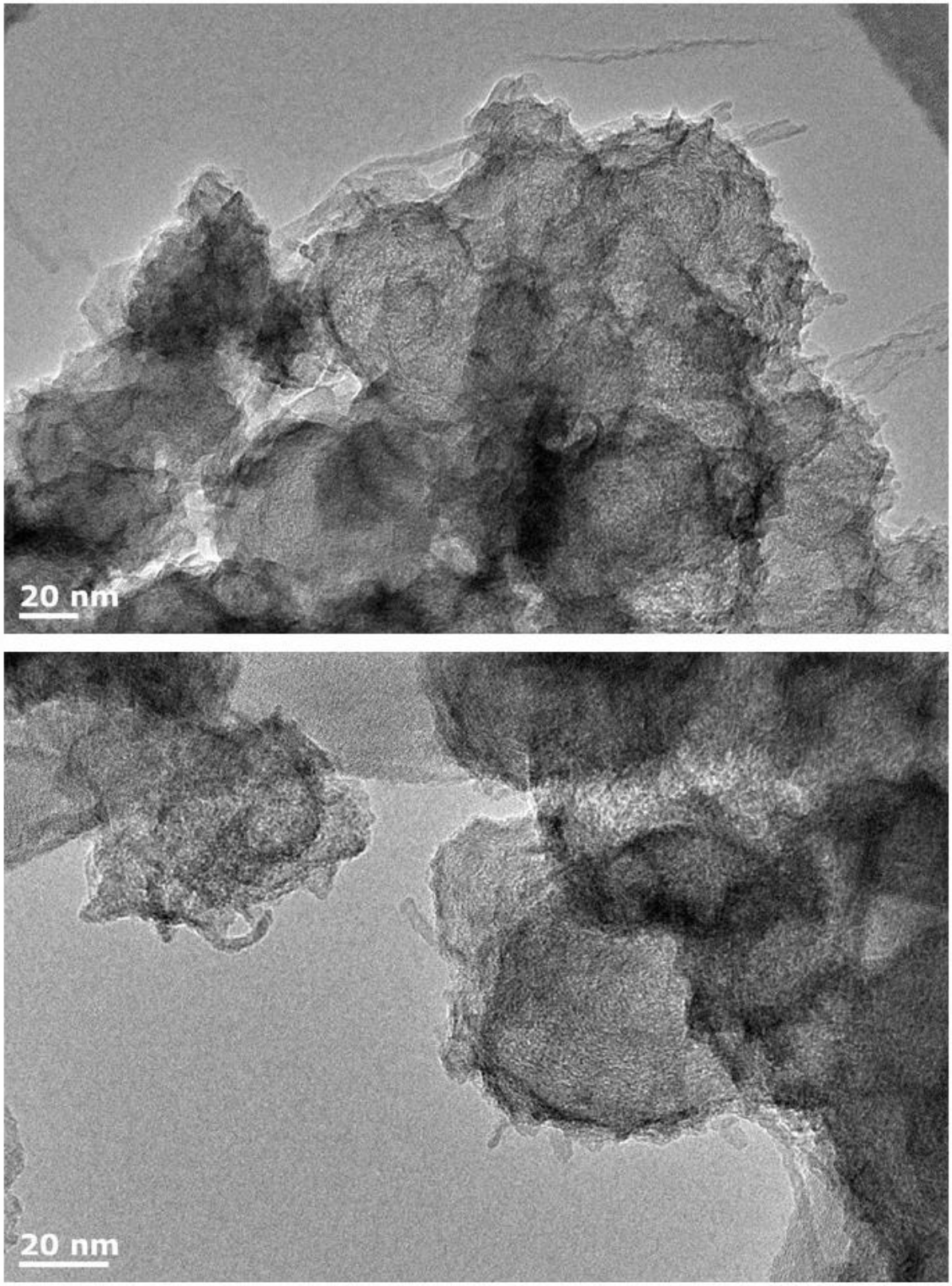

Figure 7.7 TEM image showing the MnO_x nanorod growth of MnO_x-CB

On closer inspection, in Figure 7.7, the MnO_x appears to be growing in small nanorods out of the carbon black. The growth of the MnO_x is known to nucleate on defect sites. Carbon black, being a more amorphous material and having few oxygen functional groups, exhibits fewer defect sites than the GO had on its surface for the MnO_x to grow on. Therefore, the MnO_x nucleates on these few defect locations and preferentially grows on top of itself because there are no other defect sites for the MnO_x to nucleate on, resulting in the nanorod structure.

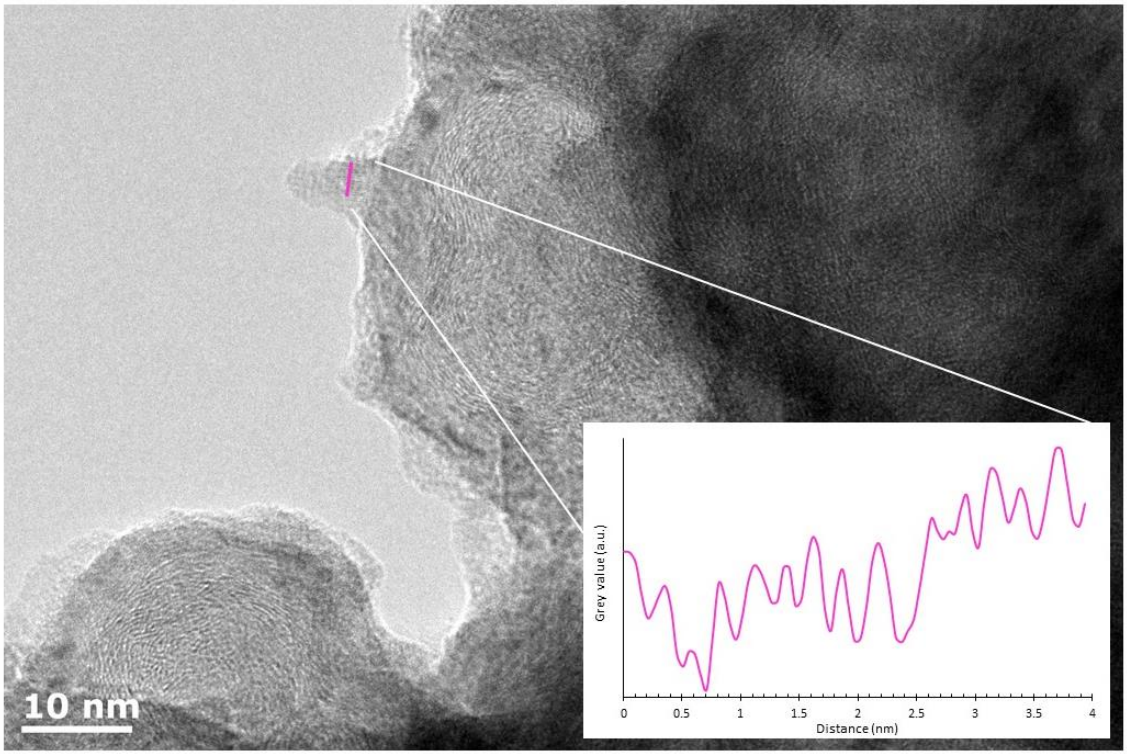

Figure 7.8 HR-TEM image showing the crystallinity of the MnO_x nanorods on MnO_x-CB. Inset: line profile of a MnOx nanorod showing the interlayer spacing.

The MnO_x nanorods are crystalline in nature, as can be seen from the line profile of the nanorod measurement in Figure 7.8, which gives an interlayer spacing of 0.26 nm ± 0.02 nm, consistent with the (031) plane of MnO_2[174].

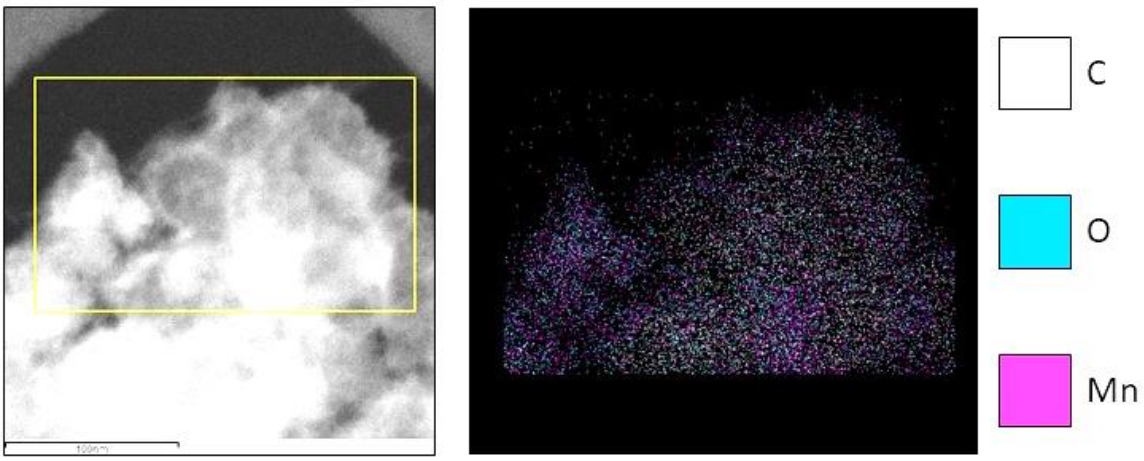

Figure 7.9 EDX map of MnO_x-CB support, showing areas of C, O, and Mn. The yellow box on the TEM image denotes the EDX map area.

The EDX map in Figure 7.9 of the MnO_x-CB support shows that the MnO_x is deposited across the entire surface of the carbon black. The intensity of oxygen and manganese coincide with each other, meaning that the majority of the oxygen in the MnO_x-CB support arises due to the manganese oxide component, rather than the carbon black. This is expected and reflects the XPS results.

7.2 Platinum on carbon black and MnO_x-CB

Platinum was subsequently grown on top of this MnO_x-CB support through a second microwave deposition method. In addition to Pt/MnO_x-CB, a platinum on carbon black (Pt/CB) was produced, following the same Pt deposition synthesis route. This was to enable comparison and show any differences between the commercial platinum deposited on Johnson Matthey Pt/CB_{com} and my Pt/MnO_x-CB.

Platinum was deposited via the same route as was used to prepare Pt/MnO_x-CB. First, 1 mL of 0.1 M K_2PtCl_6 was added to a homogeneous dispersion of 40mg catalyst support and 20mL

ethylene glycol. This was then mixed for 60 minutes using sonication, and then microwaved for 1 minute at 700 W to deposit platinum particles. The product was cooled, washed using acetone and centrifugation and then dried at 60°C. See chapter 3.2 for more detail.

The Pt/CB and Pt/MnO_x-CB were initially characterised by ICP-MS to determine the platinum and manganese loadings.

Table 7.2 Pt and Mn present in Pt/CB and Pt/MnO_x-CB, values from ICP-MS

	Mn / %	**Pt / %**
Pt/CB	-	25.7 ± 0.5
Pt/MnO_x-CB	4.6 ± 0.5	28.6 ± 0.5

The ICP-MS results (Table 7.2) show that the amount of platinum deposited on the CB and MnO_x-CB is similar, though there is slightly more platinum deposited on the MnO_x-CB. This may be due to the influence of defect sites, of which there will be many more on the MnO_x-CB support compared to the CB support, meaning that platinum can nucleate and grow more easily on the MnO_x-CB. ICP-MS shows that there is 4.6% manganese overall in the Pt/MnO_x-CB catalyst/support system.

Next, XRD was used to determine the crystallinity of the deposited platinum. The XRD spectra for Pt/CB and Pt/MnO_x-CB are shown in Figure 7.10.

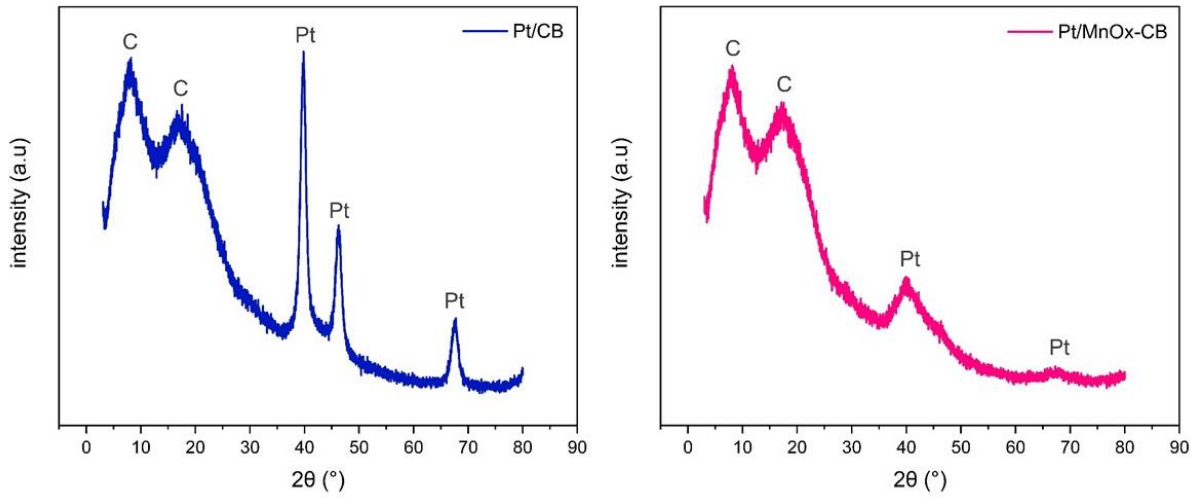

Figure 7.10 XRD spectra for Pt/CB and Pt/MnO_x-CB

The same carbon peaks seen in the supports are seen in both the Pt/CB and Pt/MnO_x-CB samples, which indicates that the deposition of the platinum does not significantly affect the structural properties of the carbon black support. Very clear platinum peaks at are seen on the Pt/CB at 40°, 46°, and 68° (JCPDS PDF 00-001-1194), indicating that the deposited nanoparticles are crystalline. For Pt/MnO_x-CB, the platinum peaks at 40° and 68° (JCPDS PDF 00-001-1194), are still visible but are much less intense than for Pt/CB and appear to be broader. The Pt peak at 46° is not distinguishable from the background noise for the Pt/MnO_x-CB. These low intensity peaks indicate that the particles are less crystalline than the particles on the Pt/CB, and the broader peaks point towards smaller particles, as smaller particles produce wider diffraction peaks, as described by the Scherrer equation[159,182]:

$$\tau = \frac{K\lambda}{\beta cos\theta} \qquad (7.1)$$

where τ is the average crystallite size, K is a dimensionless shape factor (usually 0.9), λ is the wavelength of the X-ray, β is the full width at half the maximum (FWHM) of the X-ray peak, and θ is the Bragg angle.

Next, XPS was used to determine the oxidation states of the deposited platinum, and to investigate the effect that the platinum deposition process has on the carbon black and MnO_x-CB supports. Pt/CB XPS survey spectra, C1s, O1s and Pt4f are shown in Figure 7.11.

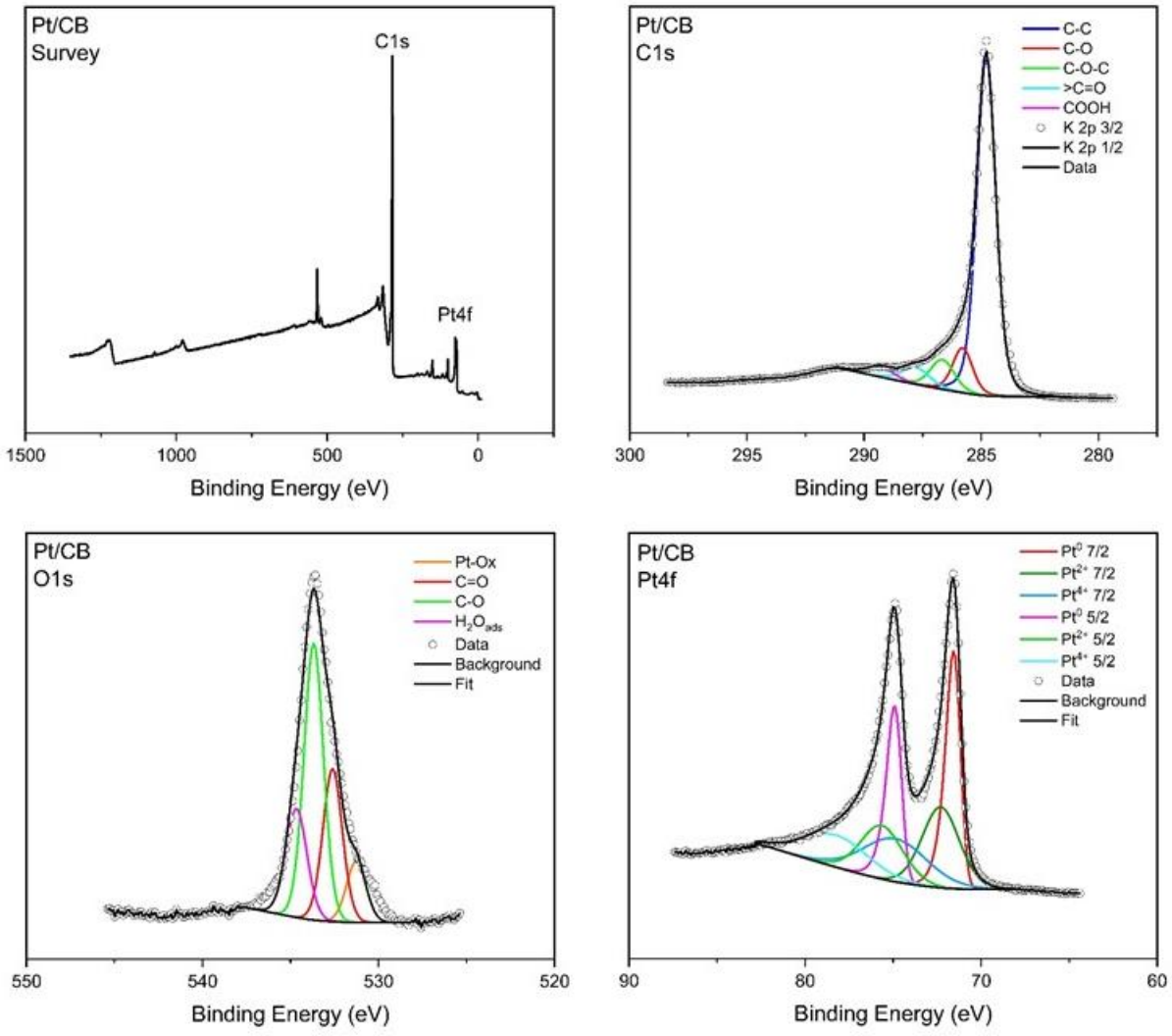

Figure 7.11 XPS survey, C1s, O1s and Pt4f spectra for Pt/CB

The Pt/CB XPS survey spectrum shows that only carbon, oxygen and platinum are present in the Pt/CB, and there are no major contaminants remaining after the synthesis procedure.

The C1s peak shows a very strong C-C component, and only very small carbon – oxygen bonds, because the XC-72 carbon black used has very few oxygen groups. The deposition of the platinum particles does not affect the C1s peak. The Pt4f shows a strong Pt^0 peak, indicating that there is a large proportion of the deposited platinum nanoparticles are pure metal, making them good candidate catalysts.

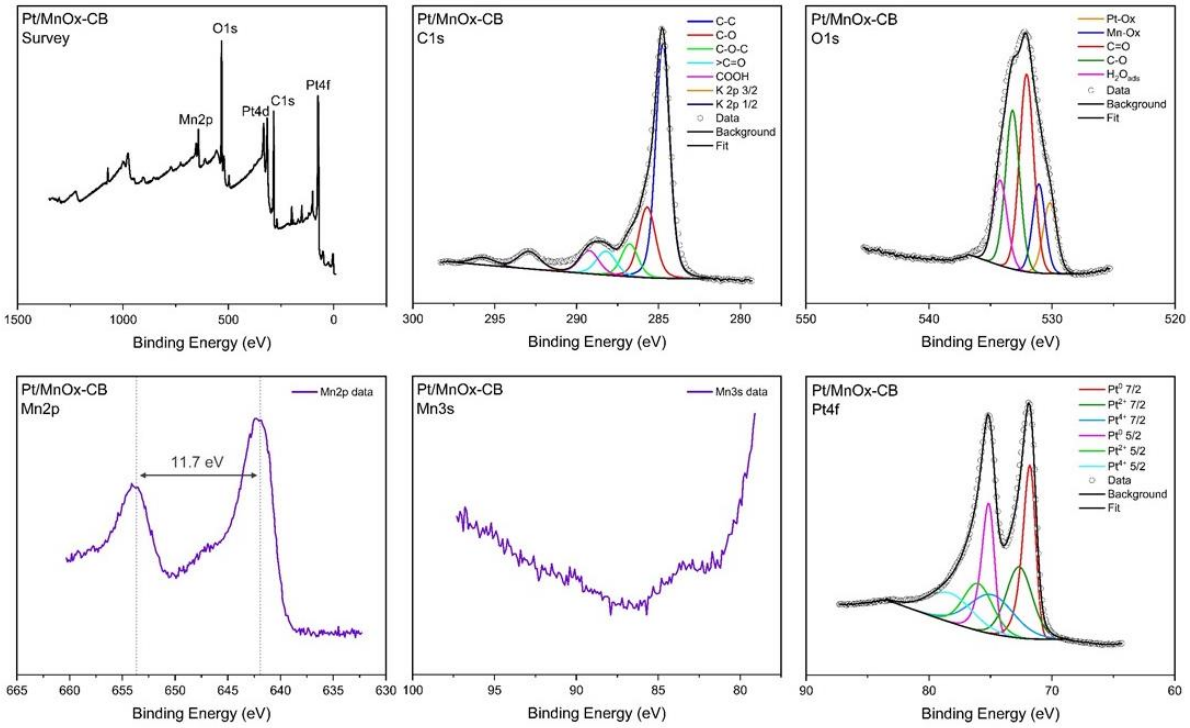

Figure 7.12 XPS survey, C1s, O1s, Mn2p, Mn3s, and Pt4f spectra for Pt/MnO_x-CB

The Pt/MnO_x-CB is a more complex system owing to the MnO_x content, however, shows a similar story to the Pt/CB XPS spectra. These Pt/MnO_x-CB XPS spectra are shown in Figure 7.12. Only carbon, oxygen, platinum and manganese are present in the survey spectra, indicating that there are no significant contaminants present in this Pt/MnO_x-CB.

The C1s spectra shows a strong carbon peak, similar to the Pt/CB, however in this instance, there is a slight increase of the C-O component. This arises due to the MnO_x, and the bond between the oxygen from the MnO_x and the carbon in the carbon black. There is also a small amount of potassium visible as the K2p peaks in the C1s spectrum window. This arises from the MnO_x deposition, which left a large K2p peak visible in the MnO_x-CB sample. The K2p peak in the Pt/MnO_x-CB is dramatically lower than for the MnO_x-CB, indicating that the process of depositing the platinum and the washing helps to remove the potassium that can easily become trapped in the tunnel structures formed by manganese oxides. This removal of the potassium during the platinum deposition step was also seen when using the graphene oxide based supports in previous chapters.

The Pt4f spectra for the Pt/MnO_x-CB is very similar to the Pt4f spectra for Pt/CB, showing a large Pt^0 component, along with some Pt^{2+} and Pt^{4+} components. The similarity indicates that the MnO_x-CB and CB behave similarly during the Pt deposition step, and the difference in MnO_x-CB and CB supports does not have a major effect in the electronic structure of the deposited platinum.

The Mn2p peak for the Pt/MnO_x-CB has a peak separation of 11.7 eV, which is attributed to MnO_2, however the peak shape also shows a satellite feature, commonly found in MnO, suggesting that the MnO_x is in a mixed oxide state. Further clarification on the MnO_x oxidation state could not be obtained from the Mn3s spectrum, as the peaks were not distinguishable from the background noise. This may be because of the interference from the Pt4f peak, which sits very close to the Mn3s peak.

TEM images were obtained of both the Pt/CB and Pt/MnO_x-CB samples to determine their physical structure. The TEM images (Figure 7.14 and Figure 7.15) show that both the Pt/CB and Pt/MnO_x-CB exhibit the same platinum particle clustering effect seen in previous chapters. This may be due to growth effects, as platinum particles nucleate on defect sites, which there may be more of in certain areas. This effect may be minimised if a different platinum particle growth method is used, as it is the direct growth method that utilises these defect sites to initiate platinum particle growth. If the particles were to be prepared separately and then deposited onto the support, this may prevent this clustering phenomena. However, this would not come without some drawbacks in the performance of the final material, for example the particle-support interaction would not be as strong, potentially decreasing the durability of the catalyst/support system.

EDX maps of the Pt/MnO_x-CB (Figure 7.13) show that the Pt and Mn are distributed across the carbon black support. The Pt and Mn intensities appear to be higher in the same locations on the material, however on closer inspection, this stronger intensity looks to be due to a thicker part of the Pt/MnO_x-CB material.

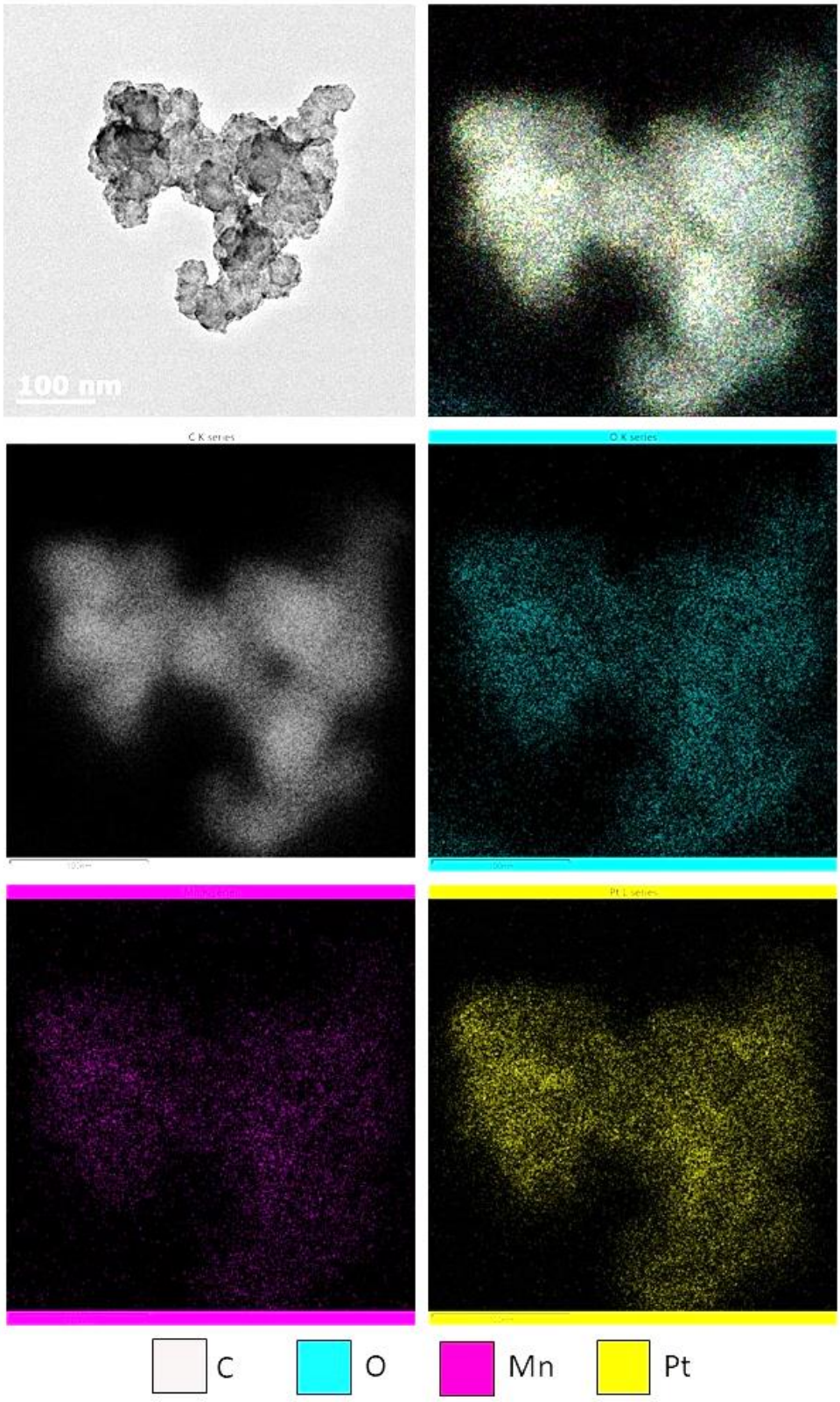

Figure 7.13 EDX map of MnO_x-CB support, showing areas of C, O, Mn and Pt. Top 2 images: TEM image & EDX composite map. Bottom 4 images: Individual element maps.

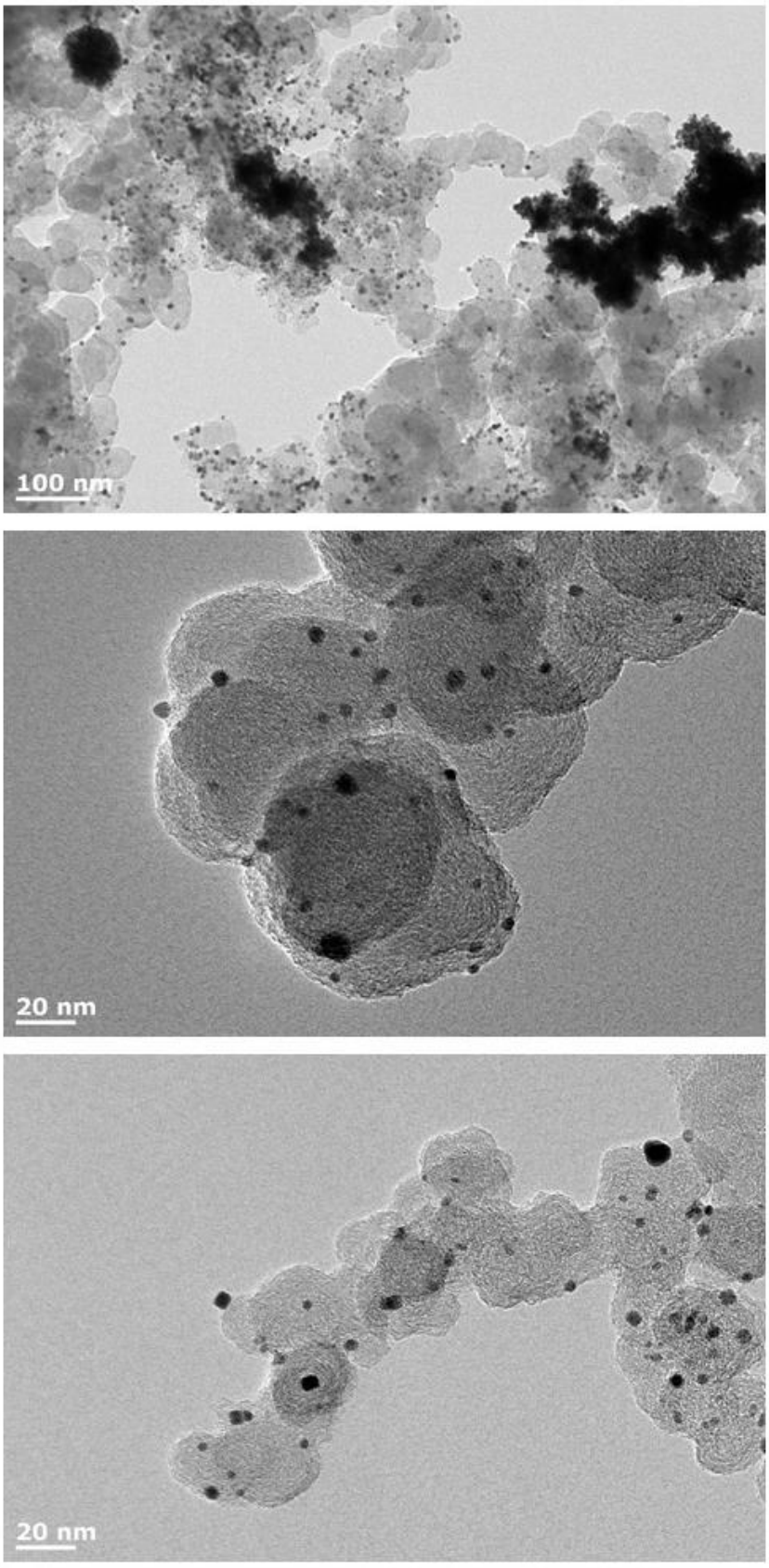

Figure 7.14 TEM images of Pt/CB

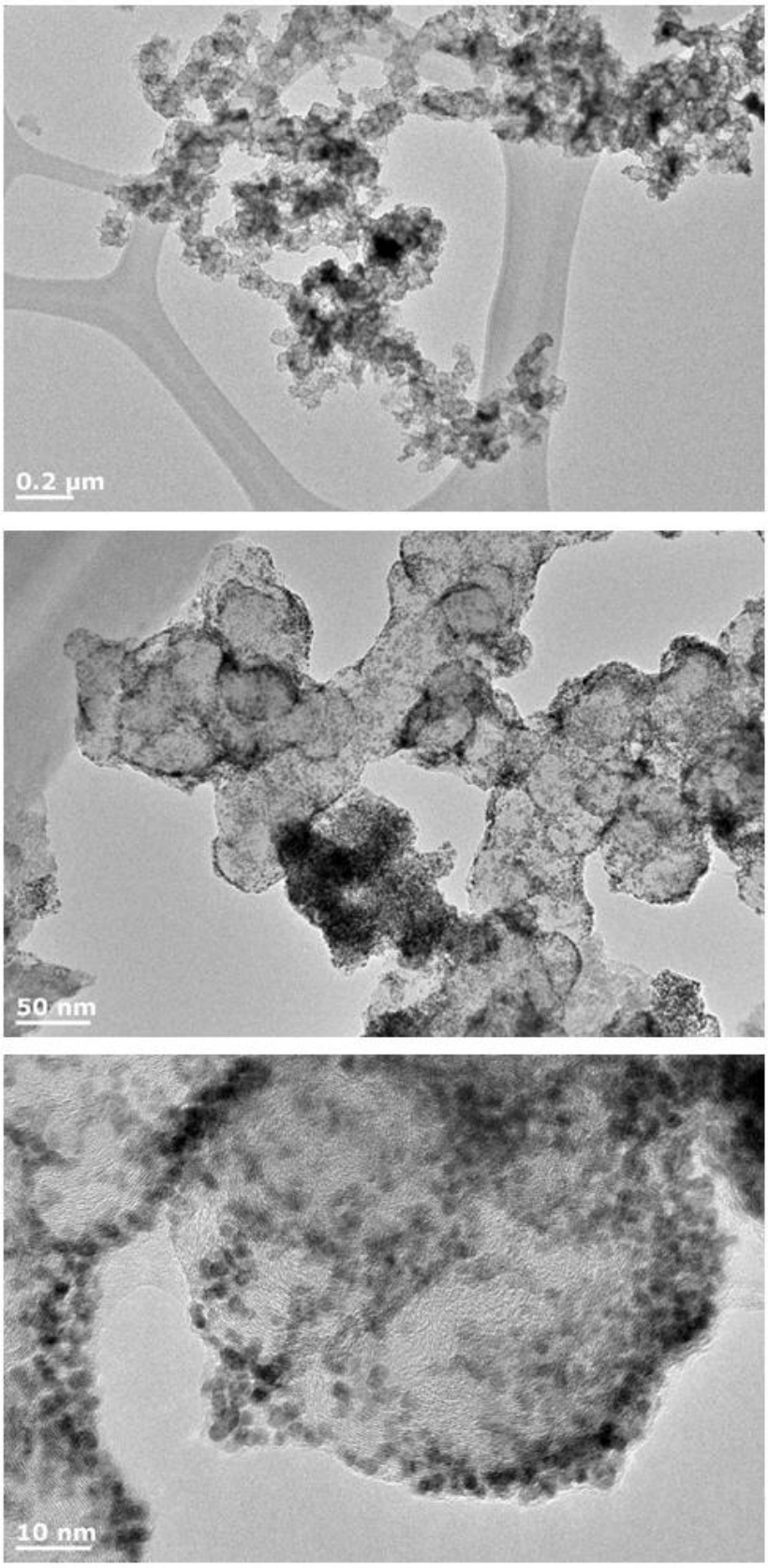

Figure 7.15 TEM images of Pt/MnO_x-CB

The TEM images of the Pt/CB (Figure 7.14) shows that the structure of the carbon support remains the same, and the spherical carbon black support can be seen throughout the images. Aside from a few clusters, the deposited platinum particles are evenly dispersed across the carbon black and have a large inter-particle distance. The particles are deposited on the outer edges of the carbon black spheres. The size of the platinum particles, measured from 229 particles, was 3.42 nm ± 2.27 nm. This particle size is larger than for the platinum deposited on graphene in earlier sections, showing that the choice of carbon support is one critical factor in the development of the catalyst/support system – particularly when a direct growth mechanism is used. This size effect is believed to be due to the relative lack of defect sites on the carbon black compared to graphene oxide, which are required for the platinum to nucleate on. Once the few defect sites have been covered by platinum particles, the only place for further platinum deposition is on the existing Pt particles, causing them to grow larger.

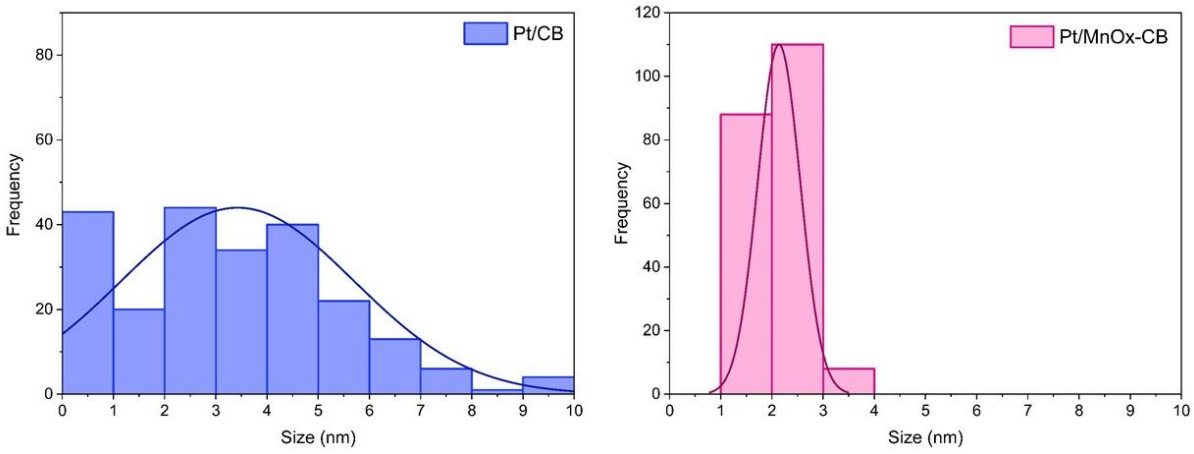

Figure 7.16 Particle size histograms for Pt/CB and Pt/MnO_x-CB

For the Pt/MnO_x-CB catalyst/support system (Figure 7.15), the MnO_x-CB roughness as seen in the bare support characterisations in section 7.1 is still visible in the TEM images, which

indicates that the Pt deposition does not drastically alter the structure of the MnOx in the support. There is less clustering of platinum particles in the Pt/MnO_x-CB compared to the Pt/CB, and even in locations where there is a high density of particles, they appear to be smaller clusters than for the Pt/CB. Again, the platinum particles are deposited on the surfaces of the MnO_x-CB support. The Pt particles in the Pt/MnO_x-CB are much smaller, and as such have a smaller inter-particle distance, owing to their small size. The size of the platinum particles was measured from 206 particles and was 2.13 nm ± 0.41 nm. In addition to being much smaller, the standard deviation on the mean is also much smaller, showing that the distribution is narrower, and indicating that the growth and deposition of platinum particles is more controlled on the MnO_x-CB support. This difference in size and inter-particle distance is attributed to the growth mechanism relying on defect sites on which the platinum nanoparticles nucleate. The surface of the MnO_x-CB is visibly rougher, owing to the MnO_x which has many edges, steps and other crystal defects, so the Pt particles grow across the whole surface, resulting in Pt particles that are smaller on the MnO_x-CB support compared to the CB. Therefore, addition of MnO_x onto a carbon support can control the size and size distribution of deposited Pt particles when they are grown in a direct growth method.

7.3 Electrochemical Performance of Pt/MnO_x-CB

The Pt/CB and Pt/MnO_x-CB were first assessed for their methanol oxidation reaction activity. They were tested against Pt/Cc_{om} and PtRu/C_{com}, the commercial standards.

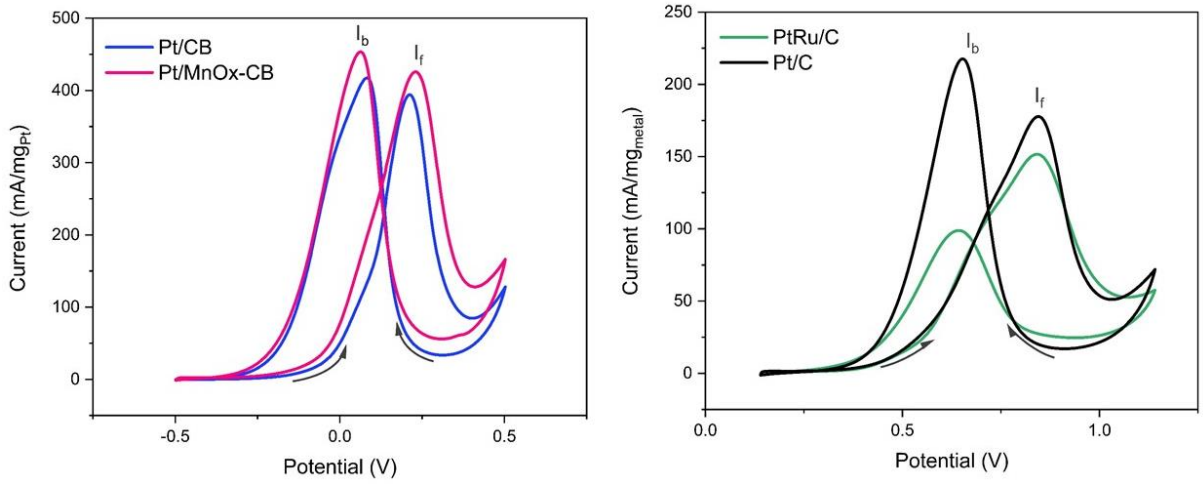

Figure 7.17 Initial MOR testing for Pt/CB and Pt/MnO_x-CB and their comparicon to Pt/C_{com} and PtRu/C_{com}.

The Initial MOR cycles seen in Figure 7.17 shows that the performance of both the Pt/CB and Pt/MnO_x-CB is much greater (in terms of forwards peak current per milligram of catalyst) than the commercial catalysts. The Pt/CB and Pt/MnO_x-CB have a forwards peak current of 391 mA/mg_{Pt} and 426 mA/mg_{Pt} respectively, while the Pt/C_{com} and PtRu/C_{com} have forwards peak currents of 177 mA/mg_{Pt} and 152 mA/mg_{metal}. This indicates that the Pt/CB and Pt/MnO_x-CB show great promise for MOR catalysts, as they provide more current per mg of Pt metal used in the catalyst.

Despite its documented drawbacks[176–178], the forwards : backwards peak current (I_f:I_b)ratio was used to investigate the potential of the Pt/CB and Pt/MnO_x-CB to be a durable catalyst as an initial screening test.

Table 7.3 I_f:I_b ratios and ECSA values for Pt/CB and Pt/MnO_x-CB, and comparison to Pt/C_{com} and PtRu/C_{com}

	I_f:I_b	ECSA / m^2,g_{Pt}^{-1}
PtRu/C_{com}	1.54 ± 0.05	-
Pt/C_{com}	0.82 ± 0.05	88.7 ± 2.3
Pt/CB	0.93 ± 0.05	9.9 ± 3.2
Pt/MnO_x-CB	0.94 ± 0.05	14.0 ± 3.4

As can be seen in Table 7.3, the I_f:I_b ratio is higher in the case of Pt/CB and Pt/MnO_x-CB than for the commercial Pt/C_{com}. Meanwhile, the PtRu/C_{com} exhibits a much higher I_f:I_b ratio than any of the other catalysts in this instance, indicating its superior durability. The Pt/CB and Pt/MnO_x-CB may perform well as durable MOR catalysts, but since this I_f:I_b ratio measurement is not the most accurate for determining durability, accelerated cycling must be undertaken in order to determine how durable these candidate catalysts are.

The ECSA for Pt/CB and Pt/MnO_x-CB (Table 7.3) are higher than previously obtained when using a graphene based support, indicating that the choice of a 3D carbon support material such as carbon black has helped to overcome the re-stacking issue that was seen in previous chapters where graphene oxide was used. The ECSA however is still not as high as the commercial catalysts, indicating that there are some experimental parameters that are not fully optimised, perhaps the catalyst ink preparation and deposition needs optimisation or a further processing step is needed before these Pt/CB and Pt/MnO_x-CB particles are used in

an electrochemical environment. The ECSA for the Pt/MnO_x-CB is higher than for Pt/CB, which makes sense considering the platinum particle size and dispersion seen on the TEM images.

Accelerated cycling tests, which are shown in Figure 7.18, were undertaken for these Pt/CB and Pt/MnO_x-CB, however due to laboratory conditions during this period, no accurate temperature control could be maintained. For this reason, only 500 accelerated degradation cycles were undertaken, in contrast to the 1000 used previously. The temperature variation over 500 cycles was not significant, however greater temperature fluctuations occurred between 500 and 1000 cycles, causing inaccuracies in the measurements at these high numbers of cycles.

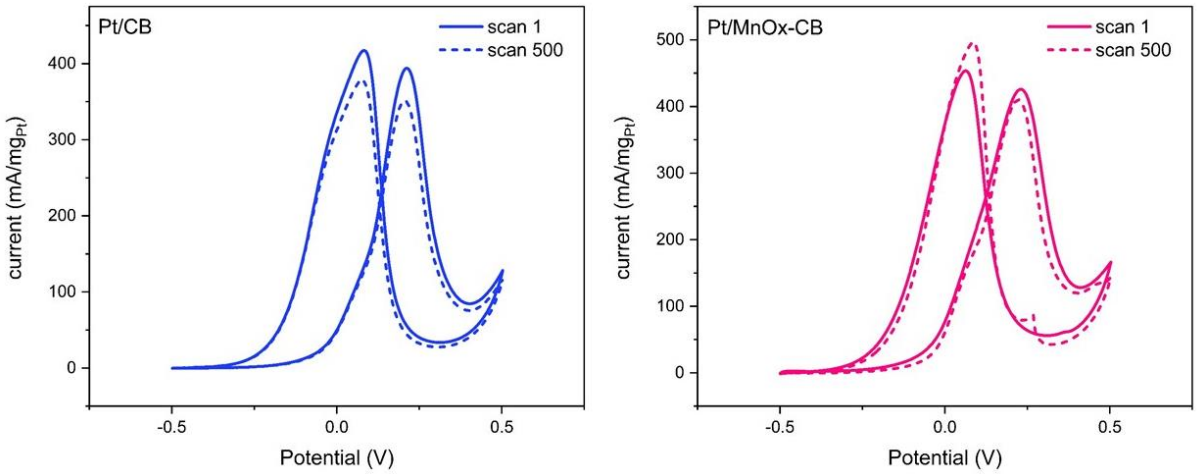

Figure 7.18 MOR accelerated degradation cycles for Pt/CB and Pt/MnO_x-CB.

After 500 degradation cycles at 50mV/s, the Pt/CB has started to degrade more rapidly than the Pt/MnO_x-CB, which exhibits very little drop in its performance. The forwards peak current for Pt/MnO_x-CB drops by only 4.7% after 500 cycles, compared to an 11% drop for Pt/CB. This indicates that by adding MnO_x to the support, it provides additional durability compared to using carbon black alone. This improvement in durability has been observed both in the case

of adding manganese oxide to graphene oxide, and to carbon black, suggesting that the addition of MnO_x to any carbon support should improve the durability of platinum catalysts applied to the MnO_x-carbon supports. This improved durability may arise due to the structural changes when MnOx is added to the support, where the MnOx provides a very rough surface[33] with many more defect sites than the carbon black alone, improving the CO to CO_2 conversion. Also, the tunnel structure of manganese oxide will provide fast ion transport, improving adsorption and desorption of hydrogen and CO[40]. In addition, hydroxyl species on the MnO_2 can help to oxidise the CO_{ads} on the platinum surface[179].

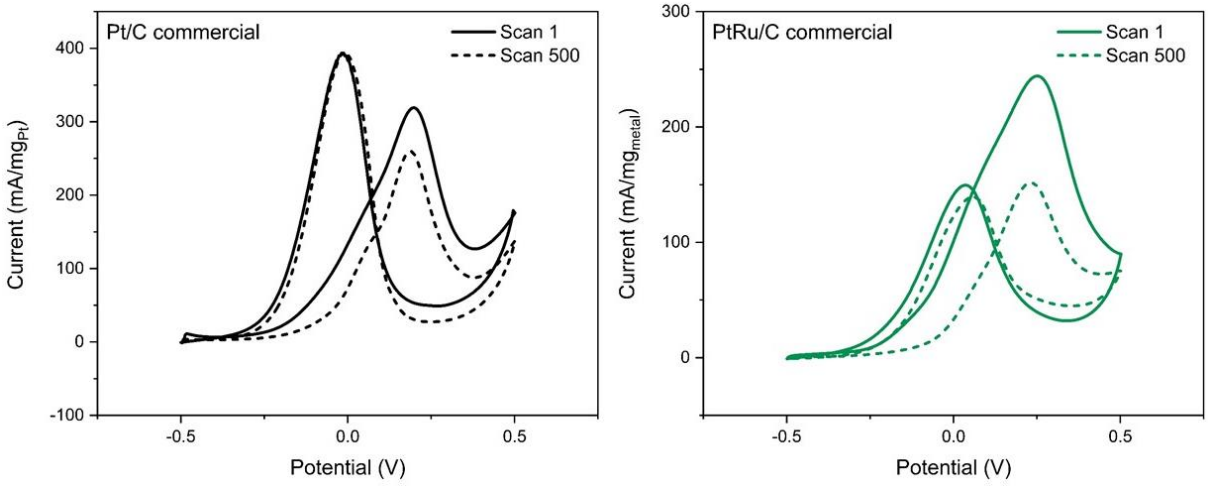

Figure 7.19 500 cycle MOR accelerated degradation for Pt/C_{com} and PtRu/C_{com}.

In stark contrast, both commercial catalysts, whose accelerated cycle test cyclic voltammograms can be seen in Figure 7.19, show a more drastic decline in forwards peak current after 500 degradation cycles. The PtRu/C_{com} shows the most drastic drop, losing 37.6%, while Pt/C_{com} shows an 18.7% drop. It is worth noting that the PtRu/C_{com} catalyst drops drastically in the initial 200 cycles, and thereafter is very stable. So, it is this initial drop in

performance that makes this catalyst appear so bad. On the other hand, the Pt/C_{com} catalyst has a steady decline upon degradation cycling.

The forwards peak for the commercial catalysts appears to show a shoulder on the lower potential side. The origin of this step is believed to be due to the dual pathway for the methanol oxidation reaction[34]. Differential electrochemical mass spectrometry proves that the forwards peak is actually made of two components, one for each pathway (a diagram of this dual pathway is shown in Figure 2.3). It is the prevalence of the two MOR pathways which gives rise to this shoulder to the MOR peak, as the two pathways occur at slightly different potentials. Such a shoulder is not as obvious for the Pt/MnO_x-CB catalyst (Figure 7.18), which indicates that only one pathway is preferred for this catalyst/support system. This may explain why the Pt/MnO_x-CB exhibits a superior durability.

The percentage drop in forwards peak current activity for Pt/C_{com} and Pt/CB are 18.7% and 11% respectively, which is relatively similar – as to be expected for similar catalysts. The Pt/MnO_x-CB shows a dramatic improvement, with only a 4.7% drop after 500 cycles. The MOR degradation cycles for the Pt/MnO_x-CB can be seen in detail in Figure 7.20. This Pt/MnO_x-CB shows signs of being an extremely durable catalyst/support system, even more so than the commercial alternatives. 1000 cycles were performed on this catalyst, with improved temperature control. The temperature was still not completely stable, however much greater control was achieved for this single test over the other synthesised catalyst/support tests previously discussed in this chapter, meaning this result can be compared to the commercial catalyst tests which did have greater temperature control over a longer number of cycles.

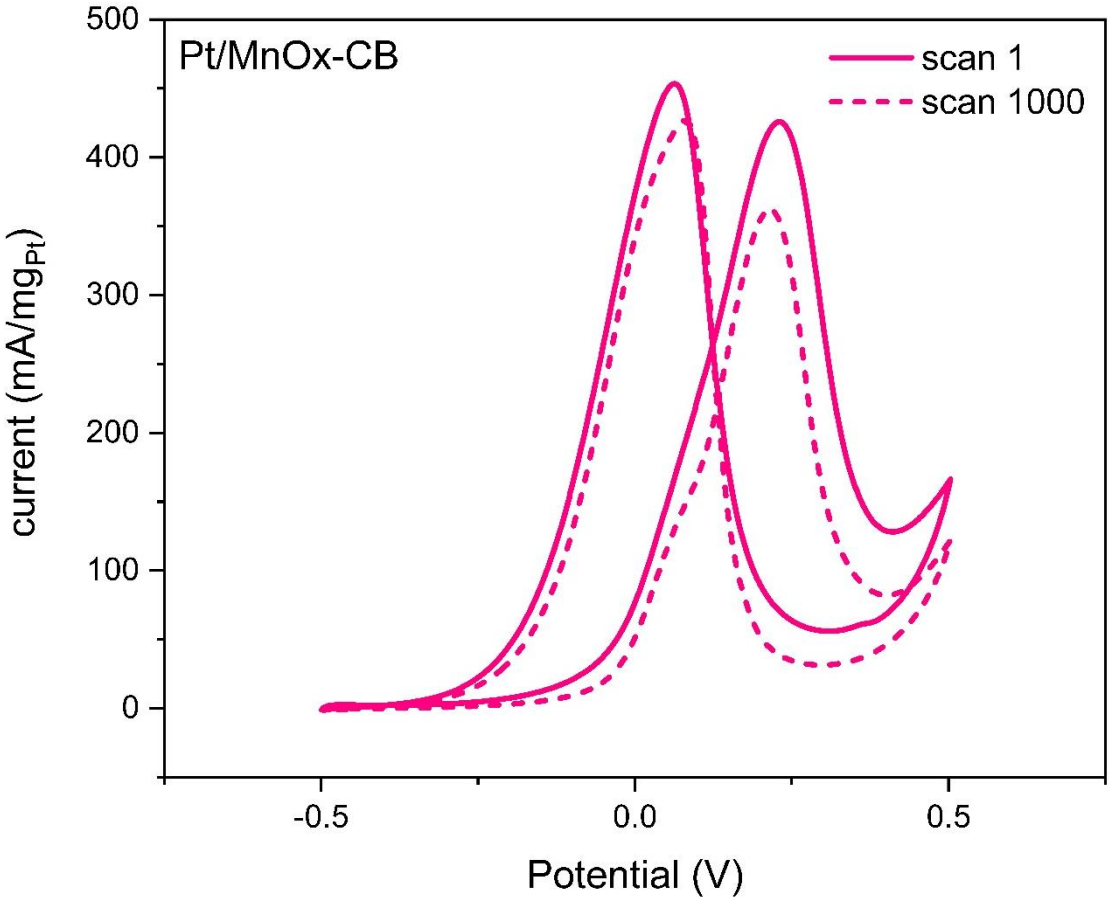

Figure 7.20 1000 MOR cycles for Pt/MnO_x-CB.

After 1000 MOR cycles, the forwards peak current has dropped by only 15.0%. This is less than Pt/C_{com} had dropped after just 500 cycles, and much less than PtRu/C_{com} had dropped over only 500 cycles. This proves that this Pt/MnO_x-CB catalyst/support system is highly durable, even more so than the commercial catalysts, and is a very good candidate to investigate further for an anode material for use in direct methanol fuel cells.

It may be that the structure of the catalyst/support system, being highly rough and porous, enables a high CO to CO_2 conversion, as proposed by Wang et.al[33] which contributes to the durability of this material. In addition, in previous chapters it has been shown that the addition of manganese oxide into the support enhances the durability of the catalyst. There

may be a number of reasons why the addition of MnO_x may improve the durability[40]. The channels in the tunnel structures of manganese oxides allows for fast ion (and proton) transport, improving the adsorption and desorption of hydrogen, and helping the adsorbed CO to be oxidised. Hydrogen and CO are believed to be able to migrate or spillover from the Pt to the MnO_x support, leaving the Pt active sites available for further methanol oxidation. In addition, MnO_2 may generate hydroxyl species, which can then help to oxidise the CO intermediates on the Pt[179]. However, in addition to these suspected improvements from the MnO_x, it must be remembered that the structure of the Pt is also important. An optimum Pt particle size of around 2 nm and a tight distribution, as seen for the Pt/MnO_x-CB will also contribute to the improved durability and performance of this candidate material.

7.4 Conclusions

A three-dimensional carbon in the form of Vulcan XC72 carbon black was used as the carbon base to a manganese oxide – carbon catalyst support. Manganese oxide was grown directly onto the carbon black, and found to have a nanorod structure, which is drastically different from the sheet-like structure formed on graphene oxide, despite using the same MnO_x deposition method and conditions. This implies that the carbon base to the support has a great impact on the structure of the MnO_x formed. The deposited MnO_x was found to be in a mixed oxide state, based around MnO_2/Mn_2O_3.

Deploying a direct growth mechanism for the platinum catalyst yielded a drastically different looking platinum catalyst on plain carbon black vs MnO_x-CB. The MnO_x-CB grew very small, and evenly dispersed platinum nanoparticles 2.13 nm ± 0.41 nm in diameter, with Mn and Pt

distributed evenly across the CB (as shown by EDX mapping). The carbon black on the other hand grew less uniformly dispersed larger particles at 3.42 nm ± 2.27 nm in diameter. In addition, 25.7% loading was achieved on Pt/CB whereas 28.6% loading could be achieved on Pt/MnO_x-CB indicating a greater number of defects and higher roughness on the MnO_x-CB support than the CB support, enabling the higher Pt loading. Despite these structural differences, XPS showed that the oxidation states of the platinum particles grown were very similar, and XRD proved that they were crystalline in both cases. The smaller size Pt particles seen on the MnO_x containing carbon black support reflects the trend seen in Chapter 6 where increasing manganese content led to smaller deposited platinum nanoparticles because of the increase in surface roughness and defect sites on which the Pt can grow.

Accelerated degradation testing showed that the microwave produced Pt/CB performed comparably to the commercial Pt/C_{com}, although the Pt/CB was slightly more durable (Pt/CB had a forwards peak current drop of 11% whereas Pt/C_{com} had a drop of 18.7%). The PtRu/C_{com} suffered from a dramatic initial drop in the first 200 cycles, leading to a poor durability. The addition of MnO_x to the carbon black support had a dramatic improvement on the durability in accelerated tests, losing only 4.7% over 500 cycles, and only 15% over 1000 cycles. This dramatic improvement seen on the addition of MnO_x to the carbon support is of great interest, as this catalyst only uses 30% precious metal loading, in comparison to the 75% metal loading for PtRu/C_{com} and the 30% loading for Pt/C_{com}. This means that a highly durable, relatively low loading catalyst for the direct methanol fuel cell anode has been successfully produced.

CHAPTER 8 Test case: Can utilising a MnO_x-CB support improve a poor catalyst?

The results from this chapter were obtained during a collaborative research project, involving two other PhD students from the University of Birmingham at the time: James Walker from Chemical Engineering and Patrick Harrison from Physics.

The work on the RuSePt/MnO_x-CB was split as follows:

Patrick Harrison:

- *Operation of the TEM including imaging and EDX mapping.*

James Walker:

- *Synthesis of the RuSePt*[183]*.*
- *Sonication of the MnOx-CB and RuSePt to form the RuSePt/MnO_x-CB.*
- *Testing and characterisation of the RuSePt.*
- *Electrochemical tests of the RuSePt/MnO_x-CB including ECSA, pack away of IL-TEM electrode system after long term cycling.*

Aimee Jackson:

- *Synthesis of the MnO_x-CB.*
- *Sonication of the MnO_x-CB and RuSePt to form the RuSePt/MnO_x-CB*
- *Testing and characterisation of the MnO_x-CB.*
- *Electrochemical tests of the RuSePt/MnO_x-CB including long term MOR, set up of IL-TEM electrode system for long term cycling.*
- *Testing and characterisation of Pt/MnO_x-CB and commercial catalysts for comparison.*

In previous chapters, it was shown that the addition of a MnO_x-CB support can improve the durability of a platinum catalyst support. Therefore, in order to test the suggestion that the addition of MnO_x to a carbon support can improve the durability of the supported catalyst towards the methanol oxidation reaction, a test case was set up. A novel catalyst that has poor activity and durability was used – in this case a RuSePt alloy. It was supported on the MnO_x-CB produced in Chapter 7, and some preliminary tests were undertaken to determine the long term MOR activity and durability of the catalyst to see if the MnO_x-CB support could improve it.

8.1 Synthesis

In contrast to previous chapters, where a direct growth method was used, this RuSePt/MnO_x-CB catalyst/support system was produced by sonicating the pre-made support and pre-made catalyst nanoparticles together. 1 mL of pre-made RuSePt nanoparticles (see Appendix A: for details) were suspended in ethanol/hexane (1:1) and mixed with 1 mg MnO_x-CB in a sample vial. This was then sonicated in a sonic bath for 1 hour, to allow the support and catalyst to thoroughly disperse and attach together. A second sample of RuSePt/CB was also produced via the same method but using Vulcan XC72 carbon black rather than the MnO_x-CB. Attaching a catalyst to a support by mixing is a common procedure and allows the pre-made particles to adhere to defect locations on the support.

8.2 Characterisation

From synthesis parameters and previous characterisation studies, the RuSePt particles are assumed to be in a 1:1:1 elemental ratio and are capped by an oleylamine capping agent. Further details on the RuSePt particles can be found in Appendix A:.

MnO_x-CB is known to be 59% MnO_x on Vulcan XC72 carbon black. The MnO_x is crystalline in nature. It is a MnO_2/Mn_2O_3 mixed oxide, and the MnO_x forms a nanorod like structure across the surface of the carbon black (see Chapter 7).

After the RuSePt/MnO_x-CB catalyst/support was produced, it was characterised by TEM and EDX to confirm adhesion of the particles to the support. Since the catalyst particles were very small[183] (3 nm on average), an aberration corrected STEM was used to obtain clear images and high magnification.

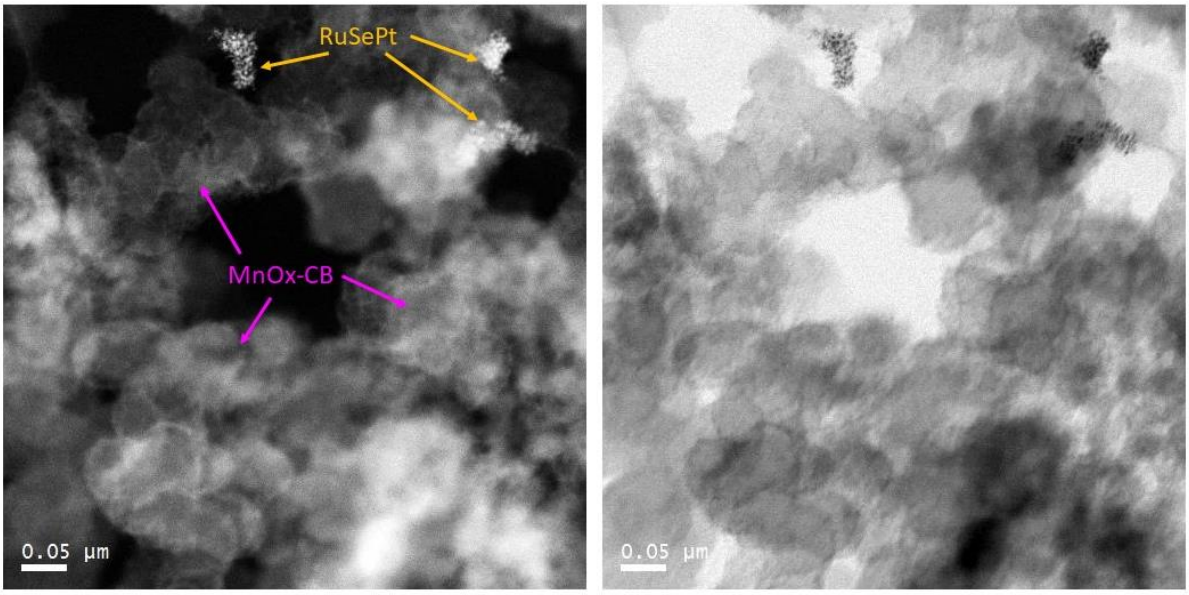

Figure 8.1 HAADF-STEM and bright field STEM images of RuSePt/MnO_x-CB before any electrochemical testing.

The TEM images in Figure 8.1 show that the MnO_x-CB support has retained its three-dimensional structure, as evidenced by the varying levels of focus throughout the image. The rough surface of the MnO_x-CB indicates that the MnO_x nanorod like structure (as discussed in Chapter 7) of the MnO_x-CB has been retained during the catalyst deposition step.

The RuSePt catalyst nanoparticles have remained as discrete particles but have clustered together and attached themselves in selected locations on the MnO_x-CB support. The poor dispersion of these particles is expected to have a detrimental effect on their electrochemical activity as the electrolyte and reactants will not be able to access in between these clustered particles. In addition, only some of the RuSePt particles are in contact with the catalyst support. This will have an additional detrimental effect on the catalytic activity and effectiveness in a fuel cell, as the electrons produced from the MOR reaction on nanoparticles away from the support will not have a conductive pathway to follow out to the external circuit, meaning they do not contribute to the activity of the catalyst for the fuel cell. In addition, the poor contact of the particles on the support may hinder the durability performance of the catalyst/support system.

From the HAADF-STEM images in Figure 8.2, it is not clear whether the oleylamine capping agent has been removed during the catalyst deposition step. However, since the particles are grouped together, but not in direct contact, it is expected that at least some of the capping agent is present because the capping agent would keep the particles separated. This is confirmed by the HR-TEM images, which show some crystallinity of the particles but also shows some 'fuzziness' or variation in focus, indicating the likely presence of a film - presumably the capping agent covering the particles. Despite the presence of the oleylamine capping agent in the image, there are clearly crystalline RuSePt nanoparticles, with a measured lattice spacing of 0.24 nm ± 0.5 nm. This was calculated from the line profile of a particle on the image, shown in the inset of Figure 8.2. This lattice spacing is consistent with Pt under tensile strain[184,185], as would be the case for such a Pt-RuSe alloy.

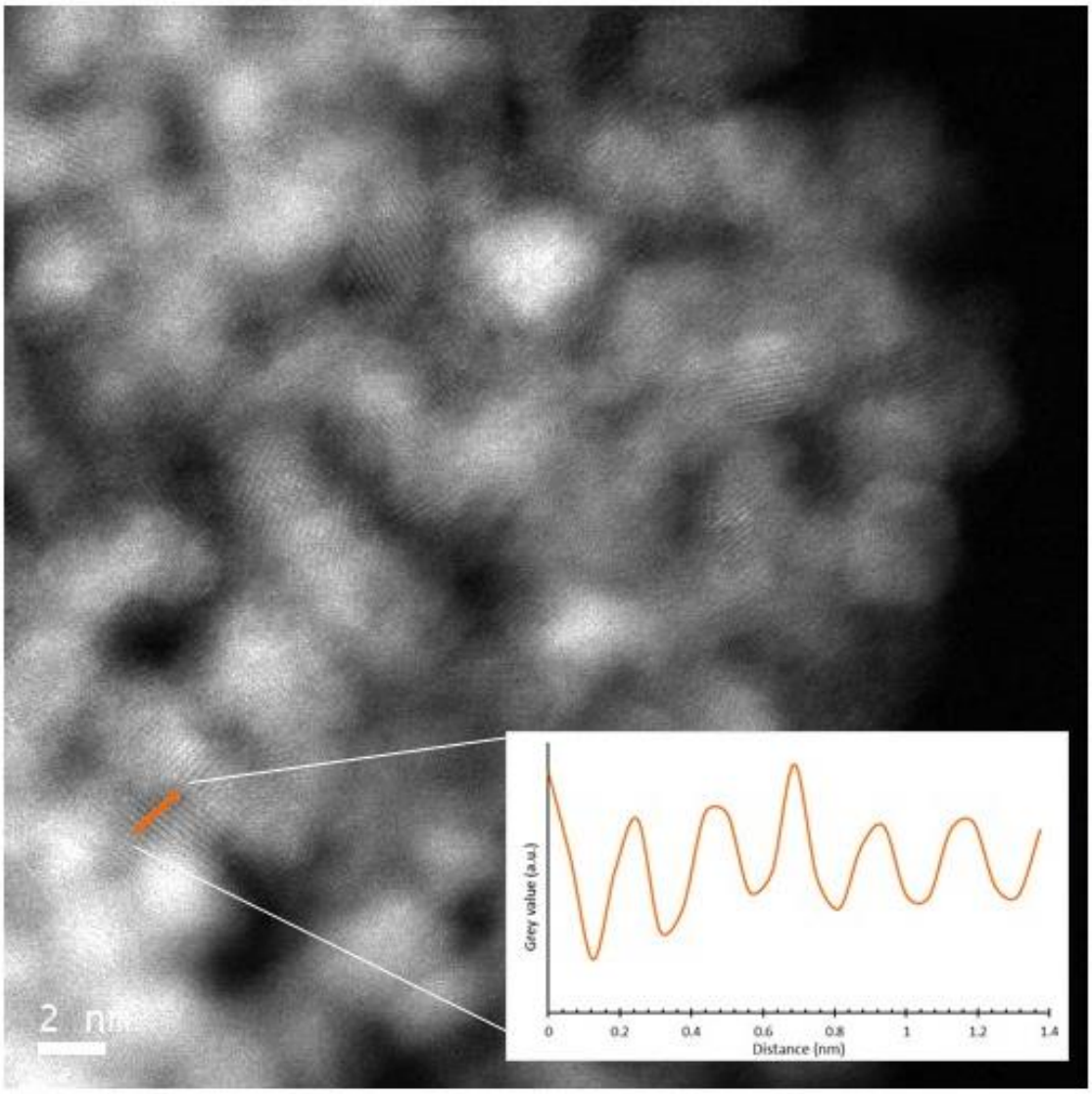

Figure 8.2 HAADF-STEM image showing the RuSePt particles. Inset: line profile across a RuSePt particle, showing the lattice spacing and the crystalline nature of the RuSePt particles.

8.3 Electrochemical testing

For the electrochemical measurements, a 3mm glassy carbon working electrode was used, with an Ag/AgCl reference electrode, and a platinum mesh counter. The electrolyte was 1M methanol/0.1M H_2SO_4 and the catalyst/support systems tested by potential cycling. A catalyst ink was made from 1mg of catalyst/support powder and 1ml of Nafion ink – the same as

previous chapters in this thesis. 2 x 5 µL drops of this ink were cast onto the 3mm glassy carbon electrode, and dried using a heat lamp prior to testing.

8.3.1 RuSePt/CB electrochemical performance

In Figure 8.3, it can be shown that the RuSePt catalyst on CB shows some activity towards the MOR, however this activity is very poor, lower than for the commercial Pt/C_{com} or $PtRu/C_{com}$ and the Pt/MnO_x-CB from Chapter 7. The RuSePt/CB material also exhibits a large capacitance – evident from the large separation between the forwards and backwards parts of the MOR graph – shown in Figure 8.3.

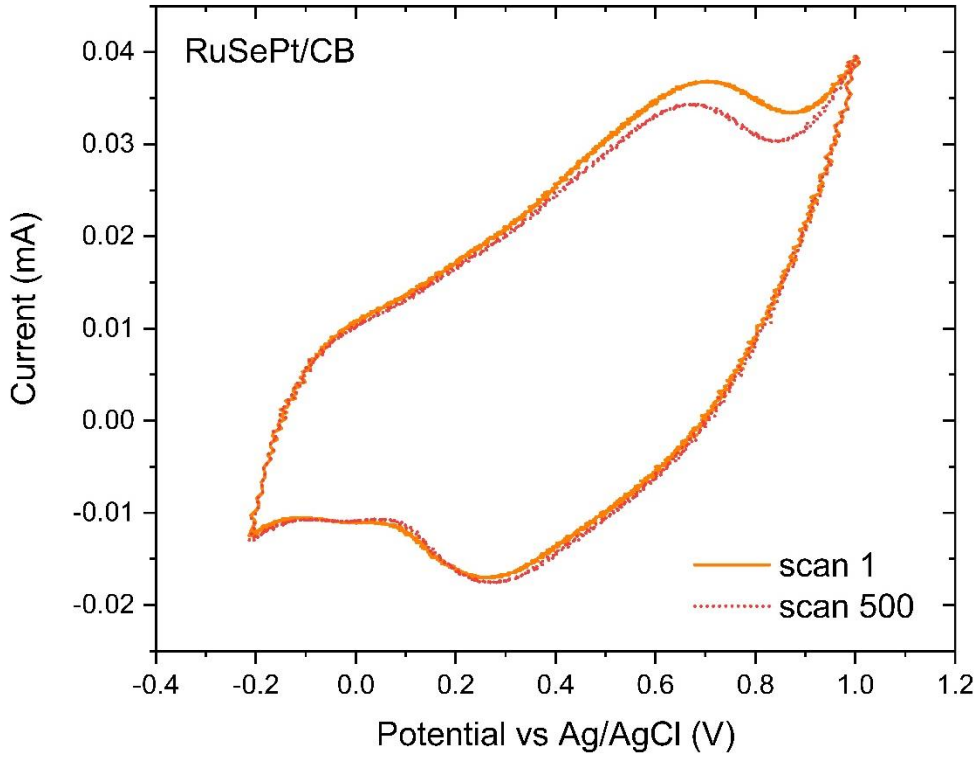

Figure 8.3 500 MOR cycles for RuSePt/CB.

The RuSePt/CB shows some durability however, losing only 8% of its initial forwards peak current after 500 cycles although it is not clear if this peak is a genuine MOR peak, or if it is

some kind of diffusive reaction occurring on the RuSePt particles. Further detailed investigation into the kinetics of this peak would be required, however this was beyond the scope of this experiment. This relatively good durability exhibited (if indeed it is a genuine MOR peak) may be enhanced through use of an MnO_x-CB support as in previous chapters, in addition to potentially improving the magnitude of the MOR current produced.

8.3.2 RuSePt/MnO_x-CB electrochemical performance

In order to ascertain the effect of the MnO_x support, a series of electrochemical measurements were made.

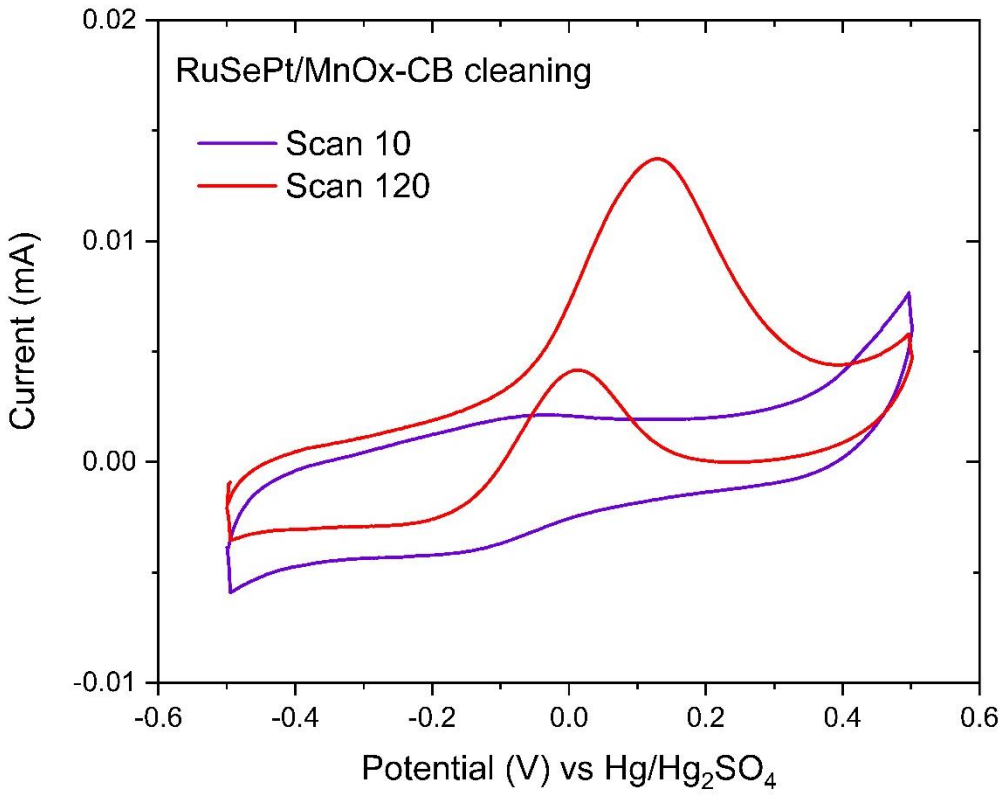

Figure 8.4 MOR cleaning cycles for RuSePt/MnO_x-CB showing the methanol oxidation peaks appearing after 120 cleaning cycles.

First, the RuSePt/MnO_x-CB was tested on a 3mm glassy carbon static electrode, to compare to the RuSePt/CB, it was tested for 1500 cycles (after electrochemical cleaning) to determine the long term behaviour of the catalyst and see if the durability could be improved.

The MOR cleaning cycles are shown in Figure 8.4. The first approximately 10 cycles show no catalytic behaviour towards the MOR, and just a resistive/capacitive type loop. On the other hand, Pt/C_{com}, PtRu/C_{com} and Pt/MnO_x-CB all exhibit some MOR behaviour on their initial cycles, whose peak current increases with some cleaning cycles.

After around 20 – 30 potential cycles, the MOR behaviour for the RuSePt/MnO_x-CB begins to become apparent, and the forwards peak current ($I_{f\ Peak}$) shows a maximum at around 120 cycles. This contrasts with the RuSePt/CB which still shows no MOR activity. Including MnO_x in the system appears to enhance the electrochemical cleaning of the RuSePt catalyst to allow the MOR reaction to take place, although the mechanism through which this happens is unclear. This cleaning behaviour exhibited by the RuSePt/MnO_x-CB is different to the cleaning behaviour seen in all other catalysts tested previously (Chapter 5 to Chapter 7). The Pt or PtRu catalysts from previous chapters all exhibit some MOR activity in the initial scan, which simply increases in peak current over 20 to 60 cycles. In the case of RuSePt/MnO_x-CB, this initial activity is not evident and must be slowly revealed and obtained over >100 potential cycles. This effect may be due to the capping agent which is present on these RuSePt particles, but not present on the commercial catalyst or the Pt/MnO_x-CB. Even after this cleaning cycling, the peak currents obtained are much lower than those obtained for the Pt/C_{com}, PtRu/C_{com} and Pt/MnO_x-CB. These low currents may be caused by a number of physical characteristics including:

i. Poor contact between catalyst and support due to the procedure used to deposit the catalyst onto the support.

ii. Poor dispersion of the catalyst particles on the support.

iii. Few catalyst particles in direct contact with the support.

iv. Effect of the capping agent on the catalyst particles.

After electrochemical cleaning, the MOR activity was measured over 1500 cycles. (for degradation cycling, the start = scan 1 = cleaning cycle 120 = the maximum initial activity)

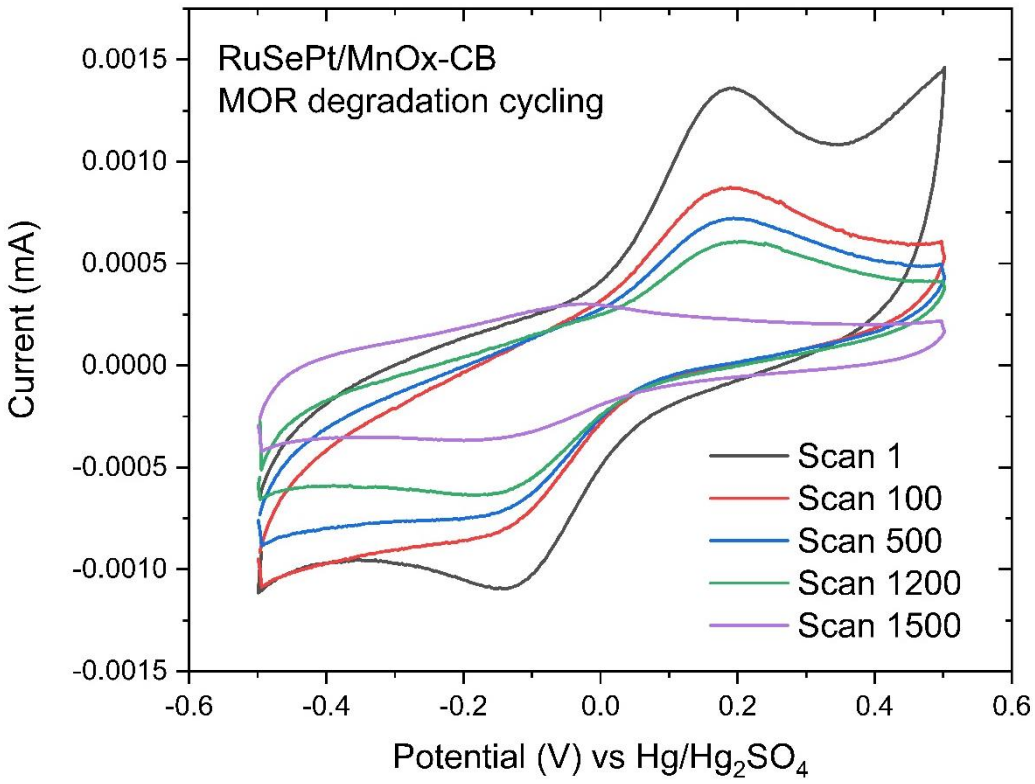

Figure 8.5 MOR degradation cycles for RuSePt/MnO_x-CB material on a 3mm glassy carbon electrode.

The degradation cycling for RuSePt/MnO_x-CB (Figure 8.5) shows the peak current drops by 48% over 100 degradation cycles, and by 55% after 1200 cycles. The voltammetry changes

significantly between scan 1200 to 1500, such that all electrochemical activity is gone by 1500 cycles.

In addition, upon cycling for 1500 potential cycles, the MOR behaviour appears to have disappeared, and the shape of the cyclic voltammogram appears to be more diffusive in nature rather than adsorptive. The peak shape is asymmetrical and there is a wide peak separation, indicating the diffusive nature of the reaction. An investigation with varying scan rates would confirm this and enable more detail on the mechanism to be obtained, however this was not in the scope of this preliminary study.

The shape and the potential at which the peaks occur indicate that there is oxidation and reduction of manganese or ruthenium occurring in the catalyst/support system. The standard potential for Mn(VII) to Mn(IV) is 0.60V (vs SHE) and the standard potential for Ru(IV) to Ru(II) is 0.68V (vs SHE)[186]. These match well with the potential of the observed peaks, suggesting that reduction/oxidation of ruthenium or of manganese oxide may be responsible for this shape. To investigate the effect of cycling on the catalyst and support in more depth, identical location TEM was performed before and after potential cycling. Any changes in the structure or in the elemental composition of the catalyst/support should be observable via the TEM image and the EDX map. This was done by identical-location TEM and EDX before and after MOR electrochemical cycling.

8.3.3 IL-TEM coupled MOR potential cycling

To measure the structural differences in the RuSePt/MnO_x-CB before and after MOR cycling, identical-location TEM was used (IL-TEM). First, TEM images and EDX maps were obtained at a specific location on a TEM grid to examine the RuSePt/MnO_x-CB before potential cycling.

8.3.3.1 IL-TEM imaging before electrochemical cycling

1 µL of catalyst ink (at 1 mg/mL catalyst powder in Nafion solution) was applied to a gold TEM grid, and allowed to dry, before being imaged using TEM. These initial TEM and EDX images can be seen in Figure 8.6 and Figure 8.7.

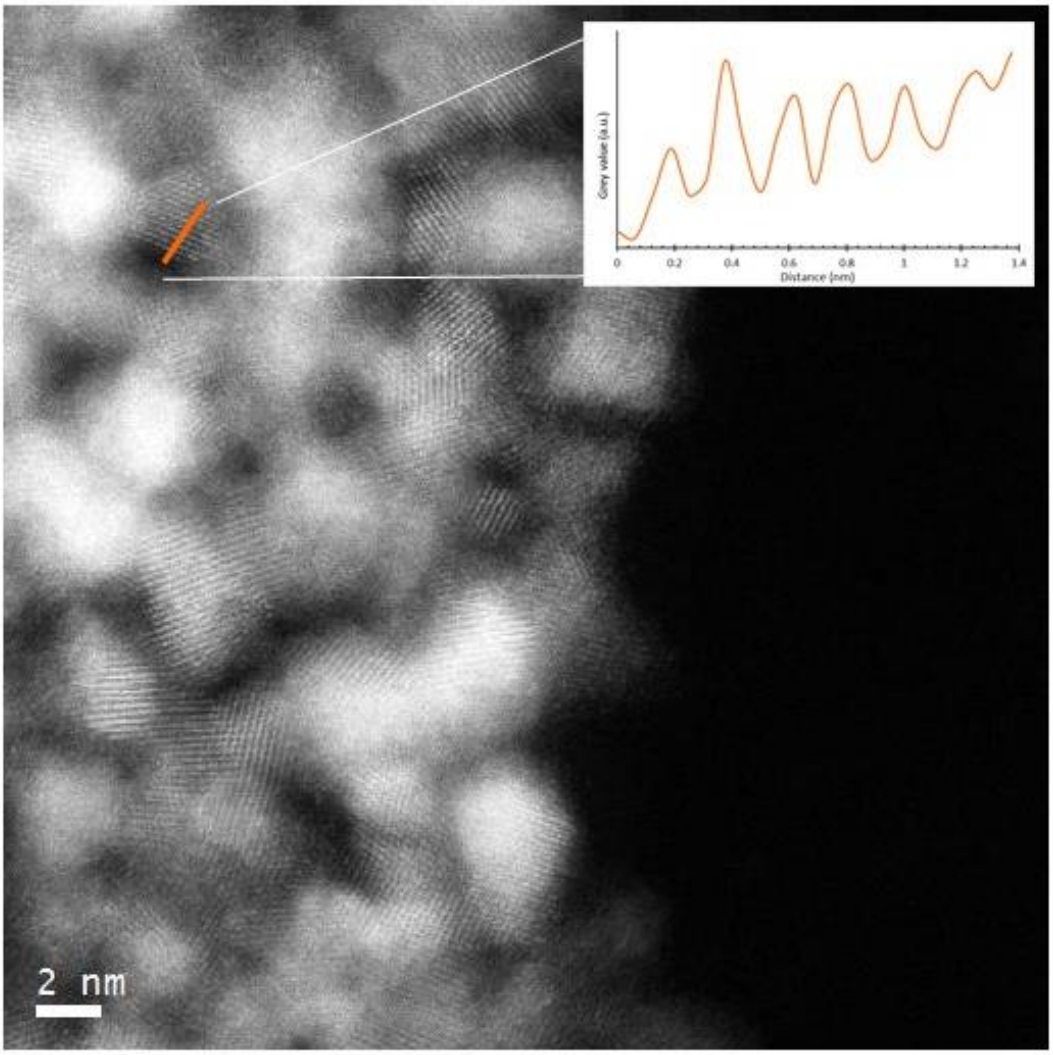

Figure 8.6 HR-TEM image showing the RuSePt particles before electrochemical cycling. Inset: line profile showing the lattice spacing of a single RuSePt particle.

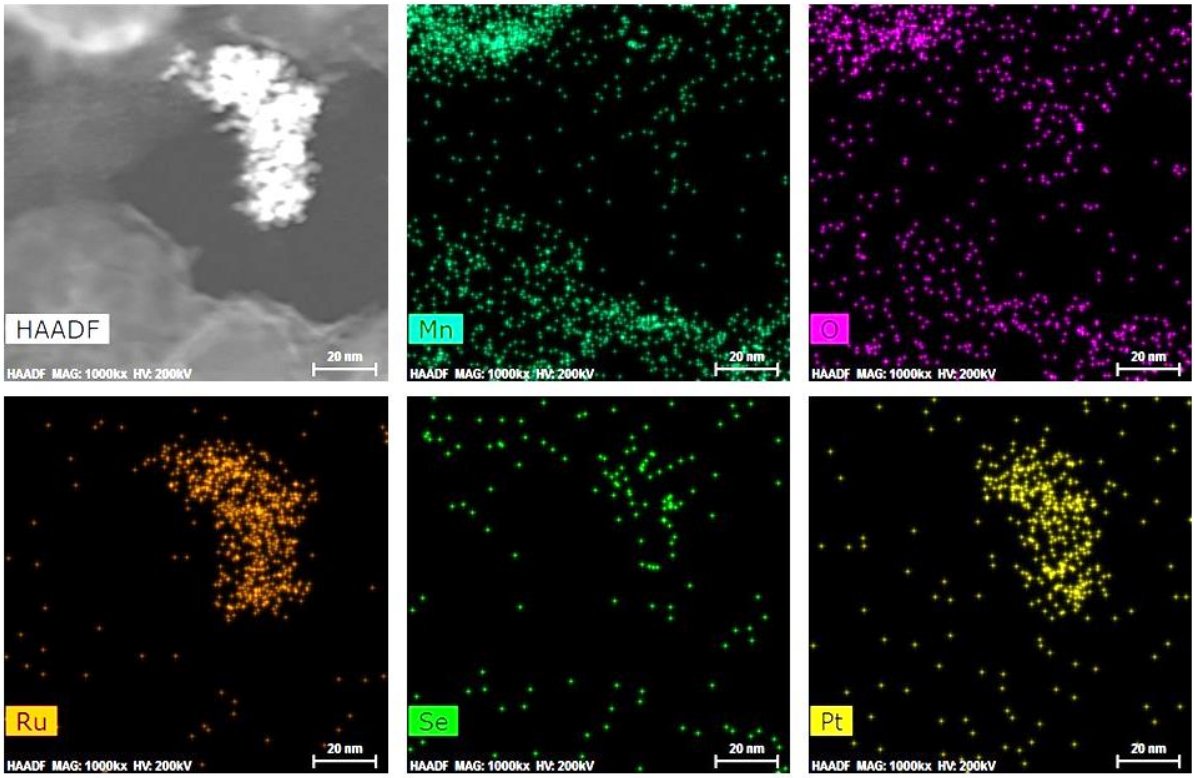

Figure 8.7 EDX maps before MOR cycling, showing the HAADF image along with the Mn, O, Ru, Se and Pt elemental maps.

The TEM image shows the same trend as in section 8.2. The RuSePt particles are attached in groups onto the MnO_x-CB support. There is also some evidence for the presence of the oleylamine capping agent, due to the distribution of the RuSePt particles and the fuzziness visible on the crystalline particles. From the line profile, the lattice spacing for the particles is 0.22nm ± 0.5nm. This is very similar to the not cleaned particles shown earlier in this chapter, and matches with a Pt-alloy where the Pt lattice is under tensile strain[184,185] as is to be expected for a RuSePt alloy particle.

The EDX map shown in Figure 8.7 shows the distinct areas of the catalyst RuSePt and the support MnO_x-CB. The RuSePt alloy particles appear to be clustered together and have not

been well dispersed. Despite this, the RuSePt cluster is attached well to an area of MnO_x-CB support. The MnO_x is well distributed across the entire carbon black support.

8.3.3.2 Electrochemical cycling after initial IL-TEM imaging

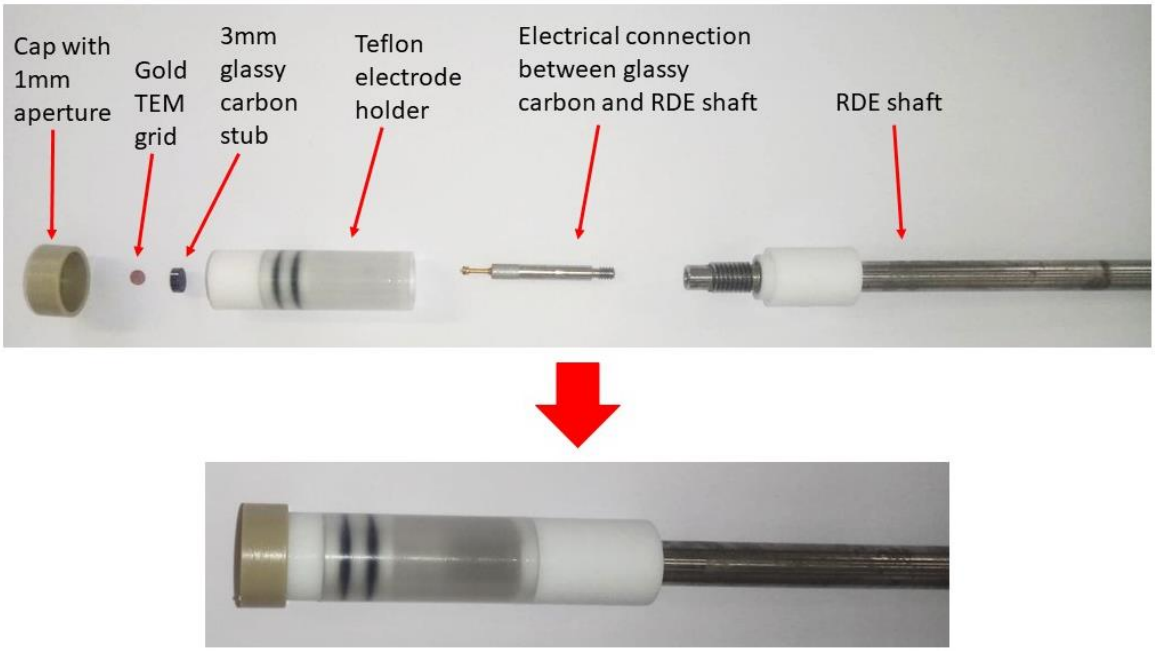

Figure 8.8 IL-TEM electrochemical potential cycling setup.

After the initial TEM image was taken, the TEM grid was mounted onto an electrode using the setup shown in Figure 8.8. The TEM grid was taken out of the TEM, and placed onto a polished 3mm glassy carbon stub, which had previously been inserted into a Teflon electrode holder. The TEM grid was held in place by a Teflon cap, which had a 1mm diameter hole drilled in the centre to allow the electrolyte access to the catalyst particles on the TEM grid. The assembled electrode was then attached to the RDE shaft and connected to the potentiostat by a crocodile clip on the RDE shaft.

The electrochemical results from this setup are inherently different to those found from the standard 3mm glassy carbon electrode, coated with 10 µL of catalyst ink (at 1 mg/mL). This difference in the electrochemical scan arises not only from the difference in the quantity of catalyst on the electrode, but also because of the gold TEM grid, and the 1 mm aperture in the cap which holds the TEM grid in place. These all contribute to a much lower current signal, which is hardly visible on the potentiostat used, therefore the electrochemical scans from the IL-TEM setup are not shown here. However, it is assumed that the potential cycling affects the catalyst particles in the same way, and therefore the images before and after electrochemical cycling are assumed to be representative of what happens at the catalyst surface during MOR electrochemical cycling.

To see what the MOR cycles looked like, the MOR potential cycling was measured using the same RuSePt/MnO_x-CB ink as was deposited on the gold TEM grid, but with the ink deposited on the 3mm glassy carbon static electrode and attached to the RDE shaft. There was no TEM grid present and no 1mm aperture cap on top. The same counter and reference electrodes were used, along with the same cycling procedure. These adjustments allowed for a strong enough current to be observed from the potentiostat output. These cycles are shown in Figure 8.5 above. The peak current drops by 55% after 1200 MOR cycles, and all electrochemical activity is gone by 1500 cycles.

8.3.3.3 IL-TEM imaging after electrochemical cycling

After the potential cycling was complete, the gold TEM grid was carefully removed from the mounted setup and placed back into the TEM for imaging.

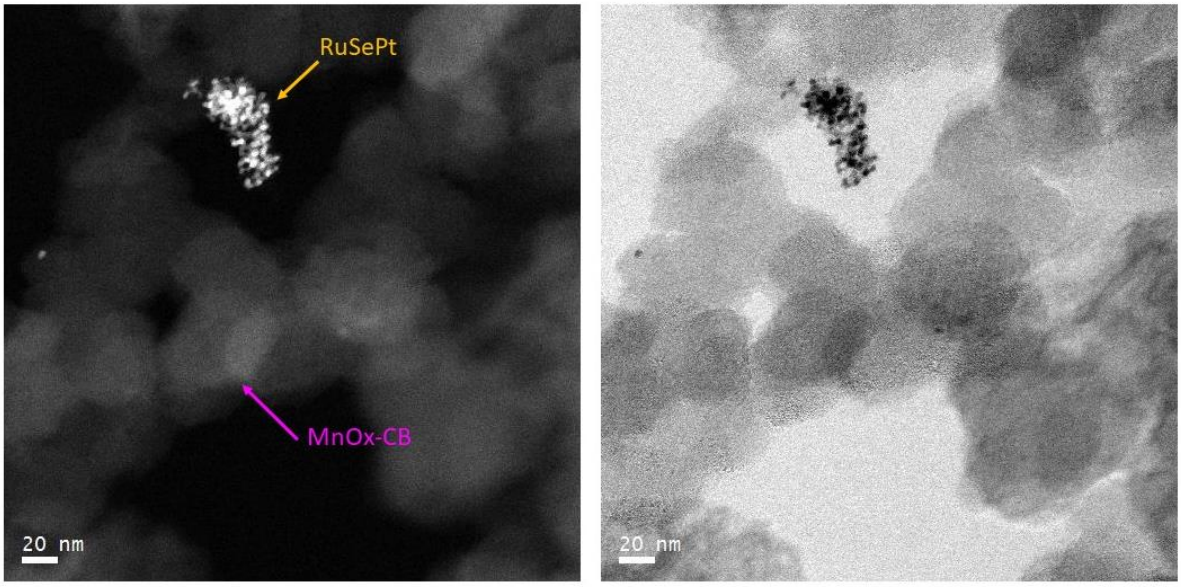

Figure 8.9 HAADF-STEM and Bright field STEM images of RuSePt-MnO_x-CB after electrochemical testing.

The same location was found on the TEM grid, and these post cycling STEM images can be seen in Figure 8.9. The post-cycling TEM images show less evidence for the MnO_x nanorod type structures on the surface of the carbon black, and instead show a smoother support, more visually similar to the unmodified vulcan carbon black.

The aberration corrected HR-TEM images post-cycling (Figure 8.10) show more clear crystalline RuSePt particles, which suggests that the capping agent has been removed through the process of potential cycling. The lattice spacing is measured to be 0.23 nm ± 0.5 nm post-cycling which has not changed from before cycling. This lattice spacing still matches with the values for a Pt lattice under strain[184], as is the case for a RuSePt alloy.

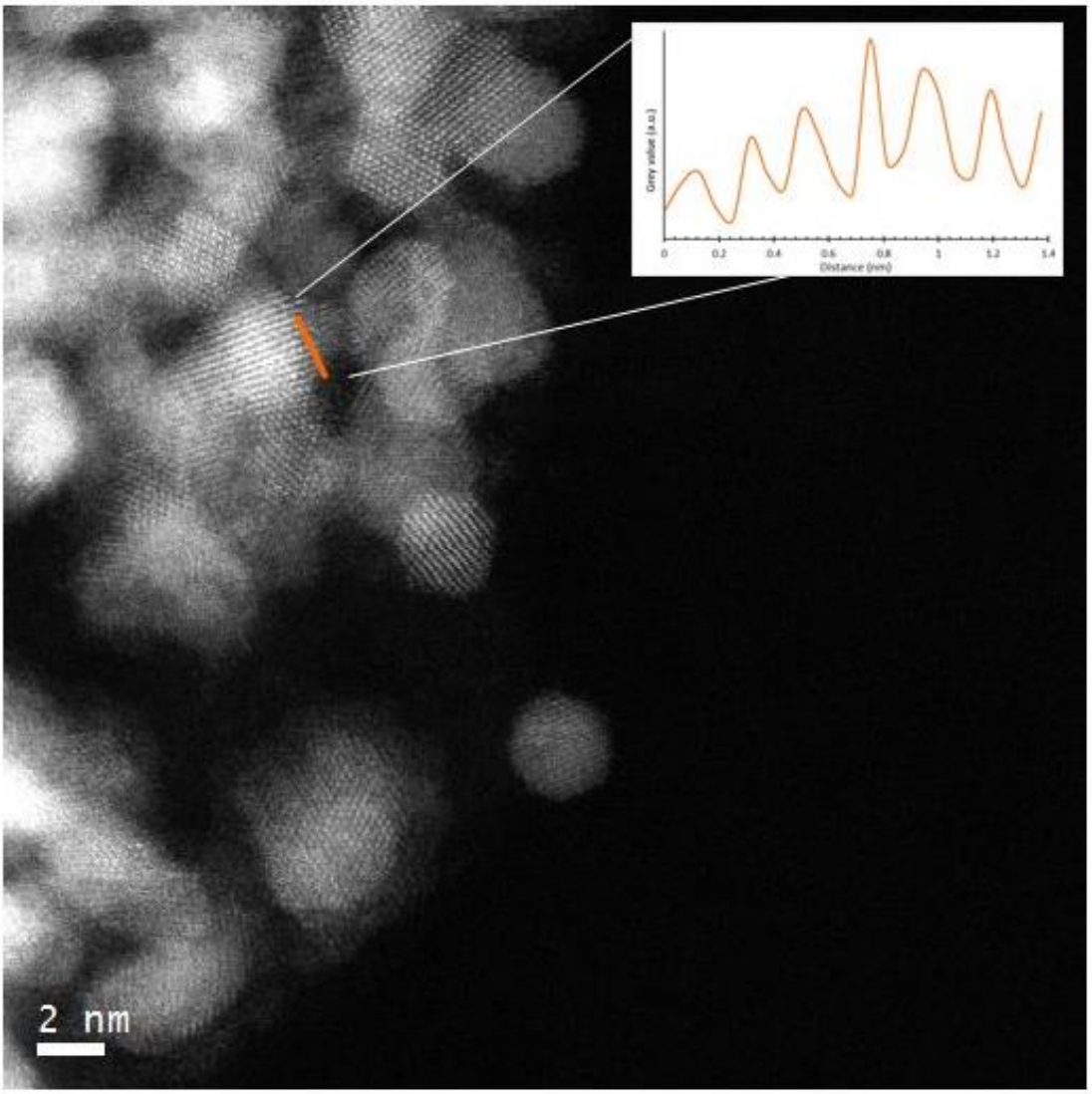

Figure 8.10 Aberration corrected HR-TEM image showing the RuSePt particles after electrochemical cycling. Inset: line profile across the same RuSePt particle from before cycling, showing the crystallinity and lattice spacing has not changed.

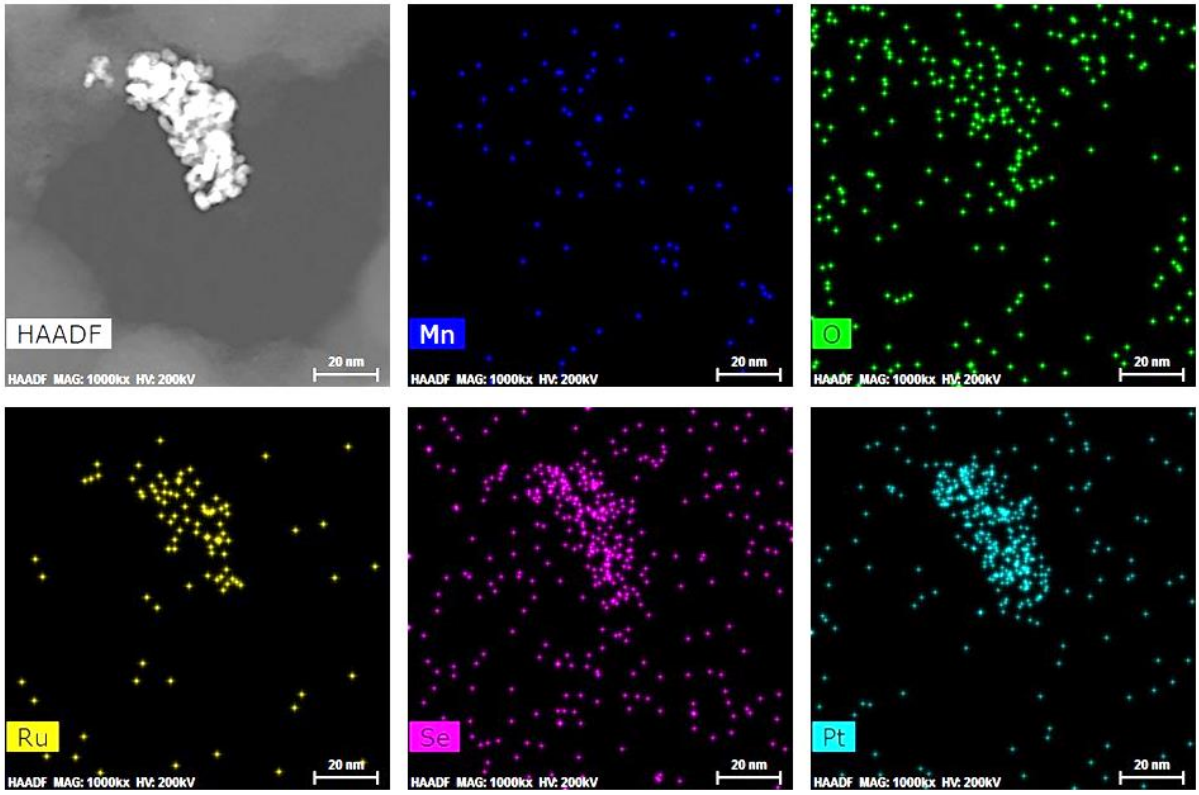

Figure 8.11 EDX maps after MOR cycling, showing the HAADF image along with the Mn, O, Ru, Se and Pt elemental maps.

In addition, the Mn signal in the EDX mapping (Figure 8.11) is much weaker, indicating that the Mn has been leached out of the system during cycling. This matches with the visual clue that shows the MnO_x nanorod type structure to have been diminished in the post cycling TEM image (Figure 8.9).

8.3.4 Testing the electrolyte from the RuSePt/MnO_x-CB MOR cycles for leached out catalyst elements

To further test the possibility that the MnO_x is leached out from the RuSePt/MnO_x-CB, another electrochemical cycling measurement was performed. The same batch of 1M methanol/0.1M H_2SO_4 electrolyte was used for each of these experiments in this series, and

it was tested before and after potential cycling of each catalyst using ICP-MS, measuring for all elements of interest present in the system: Pt, Ru, Se and Mn. This was to see if any of the elements in the RuSePt/MnO_x-CB system leach out during the course of the electrochemical cycling, and to see if this may contribute to the cyclic voltammogram measurements seen (Figure 8.5). Any elements from the RuSePt/MnO_x-CB that have been leached out during the process of MOR cycling will be present at elevated levels in the electrolyte. The RuSePt/MnO_x-CB was mounted on a 3mm glassy carbon working electrode, using 10 µL of 1mg/mL catalyst ink and a heat lamp to dry. To ensure that the only Pt in the system could come from the working electrode, the counter electrode in this experiment was a carbon rod, and the reference used was a Hg/Hg_2SO_4. A 30ml sample of the 1M methanol/0.1M H_2SO_4 electrolyte before cycling was retained as a 'blank' sample. Then, the 3 electrodes were set up in a standard electrochemical setup, using a second portion of the same batch of 1M methanol/0.1M H_2SO_4 electrolyte, and the RuSePt/MnO_x-CB was cycled for 1500 MOR cycles. After cycling, the electrolyte was retained for ICP-MS testing. As a comparison, the Pt/MnO_x-CB from Chapter 7 was mounted on a 3mm glassy carbon electrode, using the same experimental set up as for RuSePt/MnO_x-CB. A third portion of the same batch of 1M methanol/0.1M H_2SO_4 electrolyte was used, and this Pt/MnO_x-CB catalyst was also cycled for 1500 cycles, with the post-cycling electrolyte again retained for ICP-MS testing. The cyclic voltammograms are not shown here (although they appear similar to those shown in Figure 8.5), as the main aim of this experiment was to identify any dissolving or leaching of the components of the RuSePt/MnO_x-CB catalyst/support system.

Table 8.1 ICP-MS measurements of Mn, Pt, Ru and Se content of electrolyte before and after electrochemical degradation cycling.

	Mn / ppm	Pt / ppm	Ru / ppm	Se / ppm
Blank electrolyte	0.011 ± 0.001	0.012 ± 0.001	0.005 ± 0.001	0.002 ± 0.001
RuSePt/MnO_x-CB electrolyte after 1500 cycles	0.019 ± 0.001	0.001 ± 0.001	0.001 ± 0.001	0.001 ± 0.001
Pt/MnO_x-CB electrolyte after 1500 cycles	0.009 ± 0.001	0.002 ± 0.001	0.001 ± 0.001	0.002 ± 0.001

The 3 electrolyte samples were tested for the elements of interest: Pt, Ru, Se and Mn using ICP-MS. The ICP-MS results (which can be seen in Table 8.1) show that the blank electrolyte already contains some trace amounts of Mn, Pt, Ru and little Se. After cycling however, the electrolyte from the PtRuSe/MnO_x-CB contains elevated levels of Mn, which are higher than the background (blank electrolyte) measurements. This confirms the observations from TEM and EDX that the Mn has leached out of the RuSePt/MnO_x-CB system. For all other elements, the signal after cycling is not significant above the background, indicating that these elements do not leach significantly from the RuSePt/MnO_x-CB on the working electrode. These results suggest that the diffusive behaviour seen in the MOR cycles in Figure 8.5 is in fact due to reduction/oxidation of manganese oxide and not methanol oxidation. This is responsible for the Mn leaching out into the electrolyte for the case of RuSePt/MnO_x-CB and showing that the RuSePt/MnO_x-CB is not stable.

On the other hand, in the Pt/MnO_x-CB electrolyte, the Mn and Pt signals are not significant compared to the background levels, indicating that the Mn and Pt do not leach significantly in the case of the Pt/MnO_x-CB material, suggesting the MnO_x-CB is not unstable in this system.

In the case of Pt/MnO_x-CB, the Pt and Mn are in direct contact with each other, as the Pt nanoparticles have been deposited via a direct growth mechanism, whereas for the RuSePt catalyst, the Mn and RuSePt particles do not have as much direct contact, as the RuSePt particles are deposited in a post-growth sonication step. The RuSePt particles deposit in clusters in discreet locations on the MnO_x-CB, and are capped with capping agent, leading to decreased contact between the RuSePt and MnO_x-CB in the case of RuSePt/MnO_x-CB, compared to the Pt and MnO_x-CB in the case of Pt/MnO_x-CB. It appears that it is this direct contact between the Pt and MnO_x-CB that stabilises the MnO_x in the support and enhances the durability.

In addition, the presence of oleylamine as a capping agent on the RuSePt nanoparticles may have a detrimental effect on the catalyst/support system. It is known that oleylamine can act as a mild reducing agent[187], and so it is possible that when the potential is cycled, the oleylamine may interact with the catalyst and the support and cause undesirable reduction reactions, leading to the leaching of the MnO_x from the system.

8.4 Conclusions

Initial MOR tests showed that electrochemical cycling cleans the oleylamine capping agent from the RuSePt particles and improves the MOR performance of the RuSePt catalyst. Using MnO_x-CB as a support improves the methanol oxidation activity of the RuSePt catalyst over a standard carbon black support.

IL-TEM and subsequent ICP-MS electrolyte tests show that for the RuSePt/MnO_x-CB, where the catalyst and support have only poor contact with each other, manganese is lost from the support material during electrochemical cycling. This is not the case for Pt/MnO_x-CB, where there is no evidence for manganese leaching out of the support during cycling. It is therefore proposed that the combination of the MnO_x and Pt in direct contact with each other and the direct growth mechanism that gives rise to the stability and durability seen for the Pt/MnO_x-GO and Pt/MnO_x-CB MOR catalysts. In addition, the use of oleylamine as a capping agent to the catalyst nanoparticles is undesirable and its mild reducing agent status may contribute to the degradation of the catalyst/support system.

Further investigation into the mechanism behind the diffusive behaviour observed in the electrochemical cycling experiments for the RuSePt/MnO_x-CB and the cleaning and degradation mechanisms should be undertaken.

CHAPTER 9 Summary

9.1 Conclusions

This study has produced a range of hybrid MnO_x-nanocarbon catalyst supports for use in direct methanol fuel cells. The support materials were subsequently decorated with platinum nanoparticles for testing in an ex-situ electrochemical environment.

Based on a survey of the literature, three synthesis methods were selected.

Firstly, a graphene oxide material was successfully produced, following a modified Hummers method. The graphene oxide produced had a C:O ratio of 3.0 to 3.2, and ICP-MS showed that it was free from any contamination. The dominant oxygen groups on the graphene oxide were hydroxyl and epoxide groups, with only a small contribution from carbonyl and carboxyl groups.

Second, this graphene was taken as a starting point to be modified with a manganese oxide layer using a one pot microwave technique. The one-pot microwave synthesis method was successfully used and reliably enabled the direct growth of MnO_x onto graphene oxide at a range of loadings. MnO_x was grown in a MnO_2/Mn_2O_3 mixed oxide state in crystalline nano layers across the graphene support, which was reduced simultaneous to the MnO_x growth step. This direct growth enabled a good interaction between the GO and MnO_x.

Thirdly, the range of graphene oxide based support materials produced could be decorated with platinum nanoparticles, using a second one-pot microwave synthesis method. Whilst graphene oxide alone as a catalyst support for Pt nanoparticles proved to be unsuccessful over long term ex-situ degradation cycling tests, the MnO_x-GO materials showed a clear

improvement above the GO alone when tested for long term stability. Increasing the MnO_x content above 50% was detrimental to the overall performance, as the GO in this case was not as fully reduced as the supports with lower MnO_x content. This decreased the electrical conductivity of the overall support, and therefore minimised the peak currents that could be obtained from the catalyst under ex-situ tests. However, despite this low activity, the hybrid MnO_x-GO support with the highest loading of MnO_x (68%) produced a very durable catalyst. All MnO_x-GO materials suffered from suspected re-stacking of the sheet structure, which caused a low electrochemical surface area and inhibited the performance. Interestingly, the Pt particle size of the directly grown particles was also influenced by the MnO_x loading. The higher the MnO_x loading on the hybrid support, the smaller the Pt particles that were grown. It is expected that the size of the deposited Pt nanoparticles also had an influence on the durability of the catalyst/support system. The size of the directly grown Pt nanoparticles additionally had a detrimental effect on the electrochemical surface area of the Pt/MnO_x-GO materials, as they tended to have a larger particle size compared to commercial catalysts.

Next, the same one-pot hybrid support synthesis method was utilised to successfully produce a MnO_x-CB hybrid support. The MnO_x was again in a mixed oxide state but differed in its morphology: forming crystalline nanorods rather than the nanosheets that were formed on the GO. This different shape is expected to be a product of the direct growth mechanism, whereby the manganese oxide grows from defect sites on the supporting carbon. There are significantly more defect sites on graphene oxide than on the carbon black, causing sheet like structures to grow across the surface of the graphene sheet vs crystalline nanorods to grow out from the carbon black surface. Using a 3D carbon as the base for the hybrid support overcame the issues of low electrochemical surface area, as the carbon black retained its

porous structure and did not re-stack like the graphene-based supports. Pt nanoparticles grown via a direct route on this MnO_x-CB support exhibited an enhanced durability that was even better than the commercial DMFC anode catalyst in these ex-situ tests. In addition, the deposited platinum nanoparticles were of a small size which contributed to enabling a larger surface area to be obtained. The Pt/MnO_x-CB showed excellent durability and activity towards the methanol oxidation reaction. This MnO_x-CB support highlighted the significant influence of the carbon support on the subsequent growth of the manganese oxide. It also showed that through combining MnO_x and carbon as a support, and through direct growth of platinum catalyst particles, a highly durable MOR catalyst can be produced.

Finally, a test case was set up, combining the MnO_x-CB support and a novel ternary RuSePt alloy nanoparticle catalyst with the aim of investigating whether an MnO_x-CB support can improve any MOR catalyst. Pre-prepared RuSePt nanoparticles were attached to the MnO_x-CB support via a sonication deposition step. It was apparent that an indirect growth mechanism does not produce a well dispersed catalyst on the support. In addition, the nanoparticle's capping agent appears to be detrimental to the performance of this RuSePt/MnO_x-CB catalyst/support system. Identical location TEM imaging and ICP-MS of the electrolyte was performed before and after electrochemical cycling of the MnO_x-CB with the novel RuSePt ternary alloy MOR catalyst particles. This showed that the MnO_x was unstable in this case, and the Mn could be seen to be leaching out into the electrolyte. As a result, these catalyst/support RuSePt/MnO_x-CB particles showed poor activity and poor durability. This indicated that it is in fact the direct contact between catalyst and support and the direct growth mechanism of the MnO_x and Pt that generated the impressive durability that was exhibited by the Pt/MnO_x-CB seen in Chapter 7.

Overall, it was found that graphene oxide was a poor choice for the carbon substrate for a hybrid catalyst support. Despite many suggestions in the literature that graphene oxide may prove to be an excellent catalyst support material because of its high surface area and the high electrical conductivity of graphene materials , it was found that the material is not well suited to the methanol fuel cell ex situ testing environment, and presumably this extends to the in situ fuel cell environment. The graphene sheet structures tended to re-stack, which has a detrimental effect on electrochemical surface area, and would lead to mass transport issues inside a fuel cell environment. In addition, the carbon support has an effect on the growth of the MnO_x and the Pt nanoparticles when they are deposited in a direct growth method.

The use of carbon black as a 3D carbon support, with MnO_x deposited directly on top of the carbon black showed significantly improved durability over the commercial catalysts in ex situ tests, and it was shown that the direct growth mechanism is vital to achieving this exceptional durability.

9.2 Future outlook

While the Pt/MnO_x-GO materials showed good durability, but poor activity, the Pt/MnO_x-CB material showed an improved durability when compared to the commercial standards Johnson Matthey Hispec materials (referred to in this thesis as Pt/C_{com} and PtRu/C_{com}).

The Pt/MnO_x-GO studies suggested that increasing the MnO_x content can improve the durability of the catalyst/support system. Taking these findings into account, further investigations into the effect of increased MnO_x content on the MnO_x-CB support should be undertaken. This may improve the Pt/MnO_x-CB further, or the expected decrease in electrical conductivity may prove to be detrimental to the overall performance.

It would also be interesting to investigate methods by which the particle size of the Pt nanoparticles can be controlled and kept to be a smaller size, as the Pt/MnO_x-GO materials with smaller Pt particle size showed improved durability and performance, so combining the small Pt size with the optimum MnO_x loading should produce a highly durable catalyst/support system with good activity.

In addition, tests with a directly grown PtRu alloy catalyst on the MnO_x-CB support should be undertaken. This would show whether the benefits of the RuPt alloy, which are already employed in commercial catalysts, and the direct contact with the MnO_x-CB support with the catalyst can be combined to further improve the durability of the DMFC anode catalyst.

Further, longer term testing should be undertaken in order to confirm the durability of the MnO_x-CB supported particles. This will show if the MnO_x-CB particles can retain their exceptional durability over the lifetime of a fuel cell, or whether their exceptional durability does not last over the lifetime of the fuel cell.

Finally, the optimum composition of MnO_x-CB supported catalyst from the ex-situ tests should be tested inside a fuel cell environment, and durability studies undertaken to confirm that the ex-situ performance can be transferred into the fuel cell in-situ and improve the durability of the DMFC.

APPENDIX A: RuSePt Nanoparticle Characterisation

The RuSePt nanoparticles which were used in chapter 8 were prepared by James Walker and are discussed in detail in his thesis, titled "Ternary alloy nanoparticles for polymer electrolyte fuel cell electrocatalysis". Briefly, the particles were produced via a solvothermal route, adapted from literature[188] whereby precursors were injected into hot oleylamine at 230°C, the temperature maintained for one hour, and then the particles were washed via centrifugation in ethanol/hexane 50:50 solution. Further details can be found in section 2.3.1.4 of the previously mentioned thesis[183]. The as synthesised particles have a surface capping agent of oleylamine.

The particles were characterised in a range of methods, with more detail to be found in section 2.4.2 of the thesis of James Walker[183]. TEM imaging and subsequent particle sizing showed that the RuSePt particles were spherical in nature, and their size was 3.3 ± 0.4nm.

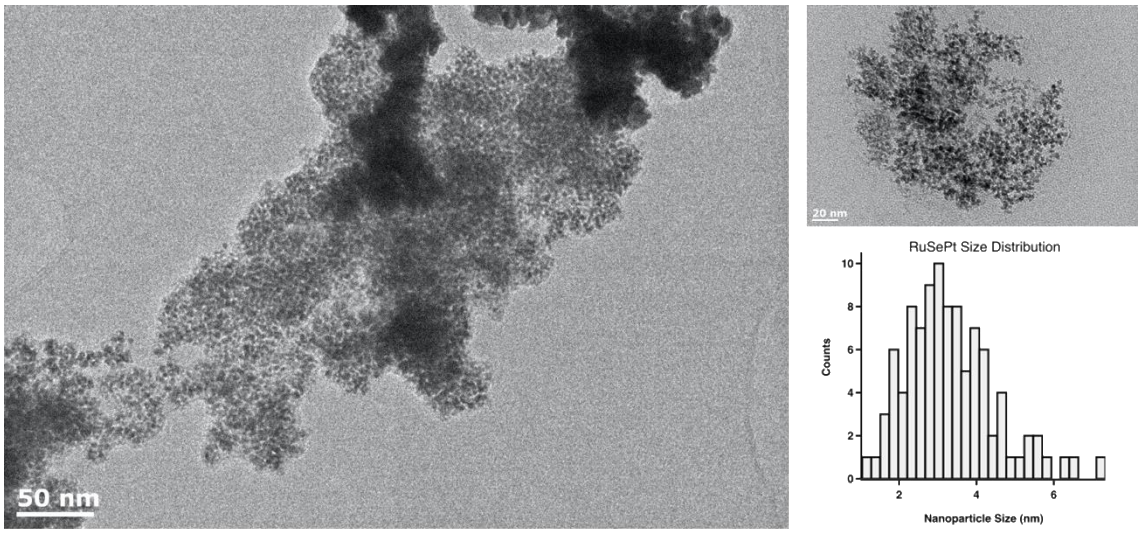

Figure A.1 Particle sizing of the RuSePt particles, used in chapter 8 (picture reproduced with permission from the thesis of James Walker)

The image shown in Figure A.1 confirms the particle sizing (the image is reproduced with permission from James Walker's thesis, section 2.4.2, page 75)

XPS results found that the particles may not have been produced in the 1:1:1 Ru:Se:Pt ratio as was expected. The Ru is believed to be in a much lower ratio because the Ru and its precursor had poor solubility in the oleylamine solvent. However, the composition of the particles is not critical to the results in this thesis, where the focus is on the catalyst-support interaction and its crucial role in the activity and stability of methanol fuel cell anode catalysts.

References

1. United Nations. Paris Agreement. (2015).
2. Department for Business Energy & Industrial Startegy. *UK Energy Statistics , 2018 & Q4 2018*. (2019).
3. Department for Business Energy & Industrial Startegy. *Energy Trends September 2017*. (2017).
4. Møller, K. T., Jensen, T. R. & Akiba, E. Progress in Natural Science : Materials International Hydrogen - A sustainable energy carrier. *Prog. Nat. Sci. Mater. Int.* **27**, 34–40 (2017).
5. Alstom. Coradia iLint - the worlds 1st hydrogen powered train. (2019).
6. Cell, F. & Review, I. The Fuel Cell Industry Review. 1–50 (2018).
7. H2 Aberdeen. H2 Aberdeen. (2019).
8. Transport for London. TfL Bus Fleet Audit 31 March 2018. (2018).
9. Samsung SDI develops military portable DMFC. *Fuel Cells Bulletin* 6–7 doi:10.1016/S1464-2859(09)70182-8
10. Fuel Cell Systems. Fuel Cell Systems - BBC Winterwatch. (2014).
11. Fuel Cell Systems. Arctic expedition uses fuel cell to power research equipment. (2017).
12. The Institution of Engineering and Technology. *Fuel Cells - A Factfile*. (2009).
13. Steele, B. C. H. & Heinzel, A. Materials for fuel-cell technologies. *Nature* **414**, 345–352 (2001).
14. US Department of Energy. Comparison of Fuel Cell Technologies. (2016).
15. Dewar, J. The Boiling Point of Liquid Hydrogen , Determined by Hydrogen and Helium Gas Thermometers. in *The Royal Society of London* **68**, 44–54 (1901).
16. Notardonato, W. U., Swanger, A. M., Jumper, K. M., Maekawa, K. & Takeda, M. Zero boil-off methods for large-scale liquid hydrogen tanks using integrated refrigeration and storage Zero boil-off methods for large-scale liquid hydrogen tanks using integrated refrigeration and storage. in *IOP Conf. Series: Materials Science and Engineering* (2017). doi:10.1088/1757-899X/278/1/012012
17. Air Products. Liquid hydrogen. (2014).
18. Dagdougu, H., Sacile, R., Bersani, C. & Ouammi, A. Hydrogen Storage and Distribution : Implementation Scenarios. in *Hydrogen Infrastructure for Energy Applications. Production, Storage, Distribution and Safety* 37–52 (Academic Press, 2018). doi:10.1016/B978-0-12-812036-1.00004-4

19. Dicks, A. *Fuel Cell Systems Explained*.

20. Law, K., Rosenfeld, J. & Jackson, M. *Methanol as a Renewable Energy Resource*. (2013).

21. Bromberg, L. & Cheng, W. K. *Methanol as an alternative transportation fuel in the US: Options for sustainable and/or energy-secure transportation*. (2010).

22. Wasmus, S. & Kuver, A. Methanol oxidation and direct methanol fuel cells : a selective review. *J. Electroanal. Chem.* **461**, 14–31 (1999).

23. Na, Y., Zenith, F. & Krewer, U. Increasing Fuel Efficiency of Direct Methanol Fuel Cell Systems with Feedforward Control of the Operating Concentration. *Energies* **8**, 10409–10429 (2015).

24. Mehmood, A., Scibioh, M. A., Prabhuram, J., An, M. G. & Ha, H. Y. A review on durability issues and restoration techniques in long-term operations of direct methanol fuel cells. *J. Power Sources* **297**, 224–241 (2015).

25. Arico, A. . *et al.* Selectivity of Direct Methanol Fuel Cell Membranes. *Membranes (Basel).* **5**, 793–809 (2015).

26. Ud Din, M. A., Saleem, F., Ni, B., Yong, Y. & Wang, X. Porous Tetrametallic PtCuBiMn Nanosheets with a High Catalytic Activity and Methanol Tolerance Limit for Oxygen Reduction Reactions. *Adv. Mater.* **29**, 1–8 (2017).

27. Shukla, A. K. & Raman, R. K. Methanol resistant oxygen reduction catalysts for direct methanol fuel cells. *Annu. Rev. Mater. Res.* **33**, 155–168 (2003).

28. Antolini, E., Lopes, T. & Gonzalez, E. R. An overview of platinum-based catalysts as methanol-resistant oxygen reduction materials for direct methanol fuel cells. *J. Alloys Compd.* **461**, 253–262 (2008).

29. Huang, W. *et al.* Highly active and durable methanol oxidation electrocatalyst based on the synergy of platinum-nickel hydroxide-graphene. *Nat. Commun.* 1–8 (2015). doi:10.1038/ncomms10035

30. *Fuel Cell Catalysis A surface Science Approach*. (Wiley, 2009).

31. Korzeniewski, C. & Childers, C. L. Formaldehyde Yields from Methanol Electrochemical Oxidation on Platinum. *J. Phys. Chem. B* **102**, 20–22 (1998).

32. Jusys, Z. & Behm, R. J. Methanol Oxidation on a Carbon-Supported Pt Fuel Cell Catalyst s A Kinetic and Mechanistic Study by Differential Electrochemical Mass Spectrometry. *J. Phys. Chem. B* **105**, 10874–10883 (2001).

33. Wang, H., Wingender, C., Baltruschat, H., Lopez, M. & Reetz, M. T. Methanol oxidation on Pt, PtRu, and colloidal Pt electrocatalysts: a DEMS study of product formation. *J. Electroanal. Chem.* **509**, 163–169 (2001).

34. Wang, H., Wingender, C., Baltruschat, H., Lopez, M. & Reetz, M. T. Methanol oxidation on Pt, PtRu, and colloidal Pt electrocatalysts: A DEMS study of product formation. *J. Electroanal. Chem.* **509**, 163–169 (2001).

35. Housmans, T. H. M., Wonders, A. H. & Koper, M. T. M. Structure Sensitivity of Methanol Electrooxidation Pathways on Platinum : An On-Line Electrochemical Mass Spectrometry Study. 10021–10031 (2006). doi:10.1021/jp055949s

36. Koper, M. T. M. Mechanisms of Carbon Monoxide and Methanol Oxidation at Single-crystal Electrodes. 320–333 (2007). doi:10.1007/s11244-007-9010-y

37. Rizo, R., Lázaro, M. J., Pastor, E. & García, G. Spectroelectrochemical study of carbon monoxide and ethanol oxidation on Pt/C, PtSn(3:1)/C and PtSn(1:1)/C catalysts. *Molecules* **21**, 1–12 (2016).

38. Li, Q., He, R., Gao, J.-A., Jensen, J. O. & Bjerrum, N. J. The CO Poisoning Effect in PEMFCs Operational at Temperatures up to 200°C. *J. Electrochem. Soc.* **150**, A1599 (2003).

39. Cai, J., Huang, Y., Huang, B., Zheng, S. & Guo, Y. Enhanced activity of Pt nanoparticle catalysts supported on manganese oxide-carbon nanotubes for ethanol oxidation. *Int. J. Hydrogen Energy* **39**, 798–807 (2014).

40. Hee, S., Hyun, S. & Soo, Y. Anode Catalysts for Direct Methanol Fuel Cells in Acidic Media : Do We Have Any Alternative for Pt ? *Chem. Rev.* **114**, 12397–12429 (2013).

41. Castanheira, L. *et al.* Carbon corrosion in proton-exchange membrane fuel cells: Effect of the carbon structure, the degradation protocol, and the gas atmosphere. *ACS Catal.* **5**, 2184–2194 (2015).

42. Kocha, S. S. *Electrochemical Degradation: Electrocatalyst and Support Durability*. *Polymer Electrolyte Fuel Cell Degradation* (Elsevier Inc., 2011). doi:10.1016/B978-0-12-386936-4.10003-X

43. Mench, M. M. & Kumbur, E. C. Polymer Electrolyte Fuel Cell Degradation. doi:10.1016/B978-0-12-386936-4.10031-4

44. Trogadas, P. & Fuller, T. F. *Degradation and durability testing of low temperature fuel cell components*. *Polymer Electrolyte Membrane and Direct Methanol Fuel Cell Technology* (Woodhead Publishing Limited, 2012). doi:10.1533/9780857095473.2.194

45. Hansen, H. A., Rossmeis, J. & Nørskov, J. K. Surface Pourbaix diagrams and oxygen reduction activity of Pt, Ag and Ni(111) surfaces studied by DFT. *Phys. Chem. Chem. Phys.* **10**, 3722–3730 (2008).

46. Meier, J. C. *et al.* Degradation Mechanisms of Pt/C Fuel Cell Catalysts under Simulated Start − Stop Conditions. *ACS Catal.* **2**, 832–843 (2012).

47. Meier, J. C. *et al.* Design criteria for stable Pt/C fuel cell catalysts. *Beilstein J. Nanotechnol.* **5**, 44–67 (2014).

48. Singh, R., Awasthi, R. & Sharma, C. Review : An Overview of Recent Development of Platinum- Based Cathode Materials for Direct Methanol Fuel Cells. *Int. J. Electrochem. Sci* **9**, 5607–5639 (2014).

49. Serov, A. & Kwak, C. Review of non-platinum anode catalysts for DMFC and PEMFC application. *Appl. Catal. B Environ.* **90**, 313–320 (2009).

50. El-Shafei, A. A., Hoyer, R., Kibler, L. A. & Kolb, D. M. Methanol Oxidation on Ru-Modified Preferentially Oriented Pt Electrodes in Acidic Medium. *J. Electrochem. Soc.* **151**, F141 (2004).

51. Gasteiger, H. a, Markovic, N., Ross, P. N. & Cairns, E. J. Methanol Electrooxidation on Well-Characterized Pt-Rn Alloys. *J. Phys. Chem.* **97**, 12020–12029 (1993).

52. Kruusenberg, I. *et al.* Highly active nitrogen-doped nanocarbon electrocatalysts for alkaline direct methanol fuel cell. *J. Power Sources* **281**, 94–102 (2015).

53. Qu, L., Liu, Y., Baek, J. B. & Dai, L. Nitrogen-doped graphene as efficient metal-free electrocatalyst for oxygen reduction in fuel cells. *ACS Nano* **4**, 1321–1326 (2010).

54. Wang, C. *et al.* Proton exchange membrane fuel cells with carbon nanotube based electrodes. *Nano Lett.* **4**, 345–348 (2004).

55. Markovic, N. M., Gasteiger, H. A. & Ross, P. N. electrooxidation mechanisms of methanol and formic acid on PtRu alloy surfaces. *Electrochim. Acta* **40**, 91–98 (1995).

56. Choi, J.-H., Park, K.-W., Park, I.-S., Nam, W.-H. & Sung, Y.-E. Methanol electro-oxidation and direct methanol fuel cell using Pt/Rh and Pt/Ru/Rh alloy catalysts. *Electrochim. Acta* **50**, 787–790 (2004).

57. Nonaka, H. & Matsumura, Y. Electrochemical oxidation of carbon monoxide, methanol, formic acid, ethanol, and acetic acid on a platinum electrode under hot aequeous conditions. *J. Electroanal. Chem.* **520**, 101–110 (2002).

58. Antolini, E., Salgado, J. R. C. & Gonzalez, E. R. The methanol oxidation reaction on platinum alloys with the first row transition metals. *Appl. Catal. B Environ.* **63**, 137–149 (2006).

59. Bashyam, R. & Zelenay, P. A class of non-precious metal composite catalysts for fuel cells. *Nature* **443**, 63–66 (2006).

60. Marcu, A., Toth, G., Srivastava, R. & Strasser, P. Preparation , characterization and degradation mechanisms of PtCu alloy nanoparticles for automotive fuel cells. *J. Power Sources* **208**, 288–295 (2012).

61. Holton, O. T. & Stevenson, J. W. The role of platinum in proton exchange membrane fuel cells. *Platin. Met. Rev.* **57**, 259–271 (2013).

62. Mayrhofer, K. J. J., Hartl, K., Juhart, V. & Arenz, M. Degradation of Carbon-Supported Pt Bimetallic Nanoparticles by Surface Segregation. 16348–16349 (2009).

63. Ahn, S. H., Kwon, O. J., Kim, S., Choi, I. & Kim, J. J. Electrochemical preparation of Pt-based ternary alloy catalyst for direct methanol fuel cell anode. *Int. J. Hydrogen Energy* **35**, 13309–13316 (2010).

64. Hartnig, C. *Catalyst and membrane technology for low temperature fuel cells*. *Polymer Electrolyte Membrane and Direct Methanol Fuel Cell Technology* (Woodhead Publishing Limited, 2012). doi:10.1533/9780857095473.1.56

65. Wang, J. G. & Hammer, B. Theoretical study of H2O dissociation and CO oxidation on Pt2Mo(111). *J. Catal.* **243**, 192–198 (2006).

66. Antolini, E. Graphene as a new carbon support for low-temperature fuel cell catalysts. *Appl. Catal. B Environ.* **123–124**, 52–68 (2012).

67. Debe, M. K. Electrocatalyst approaches and challenges for automotive fuel cells. *Nature* **486**, 43–51 (2012).

68. Shao, Y., Liu, J., Wang, Y. & Lin, Y. Novel catalyst support materials for PEM fuel cells: current status and future prospects. *J. Mater. Chem.* **19**, 46 (2009).

69. Liu, H. *et al.* A review of anode catalysis in the direct methanol fuel cell. *Journal of Power Sources* (2006). doi:10.1016/j.jpowsour.2006.01.030

70. Antolini, E. Carbon supports for low-temperature fuel cell catalysts. *Appl. Catal. B Environ. Gen.* **88**, 1–24 (2009).

71. Maass, S., Finsterwalder, F., Frank, G., Hartmann, R. & Merten, C. Carbon support oxidation in PEM fuel cell cathodes. *J. Power Sources* **176**, 444–451 (2008).

72. Wang, J. *et al.* Effect of carbon black support corrosion on the durability of Pt/C catalyst. *J. Power Sources* **171**, 331–339 (2007).

73. Shao, Y., Yin, G. & Gao, Y. Understanding and approaches for the durability issues of Pt-based catalysts for PEM fuel cell. *J. Power Sources* **171**, 558–566 (2007).

74. Shao, Y., Yin, G., Gao, Y. & Shi, P. Durability Study of Pt⁄C and Pt⁄CNTs Catalysts under Simulated PEM Fuel Cell Conditions. *J. Electrochem. Soc.* **153**, A1093 (2006).

75. Sharma, S. & Pollet, B. G. Support materials for PEMFC and DMFC electrocatalysts—A review. *J. Power Sources* **208**, 96–119 (2012).

76. Li, Y. *et al.* Stabilization of high-performance oxygen reduction reaction Pt electrocatalyst supported on reduced graphene oxide/carbon black composite. *J. Am. Chem. Soc.* **134**, 12326–12329 (2012).

77. Zhou, X., Qiao, J., Yang, L. & Zhang, J. A review of graphene-based nanostructural materials for both catalyst supports and metal-free catalysts in PEM fuel cell oxygen reduction reactions. *Adv. Energy Mater.* **4**, (2014).

78. Wu, J., Zhang, D., Wang, Y. & Wan, Y. Manganese oxide–graphene composite as an efficient catalyst for 4-electron reduction of oxygen in alkaline media. *Electrochim. Acta* **75**, 305–310 (2012).

79. Ji, Z., Zhu, G., Shen, X., Zhou, H. & Wang, M. Reduced graphene oxide supported FePt alloy nanoparticles with high electrocatalytic performance for methanol oxidation. 1774–1780 (2012). doi:10.1039/c2nj40133a

80. Han, K. I. *et al.* Studies on the anode catalysts of carbon nanotube for DMFC. *Electrochim. Acta* **50**, 791–794 (2004).

81. Sharma, S. & Pollet, B. G. Support materials for PEMFC and DMFC electrocatalysts—A

review. *J. Power Sources* **208**, 96–119 (2012).

82. Karim, W. *et al.* Catalyst support effects on hydrogen spillover. *Nature* **541**, 68–71 (2017).

83. Huang, T. *et al.* A high-performance catalyst support for methanol oxidation with graphene and vanadium carbonitride. *Nanoscale* **7**, 1301–1307 (2015).

84. Liu, M. Graphene-supported nanoelectrocatalysts for fuel cells: synthesis, properties and applications. *Chem. Rev.* **114**, 5117–5160 (2014).

85. Sharma, S. *et al.* Rapid microwave synthesis of CO tolerant Reduced graphene oxide-supported platinum electrocatalysts for oxidation of methanol. *J. Phys. Chem. C* **114**, 19459–19466 (2010).

86. Geim, A. K. & Novoselov, K. S. The rise of graphene. *Nat. Mater.* **6**, 183–191 (2007).

87. Liu, M., Zhang, R. & Chen, W. Graphene-supported nanoelectrocatalysts for fuel cells: Synthesis, properties, and applications. *Chemical Reviews* (2014). doi:10.1021/cr400523y

88. Brock, S. L. *et al.* A Review of Porous Manganese Oxide Materials. *Chem. Mater.* **10**, 2619–2628 (1998).

89. Li, W. *et al.* Nano-stuctured Pt–Fe/C as cathode catalyst in direct methanol fuel cell. *Electrochim. Acta* **49**, 1045–1055 (2004).

90. Xu, C., Wang, X., Zhu, J., Yang, X. & Lu, L. Deposition of Co3O4 nanoparticles onto exfoliated graphite oxide sheets. *J. Mater. Chem.* **18**, 5625 (2008).

91. Novoselov, K. S. *et al.* Electric Field Effect in Atomically Thin Carbon Films. *Science (80-.).* **306**, 666–669 (2004).

92. Castro Neto, a. H., Guinea, F., Peres, N. M. R., Novoselov, K. S. & Geim, a. K. The electronic properties of graphene. *Rev. Mod. Phys.* **81**, 109–162 (2009).

93. Novoselov, K. S. *et al.* Two-dimensional gas of massless Dirac fermions in graphene. *Nature* **438**, 197–200 (2005).

94. Lee, J.-H., Loya, P. E., Lou, J. & Thomas, E. L. Dynamic mechanical behavior of multilayer graphene via supersonic projectile penetration. **346**, 1092–1096 (2014).

95. Shao, Y. *et al.* Graphene based electrochemical sensors and biosensors: A review. *Electroanalysis* **22**, 1027–1036 (2010).

96. Kumar, R., Sharma, a K., Bhatnagar, M., Mehta, B. R. & Rath, S. Antireflection properties of graphene layers on planar and textured silicon surfaces. *Nanotechnology* **24**, 165402 (2013).

97. Wang, X., Zhi, L. & Müllen, K. Transparent, conductive graphene electrodes for dye-sensitized solar cells. *Nano Lett.* **8**, 323–327 (2008).

98. Eda, G., Fanchini, G. & Chhowalla, M. Large-area ultrathin films of reduced graphene

oxide as a transparent and flexible electronic material. *Nat. Nanotechnol.* **3**, 270–4 (2008).

99. Stoller, M. D., Park, S., Zhu, Y., An, J. & Ruoff, R. S. Graphene-based ultracapacitors. *Nano Lett.* 6–10 (2008). doi:10.1021/nl802558y

100. Huang, Y., Liang, J. & Chen, Y. An overview of the applications of graphene-based materials in supercapacitors. *Small* **8**, 1805–1834 (2012).

101. Yoo, E. J. *et al.* Large reversible Li storage of graphene nanosheet families for use in rechargeable lithium ion batteries. *Nano Lett.* **8**, 2277–2282 (2008).

102. Liang, M. & Zhi, L. Graphene-based electrode materials for rechargeable lithium batteries. *J. Mater. Chem.* **19**, 5871 (2009).

103. Hu, S. *et al.* Proton transport through one-atom-thick crystals. *Nature* (2014). doi:10.1038/nature14015

104. Kauffman, D. R. & Star, A. Graphene versus carbon nanotubes for chemical sensor and fuel cell applications. *Analyst* **135**, 2790–2797 (2010).

105. Hummers, W. S. & Offeman, R. E. Preparation of Graphitic Oxide. *J. Am. Chem. Soc.* **208**, 1339 (1957).

106. Ganguly, A., Sharma, S., Papakonstantinou, P. & Hamilton, J. Probing the Thermal Deoxygenation of Graphene Oxide Using High-Resolution In Situ X-ray-Based Spectroscopies. *J. Phys. Chem. C* **115**, 17009–17019 (2011).

107. Gómez-Navarro, C. *et al.* Electronic transport properties of individual chemically reduced graphene oxide sheets. *Nano Lett.* **7**, 3499–3503 (2007).

108. Krasheninnikov, a. V., Lehtinen, P. O., Foster, a. S., Pyykkö, P. & Nieminen, R. M. Embedding transition-metal atoms in graphene: Structure, bonding, and magnetism. *Phys. Rev. Lett.* **102**, 2–5 (2009).

109. Park, J. *et al.* Ultra-large-scale syntheses of monodisperse nanocrystals. *Nat. Mater.* **3**, 891–895 (2004).

110. Page, T., Johnson, R., Hormes, J., Noding, S. & Rambabu, B. A study of methanol electro-oxidation reactions in carbon membrane electrodes and structural properties of Pt alloy electro-catalysts by EXAFS. *J. Electroanal. Chem.* **485**, 34–41 (2000).

111. Wu, Z.-S. *et al.* Graphene/metal oxide composite electrode materials for energy storage. *Nano Energy* **1**, 107–131 (2012).

112. Liu, M., Zhang, R. & Chen, W. Graphene-Supported Nanoelectrocatalysts for Fuel Cells : Synthesis , Properties , and Applications. *Chem. Rev.* **114**, 5117–5160 (2014).

113. Mirti, P., Davit, P. & Gulmini, M. Colourants and opacifiers in seventh and eighth century glass investigated by spectroscopic techniques. *Anal. Bioanal. Chem.* **372**, 221–9 (2002).

114. Post, J. E. Manganese oxide minerals: Crystal structures and economic and

environmental significance. *Proc. Natl. Acad. Sci.* **96**, 3447–3454 (1999).

115. Liu, X., Chen, C., Zhao, Y. & Jia, B. A Review on the Synthesis of Manganese Oxide Nanomaterials and Their Applications on Lithium-Ion Batteries. *J. Nanomater.* **2013**, 1–7 (2013).

116. Fischer, A. E., Pettigrew, K. A., Rolison, D. R., Stroud, R. M. & Long, J. W. Incorporation of Homogeneous , Nanoscale MnO 2 within Ultraporous Carbon Structures via Self-Limiting Electroless Deposition : Implications for Electrochemical Capacitors. *Nano Lett.* **7**, 281–286 (2007).

117. Yan, J. *et al.* Carbon nanotube/MnO2 composites synthesized by microwave-assisted method for supercapacitors with high power and energy densities. *J. Power Sources* **194**, 1202–1207 (2009).

118. Ko, W.-Y., Chen, L.-J., Chen, Y.-H. & Lin, K.-J. Solvothermal synthesis of shape-controlled manganese oxide materials and their electrochemical capacitive performances. *J. Mater. Res.* **29**, 107–114 (2014).

119. Liu, J. & Pan, Q. MnO/C Nanocomposites as High Capacity Anode Materials for Li-Ion Batteries. *Electrochem. Solid-State Lett.* **13**, A139 (2010).

120. Luo, S. *et al.* Synergistic effect of manganese oxide nanoparticles and graphene nanosheets in composite anodes for lithium ion batteries. *Mater. Res. Express* **2**, 015503 (2015).

121. Ma, T. & Chen, C. Synthesis and electrochemical properties of tube-like nitrogen-doped graphene/manganese oxide composite for supercapacitors. *Micro Nano Lett.* **10**, 282–286 (2015).

122. Xu, H. *et al.* MnOx/graphene for the Catalytic Oxidation and Adsorption of Elemental Mercury. *Environ. Sci. Technol.* 150429105125009 (2015). doi:10.1021/es505978n

123. Park, G. *et al.* One-step sonochemical synthesis of a graphene oxide-manganese oxide nanocomposite for catalytic glycolysis of poly(ethylene terephthalate). *Nanoscale* **4**, 3879–85 (2012).

124. Marquardt, D. *et al.* The use of microwave irradiation for the easy synthesis of graphene-supported transition metal nanoparticles in ionic liquids. *Carbon N. Y.* **49**, 1326–1332 (2011).

125. Zhu, Y. J. & Chen, F. Microwave-assisted preparation of inorganic nanostructures in liquid phase. *Chem. Rev.* **114**, 6462–6555 (2014).

126. Rossi, L. M., Costa, N. J. S., Silva, F. P. & Wojcieszak, R. Magnetic nanomaterials in catalysis: advanced catalysts for magnetic separation and beyond. *Green Chem.* **16**, 2906 (2014).

127. Madler, L., Kammler, H. K., Mueller, R. & Pratsinis, S. E. Controlled synthesis of nanostructured particles by flame spray pyrolysis. *J. Aerosol Sci.* **33**, 369–389 (2002).

128. Mueller, R., Mädler, L. & Pratsinis, S. E. Nanoparticle synthesis at high production rates

by flame spray pyrolysis. *Chem. Eng. Sci.* **58**, 1969–1976 (2003).

129. Wei, W., Cui, X., Chen, W. & Ivey, D. G. Manganese oxide-based materials as electrochemical supercapacitor electrodes. *Chem. Soc. Rev.* **40**, 1697–1721 (2011).

130. Balan, L., Matei Ghimbeu, C., Vidal, L. & Vix-Guterl, C. Photoassisted synthesis of manganese oxide nanostructures using visible light at room temperature. *Green Chem.* **15**, 2191 (2013).

131. Zhao, Y., Li, J., Wu, C. & Guan, L. A general strategy for synthesis of metal oxide nanoparticles attached on carbon nanomaterials. *Nanoscale Res. Lett.* **6**, 71 (2011).

132. Bang, J. H. & Suslick, K. S. Applications of ultrasound to the synthesis of nanostructured materials. *Adv. Mater.* **22**, 1039–1059 (2010).

133. He, Y. *et al.* Freestanding Three-Dimensional Networks As Ultralight and Flexible Supercapacitor Electrodes. 174–182 (2013).

134. Zhang, J., Guo, C., Zhang, L. & Li, C. M. Direct growth of flower-like manganese oxide on reduced graphene oxide towards efficient oxygen reduction reaction. *Chem. Commun. (Camb).* **49**, 6334–6 (2013).

135. Lee, S. W., Kim, J., Chen, S., Hammond, P. T. & Shao-Horn, Y. Carbon nanotube/manganese oxide ultrathin film electrodes for electrochemical capacitors. *ACS Nano* **4**, 3889–96 (2010).

136. Zhao, G. *et al.* Synthesis and lithium-storage properties of MnO/reduced graphene oxide composites derived from graphene oxide plus the transformation of Mn(<scp>vi</scp>) to Mn(<scp>ii</scp>) by the reducing power of graphene oxide. *J. Mater. Chem. A* **3**, 297–303 (2015).

137. Qu, J. *et al.* Highly efficient synthesis of graphene/MnO2hybrids and their application for ultrafast oxidative decomposition of methylene blue. *Carbon N. Y.* **66**, 485–492 (2014).

138. Wang, H., Cui, L., Yang, Y. & Casalongue, H. S. Mn 3 O 4 - Graphene Hybrid as a High-Capacity Anode Material for Lithium Ion. *Am. Chem. Soc.* 13978–13980 (2010).

139. Chen, S., Zhu, J., Wu, X., Han, Q. & Wang, X. Graphene oxide-Mno2 nanocomposites for supercapacitors. *ACS Nano* **4**, 2822–2830 (2010).

140. Hayes, B. *Microwave Synthesis - Chemistry at the Speed of Light*. (CEM publishing, 2002).

141. He, Y. *et al.* Freestanding three-dimensional graphene/Mno2 composite networks as ultralight and flexible supercapacitor electrodes. *ACS Nano* **7**, 174–182 (2013).

142. Deng, J., Wang, X., Duan, X. & Liu, P. Facile Preparation of MnO 2 /Graphene Nanocomposites with Spent Battery Powder for Electrochemical Energy Storage. *ACS Sustain. Chem. Eng.* (2015). doi:10.1021/acssuschemeng.5b00305

143. *Microwaves in Catalysis: Methodology and Applications*. (Wiley, 2015).

144. Adam, D. Out of the kitchen. *Nature* **421**, 571–572 (2003).

145. Peng, Z., Hwang, J. Y. & Andriese, M. Magnetic loss in microwave heating. *Appl. Phys. Express* **5**, 5–8 (2012).

146. Clerk Maxwell, J. A dynamical theory of the electromagnetic field. *Philos. Trans. R. Soc. A Math. Phys. Eng. Sci.* **155**, 459–512 (1864).

147. Bruno, M. M. & Viva, F. A. Carbon Materials for Fuel Cells. in *Direct Alcohol Fuel Cells - Materials, Performance, Durability and Applications* 231–269 (Springer Netherlands, 2014). doi:10.1007/978-94-007-7708-8

148. Morimoto, N., Kubo, T. & Nishina, Y. Tailoring the oxygen content of graphite and reduced graphene oxide for specific applications. *Sci. Rep.* **6**, 4–11 (2016).

149. de Broglie, L.-V. On the Theory of Quanta. *Ann. Phys. (N. Y).* **10**, (1925).

150. Egerton, R. F. *Physical Principles of Electron Microscopy*. (Springer US, 2016). doi:doi.org/10.1007/b136495

151. Einstein, A. On a heuristic point of view concerning the production and transformation of light. *Ann. Phys. (N. Y).* **17**, 132–148 (1905).

152. Moulder, J. F., Stickle, W. F., Sobol, P. E. & Bomben, K. D. *Handbook of X-ray Photoelectron Spectroscopy*. (Perkin-Elmer Corporation, 1992).

153. Morgan, D. J. Cluster cleaned HOPG by XPS. *Surf. Sci. Spectra* **24**, 024003 (2017).

154. Fairley, N. *Introduction to XPS and AES (CasaXPS Manual2.3.15)*. (nexus at nanoLAB, 2009).

155. Walton, J., Wincott, P., Fairley, N. & Carrick, A. *Peak fitting with CasaXPS*. (Arcolyte Science, 2011).

156. Fairley, N. Casa XPS workshop. in (2016).

157. Kittel, C. *Introduction to Solid State Physics*. (Wiley, 2005).

158. Dorofeev, G. A., Streletskii, A. N., Povstugar, I. V., Protasov, A. V. & Elsukov, E. P. Determination of nanoparticle sizes by X-ray diffraction. *Colloid J.* **74**, 675–685 (2012).

159. Monshi, A., Foroughi, M. R. & Monshi, M. R. Modified Scherrer Equation to Estimate More Accurately Nano-Crystallite Size Using XRD. *World J. Nanosci. Eng.* **2**, 154–160 (2012).

160. Sharma, R., Bisen, D. P., Shukla, U. & Sharma, B. G. X-ray diffraction: a powerful method of characterizing nanomaterials. *Recent Res. Sci. Technol.* **4**, 77–79 (2012).

161. PerkinElmer. Thermogravimetric Analysis (TGA): A Beginner's Guide. *PerkinElmer, Inc* 1–19 (2010).

162. PerkinElmer. *Thermogravimetric Analysis (TGA): A Beginner's Guide*. (2015).

163. Singh, A. K. Experimental Methodologies for the Characterization of Nanoparticles. in

Engineered nanoparticles 125–170 (Academic Press, 2016). doi:10.1016/B978-0-12-801406-6.00004-2

164. Inorganic Ventures. ICP Periodic Table Guide. (2014).

165. Wei, R., Fang, M., Dong, G. & Ho, J. C. Is platinum a suitable counter electrode material for electrochemical hydrogen evolution reaction? *Sci. Bull.* **62**, 971–973 (2017).

166. Yin, M., Huang, Y., Liang, L., Liao, J. & Xing, W. ChemComm Inhibiting CO formation by adjusting surface composition in PtAu alloys for methanol electrooxidation w. *Chem. Commun.* **47**, 8172–8174 (2011).

167. Carlos, J., Gómez, C., Moliner, R. & Lázaro, M. J. Palladium-Based Catalysts as Electrodes for Direct Methanol Fuel Cells : A Last Ten Years Review. *Catalysts* **6**, (2016).

168. Ye, R. *et al.* Manganese deception on graphene and implications in catalysis. *Carbon N. Y.* **132**, 623–631 (2018).

169. Groves, M. N., Malardier-Jugroot, C. & Jugroot, M. Improving platinum catalyst durability with a doped graphene support. *J. Phys. Chem. C* **116**, 10548–10556 (2012).

170. Matsui, K. *et al.* X-ray characterisation of polymer intercalated graphite oxide. *Denver X-ray Conf. Appl. X-ray Anal.* **16**, (2009).

171. Spivey, J. J. Complete catalytic oxidation of volatile organics. *Ind. Eng. Chem. Res.* **26**, 2165–2180 (1987).

172. Biesinger, M. C. *et al.* Resolving surface chemical states in XPS analysis of first row transition metals, oxides and hydroxides: Cr, Mn, Fe, Co and Ni. *Appl. Surf. Sci.* **257**, 2717–2730 (2011).

173. Birkner, N. & Navrotsky, A. Thermodynamics of manganese oxides: Sodium, potassium, and calcium birnessite and cryptomelane. *Proc. Natl. Acad. Sci.* **114**, E1046–E1053 (2017).

174. Min, S. *et al.* Hydrothermal growth of MnO_2 /RGO/$Ni(OH)_2$ on nickel foam with superior supercapacitor performance. *RSC Adv.* **5**, 62571–62576 (2015).

175. *Handbook of Graphene Volume 2: Physics, Chemistry and Biology*. (Wiley, 2019).

176. Chung, D. Y., Lee, K. J. & Sung, Y. E. Methanol electro-oxidation on the Pt surface: Revisiting the cyclic voltammetry interpretation. *J. Phys. Chem. C* **120**, 9028–9035 (2016).

177. Augusta M. Hofstead-Duffy, De-Jun Chen, S.-G. S. and Y. J. T. Origin of the current peak of negative scan in the cyclic voltammetry of methanol electro-oxidation on Pt-based electrocatalysts : a revisit to the current ratio criterion †. *J. Mater. Chem.* **22**, 5205–5208 (2012).

178. Zhao, Y., Li, X., Schechter, J. M. & Yang, Y. Revisiting the oxidation peak in the cathodic scan of the cyclic voltammogram of alcohol oxidation on noble metal electrodes. *RSC Adv.* **6**, (2016).

179. Sun, Q., Park, S.-J. & Kim, S. Preparation and electrocatalytic oxidation performance of Pt/MnO2–graphene oxide nanocomposites. *J. Ind. Eng. Chem.* **26**, 265–269 (2015).

180. Fujiwara, M., Matsushita, T. & Ikeda, S. Evaluation of Mn3s X-ray photoelectron spectroscopy for characterization of manganese complexes. *J. Electron Spectros. Relat. Phenomena* **74**, 201–206 (1995).

181. Cho, S. H., Yang, H. N., Lee, D. C., Park, S. H. & Kim, W. J. Electrochemical properties of Pt / graphene intercalated by carbon black and its application in polymer electrolyte membrane fuel cell. *J. Power Sources* **225**, 200–206 (2013).

182. Walerczyk, W., Zawadzki, M. & Okal, J. *Glycothermal synthesis as a method of obtaining high surface area supports for noble metal catalysts*. *Scientific Bases for the Preparation of Heterogeneous Catalysts: Proceedings of the 10th International Symposium, Louvain-la-Neuve, Belgium, July 11-15, 2010* **175**, (Elsevier Masson SAS, 2010).

183. Walker, J. S. Ternary alloy nanoparticles for polymer electrolyte fuel cell electrocatalysis. (University of Birmingham, 2020).

184. Daio, T., Staykov, A., Guo, L., Liu, J. & Tanaka, M. Lattice Strain Mapping of Platinum Nanoparticles on Carbon and SnO 2 Supports. *Sci. Rep.* **5**, 13126 (2015).

185. Wang, M. *et al.* Pt/MnO2 nanosheets: facile synthesis and highly efficient catalyst for ethylene oxidation at low temperature. *RSC Adv.* **7**, 14809–14815 (2017).

186. Ball, D. W. & Key, J. A. Appendix: standard reduction potentials by value. in *Introductory Chemistry - 1st Canadian Edition*

187. Xu, Z., Shen, C., Hou, Y., Gao, H. & Sun, S. Oleylamine as Both Reducing Agent and Stabilizer in a Facile Synthesis of Magnetite Nanoparticles. *Chem. Mater.* 1778–1780 (2009).

188. Niu, Z. *et al.* Anisotropic phase segregation and migration of Pt in nanocrystals en route to nanoframe catalysts. *Nat. Mater.* **15**, 1188–1194 (2016).